POLITECNICO DI TORINO

Master's Degree in Automotive Engineering

Master's Degree Thesis

Evaluation and improvement of Tesla Cybertruck aerodynamic performance

Supervisors

Prof Andrea TONOLI

Prof Farhod ABDULLAYEV

Candidate

Urolbek MUMINOV

October 2023

Abstract

In our fast-changing world with advanced technologies and enough mature attitudes toward the design of vehicles, automotive engineers are still working on how to model the car with parameters that meet the high requirements of the driver while keeping this vehicle within the legislation framework. However, both the requirements of the driver and the restrictions of the legislation framework are increasing significantly year by year. Then it is obvious that the great challenge behind the automotive manufacturers should be overcome.

Following this, the desire to acknowledge how car manufacturers are dealing with this trend, urged us to explore the aerodynamic behavior of recent models on the market and forced us to implement changes to the vehicle. And the present thesis work focuses on the evaluation of the aerodynamic performance of the Tesla Cybertruck and its aerodynamic coefficients reduction in high speeds by installing add-on details.

The first part of the work represents an overview of the fundamentals of aerodynamics, which will be continued with an introduction to aerodynamic vehicle design.

The second part of the work includes the analysis of aerodynamic behavior by executing a CFD Simulation of Cybertruck like in real world conditions using the very powerful numerical software tool STAR CCM+ in order to identify problematic regions in an existing model.

Finally, the installation of additional components was performed on an existing CAD model to further decrease the drag and lift coefficient, followed by a CFD Simulation analysis of an improved geometry.

Table of contents

List of Tables

List of Figures

Acronyms

CFD

Computational Fluid Dynamics

NEDC

New European Drive Cycle

WLTP

Worldwide harmonized Light vehicles Test Procedures

KPH

Kilometers Per Hour

SAE

Society of Automotive Engineers

CP

Center of Pressure

NSP

Neutral Steering Point

ISO

International Organization for Standardization

NASA

National Aeronautics and Space Administration

HVAC

Heating, Ventilation, and Air Conditioning

CAD

Computer-Aided Design

BSS

Basic Suction System

TGS

Turbulence Generation System

WT

Wind Tunnel

GPU

Graphics Processing Unit

CPU

Central Processing Unit

RANS

Reynolds Averaged Navier-Stokes

FCA

Fiat Chrysler Automobiles

Chapter 1

Introduction

“Aerodynamics is for those who cannot manufacture good engines.” the quote which is not too accurate, but which correctly summarize the speaker’s thoughts was made by Enzo Ferrari in 1960 [1]. It was a response to driver Paul Frère who was concerned about the drag caused by the huge front windscreen of his Ferrari 250 Testa Rossa he was going to drive in the high speed 24 Hours of Le Mans. At that instant he was able to defend his statement, becuase his vehicles were on the other level compared to his opponents even with better aerodynamics.

Figure 1.1: Ferrari 250 Testa Rossa at the 24 Hours of Le Mans.

But in our days, where the propulsion systems have reached a high level of maturity and technologies enable us to determine the effect of wind (like CFD tools, wind tunnels, etc.), aerodynamics urges engineers to implement hard work to decrease drag and increase the downforce of their products, which in turn will lead to higher performance and fuel economy.

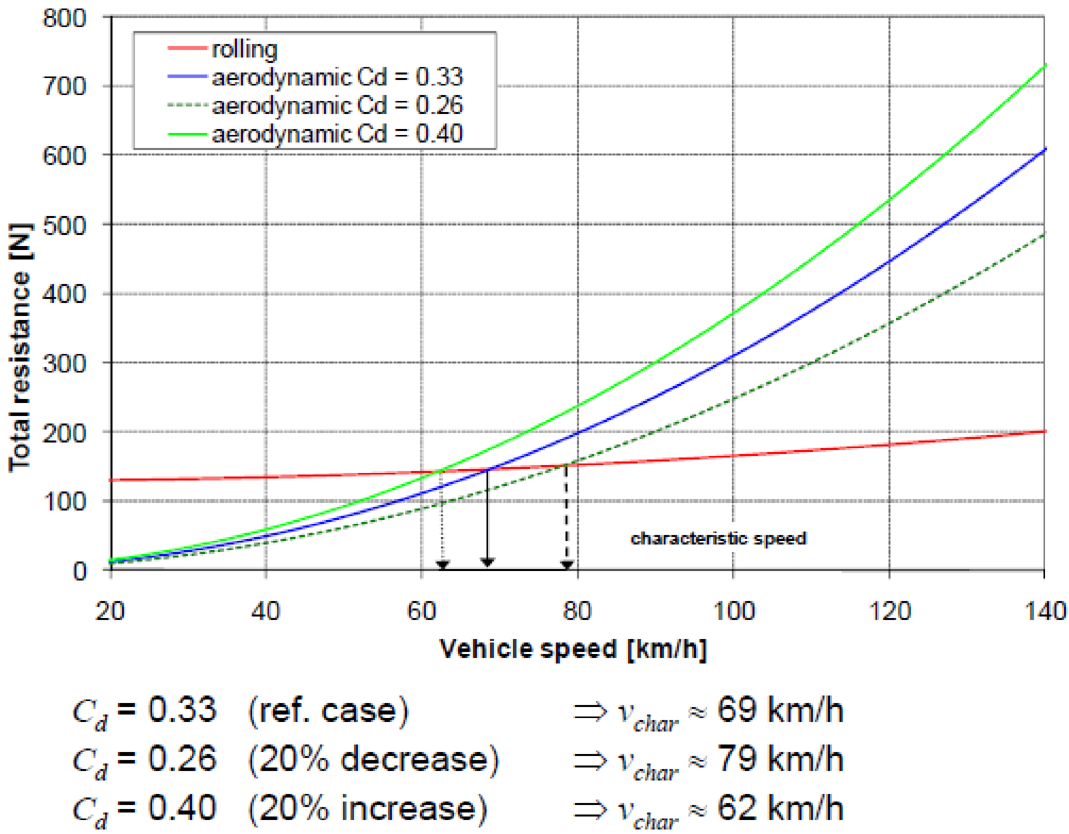

Figure 1.2: Influence of aerodynamic drag on total driving resistance on a level road [2]

At the above picture we can see the effect of drag coefficient on total driving resistance, which can be purely recognized by speed profile differences of the same vehicle with increased and decreased aerodynamic drag. As we can observe, the difference on aerodynamic drag ΔCd = – 0.07, will result in vehicle speed a difference of 10 km/h. But if we consider the case at higher or top speeds, even this small difference in Cd will result in a notable difference in speed.

And what if we increase this variation in drag coefficient for bigger values? Let’s say as in below indicated example.

Figure 1.3: Mercedes-Benz CLA 250 with Cd=0.30

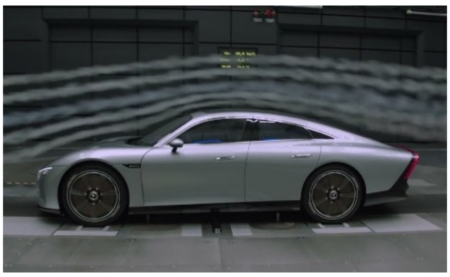

Figure 1.4: Mercedes-Benz Vision EQXX with Cd=0.17

Then, we can estimate how much the vehicle's performance parameters will change and how efficiently the propulsion system will be utilized.

But how is the trend with light-duty trucks? As we all know, their aerodynamic issues due to their large size and mass make them predecessors in this field. Keeping in mind that fuel economy and performance are not less important for them, a great challenge lies ahead of the design engineers that needs to be overcome.
Let’s take as an example the most popular truck in the market:

Figure 1.5: Ford F-150 Lightning Extended Range with Cd=0.56

Ford F-150 Lightning Extended Range is the next generation all electric pick-up truck of the famous F-series trucks of Ford Motor Company with drag coefficient of 0.56 [3].

At that point, Elon Musk had promised that his brand-new, all electric Tesla Cybertruck, which is also a light-duty truck, will have a drag coefficient of 0.3 in a wind tunnel.

Figure 1.6: Tesla Cybertruck

If we look for the shape of this vehicle with a stainless-steel exoskeleton and a bulletproof glass window, the sloping front and back, along with the flat sides, should contribute to reduce air resistance for some amounts [4].

However, this value of drag coefficient is surprisingly low, as this value is accomplished with cars of another type (sedans, hatchbacks and etc.). Also, are there still possibilities to further decrease this amount of drag?

So, the simulation tools we have now let us figure out this issues and see how the air flows around the car, by implementing an aerodynamic analysis of the Tesla Cybertruck existing and modified models on STAR CCM+.

This paper first highlights the fundamentals of aerodynamic phenomena on vehicles, then go on to an introduction to aerodynamic vehicle design. Then, in the second part, there is an evaluation of an existing model aerodynamic performance. Lastly improvement of aerodynamic performance was performed by the installation of add-on details to further decrease a drag and lift coefficients, followed by a CFD simulation analysis of an upgraded geometry.

Chapter 2

Overview of the aerodynamics of vehicles

2.1 Fundamentals of aerodynamics

Aerodynamics describes the movement of objects via air. The forces created by the air flowing over and around the body are determined by how the body reacts to air contact. It is one of the most influential elements on the performance of automobiles and vehicles in total. Driving a vehicle is similar to swimming across an endless sea of floating air particles. Air flow parameters are crucial because they determine the behavior of air around an item. How air flows around an object and how the object interacts with the air is affected by the air's speed, temperature, density, and viscosity. More lift is produced by faster speed, lower temperatures, and lower viscosity, while less lift is produced by higher temperatures, higher viscosity, and lower speeds. In addition, the air's density and viscosity determine an object's drag, with higher densities and viscosities resulting in greater drag.

Isaac Newton developed the first theory of air resistance by investigating the laws of motion. He showed that air resistance is an external force that acts on an object, and that it is proportional to the speed of the object. He also showed that the air resistance force is inversely proportional to the cross-sectional area of an object. He developed a mathematical model to calculate the effects of air resistance on objects, and this was the first accurate model of air resistance, which is still used today. Followed by efforts of Daniel Bernoulli, Bernoulli's Law was developed, and it is a fluid dynamics principle that asserts that the pressure of a liquid or gas is in inverse proportion with respect to its velocity. This principle is used to describe the relationship between pressure, velocity, and the shape of an object in aerodynamic phenomena. Bernoulli's principle is used in aerodynamics to describe the forces and pressures caused by the air flow around an object. For instance, the air pressure around a curved surface is lower than that around a flat surface. In addition, the air pressure surrounding an item increases as air velocity increases.

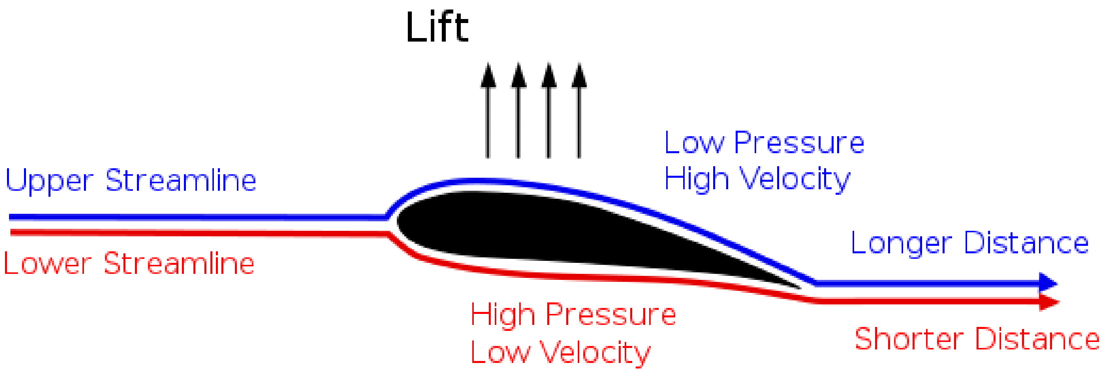

Figure 2.1: Bernoulli's principle

By analyzing the airflow around an object, engineers have determined how the air interacts with the thing and how this interaction impacts the performance of the object.

One of these determinations was the Magnus effect, a phenomenon in which a rotating item in a fluid flow experiences a force perpendicular to the flow's direction. This force, known as the Magnus force, results from the interaction between the rotation of the item and the motion of the fluid, and is responsible for the departure of a spinning ball from its initial path when moving through air. Heinrich Magnus, a German physicist, described the Magnus effect for the first time in 1852.

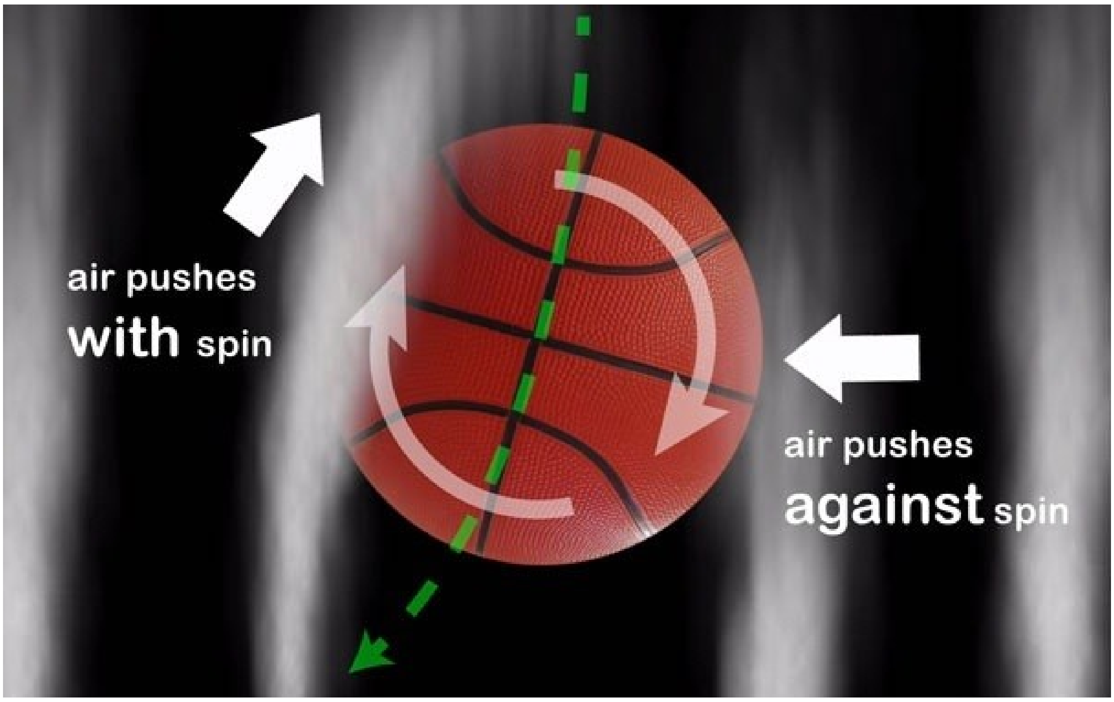

Figure 2.2: Magnus effect

By further investigations in this field, Romanian aerodynamicist Henri Coanda realized Coanda effect in the early 1900s while working on his thesis. The Coanda effect, also known as the wall attachment effect, is a phenomenon in which a fluid jet prefers to adhere to a wall or surface it is directed toward.

Figure 2.3: Coanda effect

The most typical application of the Coanda effect is in aircraft, where the curved curvature of the wings helps to generate lift. It is also utilized in the design of rockets to assist direct the exhaust gases. Certain automotive engines use the Coanda effect to provide a smoother airflow for improved fuel economy.

Following that, in 1904 the German physicist Ludwig Prandtl investigated the boundary layer concept of aerodynamics. Prandtl's work helped explain how the flow of air around an object is affected by the presence of a thin layer of air near the object's surface. This layer has a different velocity profile compared to the bulk flow of the fluid, and it is affected by the viscosity of the fluid.

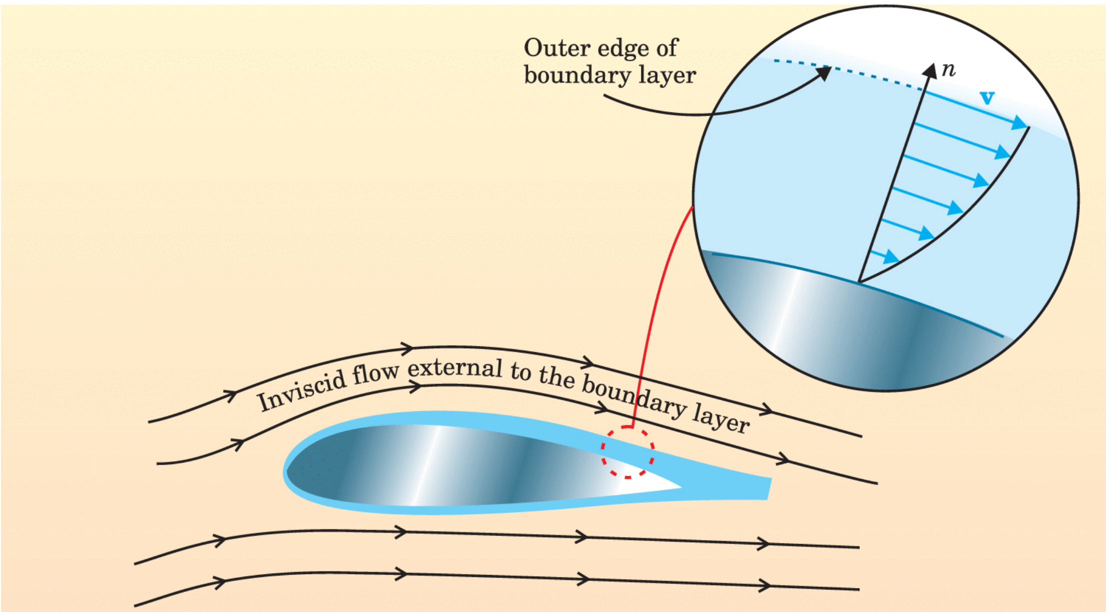

Figure 2.4: Boundary Layer

In real flows, boundary layers can be laminar or turbulent depending on the Reynolds number, quantity expressing the ratio between an inertial forces and a viscous forces. At low Reynolds numbers, the flow in the boundary layer is laminar, meaning that the fluid particles move in smooth, parallel layers. At high Reynolds numbers, the flow becomes turbulent, characterized by chaotic, irregular motion and mixing of fluid particles.

Following this, there are fundamental concepts of aerodynamics involving the study of air flow and the forces that act upon a body moving through the air. Drag, lift, and momentum are three significant phenomena in aerodynamics that influence the motion of objects in fluids such as air.

2.1.1 Drag

Drag is the aerodynamic force that opposes the forward movement of a vehicle through the air [5].

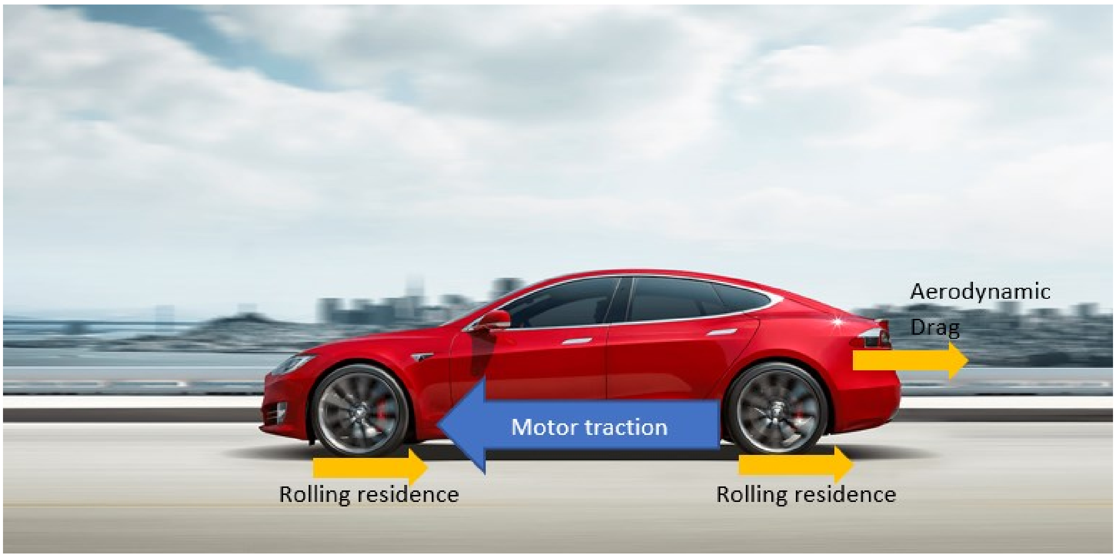

Figure 2.5: Aerodynamic drag on Tesla Model S

Drag is a force that is mechanical in nature. It results from the interaction and contact between a solid and a fluid. It is not generated by a field of a force, as in a gravitational or electromagnetic field, where a single object may affect another with no being in contact. For drag generation, a substantial body must be interacting with the fluid. If no fluid is present, there will be no resistance. Drag is caused by a variance in velocity among a component and a fluid. Motion should exist among the component and the fluid. If there isn't no movement, then drag cannot exist. It makes no difference if the object moves through a fluid at rest or if the fluid goes past a component at rest.

Because drag is a force, it is a vector quantity with both magnitude and direction. Drag operates in the opposite direction of the motion of the vehicle. Drag can be thought of as friction at the air, and skin friction is a cause of drag that exist between particles at an air and the surface of the aircraft. Due to the fact that skin friction represents an interaction among a solid and a gas, both the solid's and the gas's qualities affect how much skin friction there is.

It is dependent on the air's viscosity and the Reynolds number, which reflects the relative size of the forces that are viscous to the flow's motion, for the gas, whereas a smooth, waxed surface produces lower skin friction than a roughed surface for the solid. The boundary layer of minimal energy flow is created across the solid surface, and the boundary layer conditions affect how much skin friction is present.

Let us express drag in relationship with other physical quantities:

$$F_D = 0.5 C_D \rho A v^2 \tag{2.1}$$

The drag force increases with the fluid's density. The greater the density, the greater the mass, the greater the inertia, and the greater the resistance to change direction. Both quantities are proportional to one another:

$$F_D \propto \rho \tag{2.2}$$

With increasing area, drag increases. More surface area means a greater proportion of the object is in contact with the fluid, resulting in greater drag:

$$F_D \propto A \tag{2.3}$$

Drag increases with velocity. Objects that are fixed in relation to the fluid will not experience any drag force. When you begin to move, a resistive force will develop. Accelerate, and certainly the opposing force will increase. The difficult aspect of this relationship is the specific manner in which speed influences drag. Bernoulli's equation suggests that drag should be proportional to the square of speed:

$$F_D \propto v^2 \tag{2.4}$$

Other factors, such as shape, texture, viscosity (which causes viscous drag or skin friction), compressibility, lift (which causes induced drag), boundary layer separation, etc., influence drag. These variables can be combined into a single, massive drag coefficient factor:

$$F_D \propto C_D \tag{2.5}$$

2.1.2 Lift

Lift is an aerodynamic force, which is also mechanical in nature, resulting from the vehicles motion through the air [6]. Since lift is a force, it is a vector quantity with both magnitude and direction. The lift force is exerted at the center of pressure of the object and is oriented perpendicular to the direction of fluid flow. There are numerous variables that influence lift magnitude.

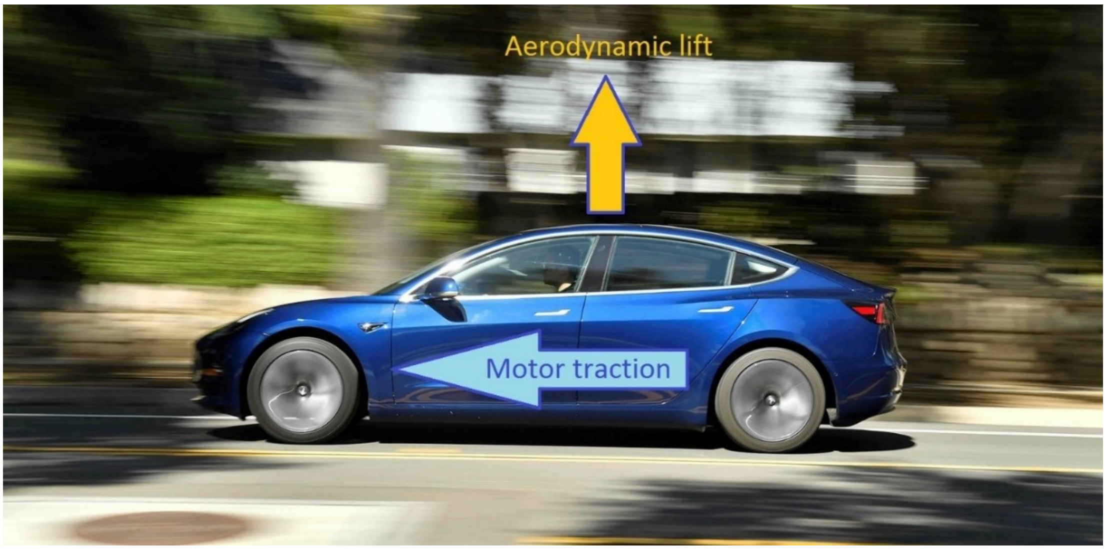

Figure 2.6: Aerodynamic lift on Tesla Model 3

Lift occurs when a large object turns a gas flow in motion. In accordance with Newton's Third Law, the flow is oriented in one direction while lift is generated in the opposite direction. Because air is a gas with freely moving molecules, any solid surface can deflect its flow. Then lift occurs when fluid flows around an object and creates a pressure difference between the upper and bottom surfaces.

When a solid and a fluid (a liquid or a gas) come into touch with each other, lift happens. It isn't formed by a force field in the way that a gravitational field. In this field, one item can affect another without touching it. For lift to happen, the solid body must be in touch with the fluid. Without the fluid, there is no lift. The Space Shuttle does not remain in orbit due to the lift of its wings, but rather due to orbital mechanics associated with its speed. Space almost doesn't have any air. The wings cannot generate lift if there is no air to move.

The variance in velocity between a solid object and a fluid produces lift. Without motion, there is no lift between the object and the fluid. Whether the fluid is moving past a stationary solid or the object is moving through a static fluid, it makes no difference.

As excessive lift can cause the vehicle to lose traction at high velocities and can cause fatal injuries to the driver and other pedestrians as well as damage to public property, lift force is also a major concern for design engineers. Therefore, it is highly preferable that the lift be well within the specified range. Lift can be expressed as:

$$F_L = 0.5C_L\rho Av^2 \tag{2.6}$$

Downforce is a pointing down lift force created by the aerodynamic features of a vehicle. If the vehicle is a car, the goal of downforce is to allow the car to travel faster by increasing the vertical force on the tires, thereby increasing its grip.

Figure 2.7: Niki Lauda's 1976 Ferrari 312 T2 with front and rear wings to produce a downforce

2.1.3 Bluff body aerodynamics

Aerospace engineers are typically involved in the aerodynamics of smooth, slender, streamlined shapes, such as airfoils and wings, that progressively taper to a sharp point at their extending edges. However, non-streamlined shapes with blunt front and rear faces are referred to as bluff bodies (or blunt bodies) are also encountered in a variety of engineering applications [7]. Bluff bodies have a big cross-sectional area relative to their length and are identified by flow separation and extensive wake regions. While both skin friction drag and pressure drag contribute to a body's overall drag, the latter often has a much larger effect on bluff bodies. As depicted in the figure below, this result is due to the effects of the large low-pressure zone generated in the wake behind the body.

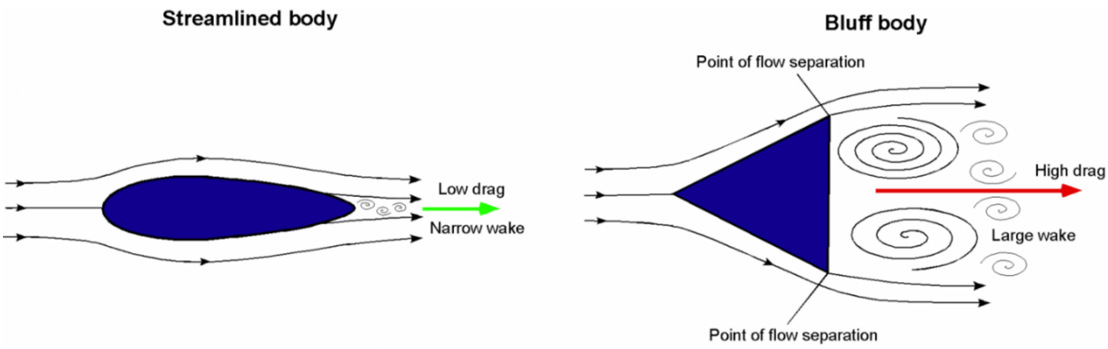

Figure 2.8: Flow and wake regions differences of streamlined and bluff bodies

A body that is aerodynamic has a smooth flow and a compact wake. A bluff body typically generates large-scale flow separation, beginning at the body's extremities or angles, and a broad wake with low pressures, resulting in a high overall drag.

There are an infinite number of bluff body configurations for which the drag (or coefficient of drag) may be required for engineering purposes. In practice, however, far fewer shapes appear, the majority of which have been thoroughly examined, and drag coefficients have been measured in wind tunnels. Multiple publications provide drag coefficients for common two- and three-dimensional bluff body designs that engineers can use in their work. The following table displays the values for cone shape and streamlined bluff body configurations.

Shape	Reference area A	Drag coefficient C_D	Reynolds number $Re = \rho UD/\mu$
Cone (θ, D)	$A = \frac{\pi}{4}D^2$	θ, degrees / C_D: 10 / 0.30; 30 / 0.55; 60 / 0.80; 90 / 1.15	$Re > 10^4$
Streamlined body (D)	$A = \frac{\pi}{4}D^2$	0.04	$Re > 10^5$

Figure 2.9: Drag coefficients for different body configurations

For the majority of aerodynamic objects, the coefficient of drag is nearly constant over a wide range of Reynolds numbers.

For an ordinary sphere, however, the coefficient of drag varies significantly with Reynolds number. Flow past a cylinder and a sphere undergoes a number of velocity transitions as depicted in below figure:

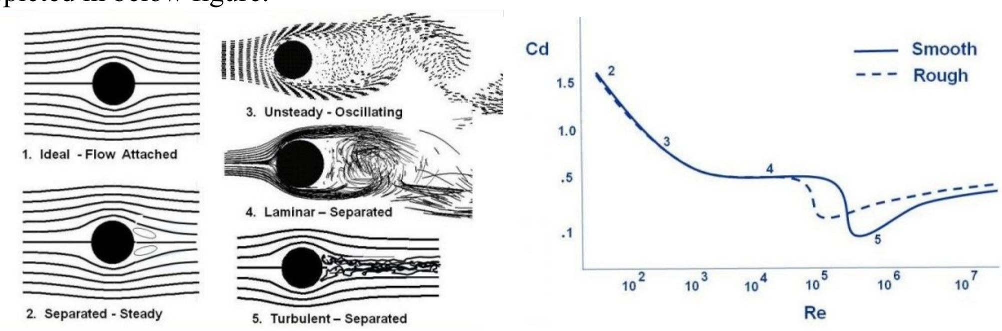

Figure 2.10: Dependence of Cd on Reynolds number for an ordinary sphere [8]

The ball has the same density, viscosity, and diameter in each of the cases depicted in this figure. The flow velocity is increased progressively from the left to raise the Reynolds number.

In first situation, viscosity is wholly neglected due to the extremely slow flow. There is no boundary layer along the surface, the flow is wholly attached (no separation), and there is no viscous wake downstream of the cylinder. Since the flow is symmetric from upstream to downstream, the cylinder experiences no resistance! This unusual result is known as d'Alembert's paradox, after the early mathematician who investigated the issue. The analysis is simplified by ignoring viscosity, but this form of flow does not occur in nature, where every fluid has a small amount of viscosity.

The second situation depicts the actual scenario with low velocity. A pair of stable vortices form on the downstream side of the cylinder. The flow is separated but constant, and the vortices produce quite a big amount of drag on the cylinder or sphere.

The third situation illustrates the flow as the velocity increases. The downstream vortices transform into unstable type, distinct from the main body, and are subsequently shed alternately downstream. The wake is extremely broad and generates a substantial amount of drag. The alternate discharge is referred to as the Karman vortex road. This form of flow is periodic and unsteady, but it repeats at a certain time interval. Variations in pressure caused by changes in velocity generate a sound known as an aeolian tone. This is the sound produced by the wind passing over high-voltage wires or tree branches in the autumn and winter. It is a tone with a low frequency.

The fourth situation illustrates the flow as the velocity is increased further. The periodic flow disintegrates into a disorganized wake. The boundary layer flow on the windward face of the cylinder is laminar and orderly, while the chaotic wake is initiated as the flow turns onto the opposite side of the cylinder. The wake is not quite as wide as in third situation, so there is a slight reduction in drag.

The fifth situation demonstrates an even greater flow velocity. The boundary layer transitions to disordered turbulent flow, with vortices of various dimensions shedding from the body's turbulent wake. The fourth situation describes a situation in which the separating point is originally slightly downstream of the laminar separation point, resulting in a discharge that is originally slightly smaller and a drag that is initially less than the laminar drag. There is a range of Reynolds numbers, during the transition from laminar to turbulent flow, for which turbulent drag is less than laminar drag. As velocity increases, turbulent drag ultimately approaches and exceeds laminar drag value.

All cylinder computations used a smooth surface. Drag depends on boundary layer flow, hence surface roughness will affect it. Experimentally, roughened cylinders and balls transform to turbulent flow at lower Reynolds numbers than smooth ones. The dashed line on the above figure shows drag for a rough surface ball. The effect is intriguing. For the same diameter, velocity, and flow conditions, roughened balls have less drag than smooth balls at a small Reynolds number. This Reynolds number range covers golf ball size and speed. Dimples on a golf ball produce turbulence that would not exist on a smooth ball. Dimpled golf balls fly farther (twice in fact) than smooth balls of the same speed, diameter, and weight due to lower drag:

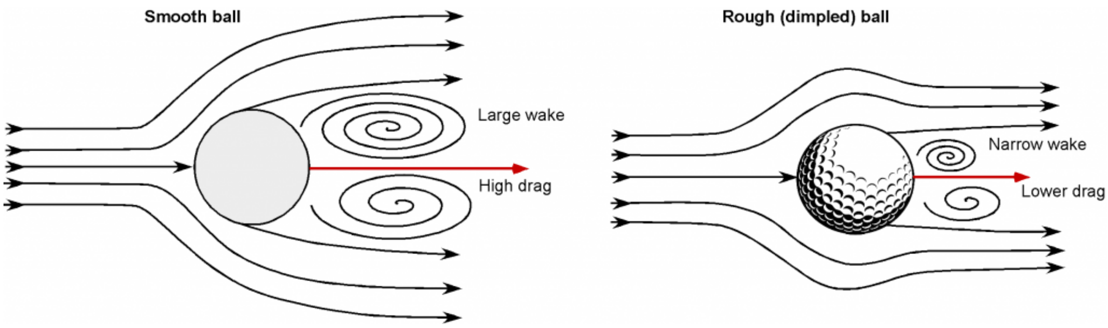

Figure 2.11: Flow sketches about smooth and rough golf balls.

2.1.4 Fundamental equations for compressible flows

In fluid dynamics, the distinction between compressible and incompressible flow is conceptually straightforward: a compressible fluid can undergo a density change during flow, whereas an incompressible fluid does not [9]. According to the principles of material mechanics, the density of an incompressible fluid does not change as a result of shear forces on the fluid caused by viscosity or external body forces. In other words, any density-term derivatives in the Navier-Stokes equations (equations that describe the motion of fluid substances) can be disregarded. This crucial distinction is what makes simple the incompressible fluid dynamics equations relative to the complete Navier-Stokes equations. In both instances, the objective of problems is to calculate the flow velocity field and density in flow problems.

Continuity equation

Lets see a flow field where all properties vary with spatial location and time, for example, $\rho = \rho(x, y, z, t)$. In this flow field, lets consider the fixed finite control volume depicted in Figure 1.18. At a point on the control surface, the flow velocity is **V** and the vector elemental surface area is **dS**. Also dV is an elemental volume inside the control volume.

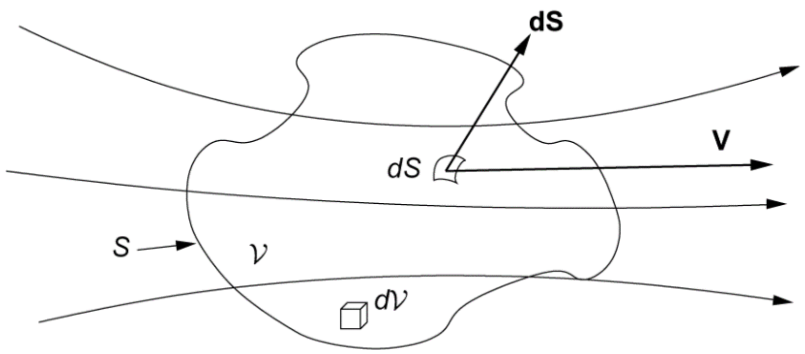

Figure 2.12: Finite control volume fixed in space [10]

Applied to this control volume a physical principle that states mass can be neither created nor destroyed, we can derive that

Net mass flow *out* of control volume through surface *S*	=	time rate of decrease of mass inside control volume *V*

In more simple words, the mass flow that enters the control volume per unit of time exits simultaneously, i.e., no mass accumulates within the control volume.

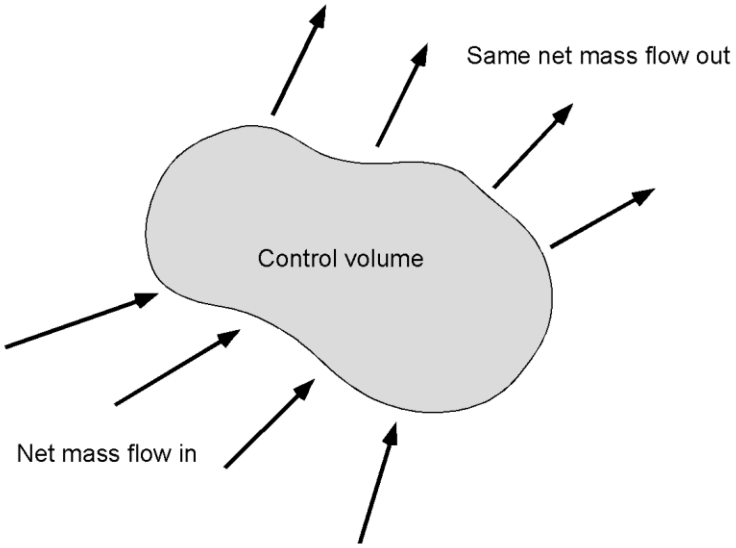

Figure 2.13: In the situation of a steady flow, the mass flow entering the control volume equals the mass flow exiting of the control volume [11].

The continuity equation is the crucial relationship between flow velocity and density.

$$\frac{\partial \rho}{\partial t} + \bar{\nabla} \cdot (\rho \cdot \bar{u}) = 0 \tag{2.7}$$

Here, $\bar{u}$ is the vector of fluid flow, and ρ is the density of the fluid. Usually, the flow rate is written in Cartesian coordinates, but many systems can be made easier by putting the equations of Navier-Stokes into a different coordinate system (such as circular, linear, etc.). This equation effectively conveys the conservation of mass flow rate entering and leaving any system region.

Momentum equation

When forces are involved, the principle of momentum conservation must be applied to a fluid, i.e., Newton's second law of motion must be applied. The conservation of momentum is a fundamental principle applicable to fluid flows, which is mathematically expressed by the momentum equation. The equation accounts for numerous forces acting on a fluid, including body forces, pressure forces, and viscous forces. Depending on the problem at a situation the momentum equation may be simplified by making appropriate assumptions, such as continuous flow or inviscid flow, but only if these assumptions are justified. Using a combination of the momentum and continuity equations, it is possible to solve fluid flow problems involving indeterminate quantities. In situations involving pressure, the principles of the conservation of energy must also be considered.

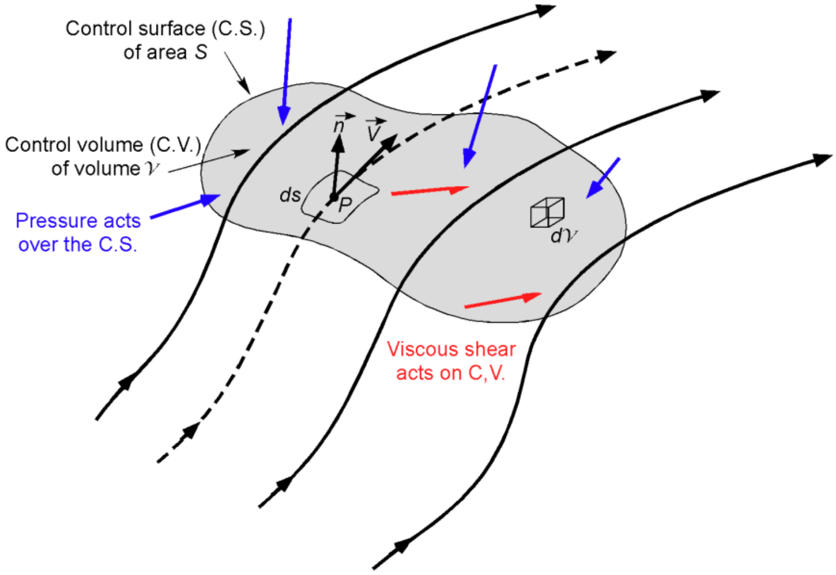

Figure 2.14: A fixed, finite control volume used to establish the most general form of the momentum equation [12].

To be more specific, for compressible flow there is a momentum equation from the Navier-Stokes equation:

$$\rho\left(\frac{\partial\bar{u}}{\partial t}+\bar{u}\cdot\nabla\bar{u}\right)=-\nabla p+\nabla\cdot\left[\mu\left(\nabla\bar{u}+(\nabla\bar{u})^{T}\right)\right]+\nabla\cdot\left[\lambda(\nabla\cdot\bar{u})\bar{I}\right]+\rho\bar{g} \quad (2.8)$$

The conservation of momentum implies that momentum is neither created nor destroyed, as the momentum within a control volume remains constant. It can only alter due to the action of forces in accordance with Newton's laws.

In the above equation (2.8) we can see momentum convection as a sum of mass (body) force, surface (pressure) force and viscous force. Describing further, μ and λ are proportionality constants that determine the viscosity and stress-strain relationship of the fluid, respectively. In general, λ 's value is a function of viscosity. In literature and other sources on fluid mechanics, these quantities are linearly correlated to accommodate situations in which fluids exclusively experience elasticity-related deformation. This is commonly observed in compressible fluids subject to minimal body forces. This phenomenon may not be applicable to gases operating under low-pressure conditions, since they possess a higher susceptibility to compression during the process of flow.

We can instinctively account for viscous or inviscid flows at this point. By setting $\mu = 0$ in the above momentum equation, the viscous components are eliminated, and the resulting system is simplified, thereby defining an inviscid flow. Fluids with adequately low viscosity and very high Reynolds numbers can typically be approximated using the inviscid form of the preceding momentum equation.

Energy equation

When applied to fluid flow, the principle of energy conservation yields a formidable-looking equation, at least in its more general form. The energy equation is based on thermodynamic principles, specifically the first law of thermodynamics, and employs the concepts of heat, work, and power. Internal, potential, and kinetic energy are the forms of energy involved in the majority of fluid problems. The energy equation can be expressed as a power equation, which is derived from its units and represents the rate at which work is performed. The utilization of thermodynamic concepts in issues related to fluid flow requires the incorporation of the equation of condition to facilitate the development of links between identified and unidentified quantities.

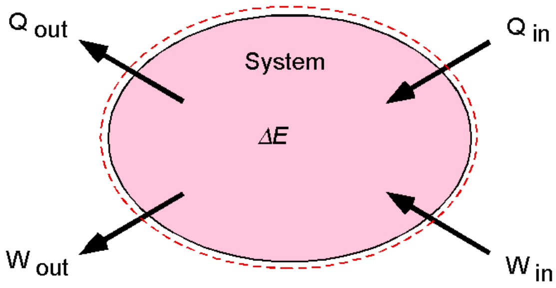

Figure 2.15: According to the first law of thermodynamics, the change in internal energy of a fixed system is equal to the net heat added minus the net work performed on that system [13].

The energy equation is most frequently applied to so-called single-stream systems, in which a certain quantity of fluid energy enters a system where work is added or removed. Then, energy can exit the system in a different form. The Bernoulli equation is derived by simplifying the energy equation for inviscid, incompressible flows without energy addition. This equation is widely applicable in practical scenarios as it establishes a relationship between pressures and flow velocities. The Bernoulli equation can be understood as a manifestation of the principle of energy conservation, whereby a fluid converts its particular kinetic energy into static pressure or potential pressure.

As it is obvious from the first law of thermodynamics about the conservation of energy, the addition of work and heat to a system will result in an increase in the system's total energy. Below we can observe one of the common equations for energy conservation:

$$\rho\left[\frac{\partial h}{\partial t} + \nabla \cdot (hV)\right] = -\frac{\partial p}{\partial t} + \nabla \cdot (k\nabla T) + \phi \tag{2.9}$$

where h stands for enthalpy, k stands for thermal conductivity and ϕ is dissipation rate. This equation equalizes local enthalpy change with time plus convective term to pressure work plus heat flux term plus heat dissipation term.

2.2 Effects of aerodynamics on vehicle performance parameters

2.2.1 Effect on fuel efficiency

In recent years, the need to increase fuel economy has pushed aerodynamics to the forefront of automakers' concerns. Because smoother airflow reduces drag and consequently fuel consumption at a given speed. "Skin friction" is a true phenomenon that occurs when air passes over a surface, and while it may not be as important as other factors such as turbulence and pressure differences, it all adds up.

It is also significantly less expensive for manufacturers to increase efficiency through aerodynamics than through weight reduction or engine technologies. Because it is obvious that weight reduction is done by substituting existing parts with another ones, which are made of much more expensive materials and we all know that engine technologies in our days have reached enough maturity, meaning that further innovations could take longer time.

When we push a car, we soon discover that the friction and rolling resistance of the tires consume an extensive amount of energy. How much energy does it take to propel a vehicle at 30 kilometers per hour if it is difficult to drive it at 3 kilometers per hour? Quite true. At urban speeds, friction and rolling resistance account for the majority of petroleum consumption, while aerodynamic drag is not a significant factor.

However, these forces of friction are linear. Traveling at 60 kilometers per hour requires roughly twice as much energy as traveling at 30 kilometers per hour. In contrast, aerodynamic drag increases in proportion to the square of the velocity [14].

This means that at freeway velocities, aerodynamic drag will account for more than fifty percent of your fuel consumption, if not more. The quicker a vehicle travels, the more fuel is required to propel it through the air.

The power needed to counteract aerodynamic drag has a cubic relationship with velocity, since drag is directly equal to the squared of velocity. This observation suggests a notable association between the velocity of an automobile and the percentage of fuel expended in order to counteract aerodynamic drag.

In the context of passenger cars, it can be determined that aerodynamics plays a significantly larger role in fuel consumption throughout the highway cycle compared to the city cycle, accounting for around 50% and 20% of fuel usage, respectively. This implies that a decrease of 10% in aero drag will lead to an enhancement of 5% in fuel efficiency on highways and a 2% enhancement in fuel efficiency in urban areas.

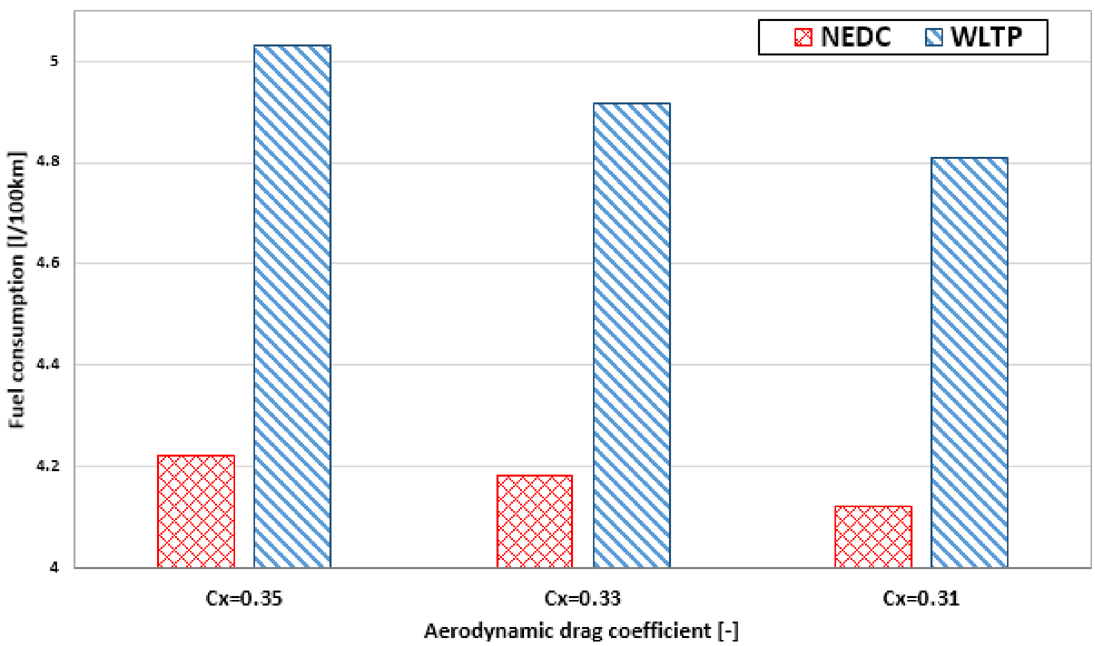

Figure 2.16: Vehicle fuel consumption at different values of aerodynamic drag coefficient while driving on two homologation cycles [15].

There are two occurrences that are increasing the significance of aerodynamics. One observation is that driving cycle speeds are gradually rising to align with the driving patterns of car users. In contrast to the New European Drive Cycle (NEDC), which maintains an average speed of 33.6 kilometers per hour (kph), the recently introduced Worldwide harmonized Light vehicles Test Procedures (WLTP) exhibits a higher speed of 46.5 kph, representing a notable increase of 38%. One additional point to consider is that with the growing prevalence of hybrid vehicles, the utilization of regenerative braking leads to a reduction in the impact of weight, thereby resulting in a higher proportion of overall losses that can be attributed to aerodynamics. The aforementioned enhancement has the potential to reach a maximum of 44% for a high-velocity cycling scenario involving numerous instances of acceleration and deceleration. [16].

Improved aerodynamics won't halve our vehicle's fuel consumption overnight, but a single design change, for instance, could reduce our fuel consumption by 1 km/l, so the savings can add up rapidly [14].

2.2.2 Effect on top speed and acceleration.

For simple explanation how aerodynamics (drag in particular) affects vehicle top speed lets analyze the situation with a parachute jumper with zero initial velocity at the start [17]. The starting velocity is assumed to be zero, the presence of aerodynamic drag is neglected, and the object is considered to be in a state of free fall with a constant acceleration of 9.8 m/s^2.

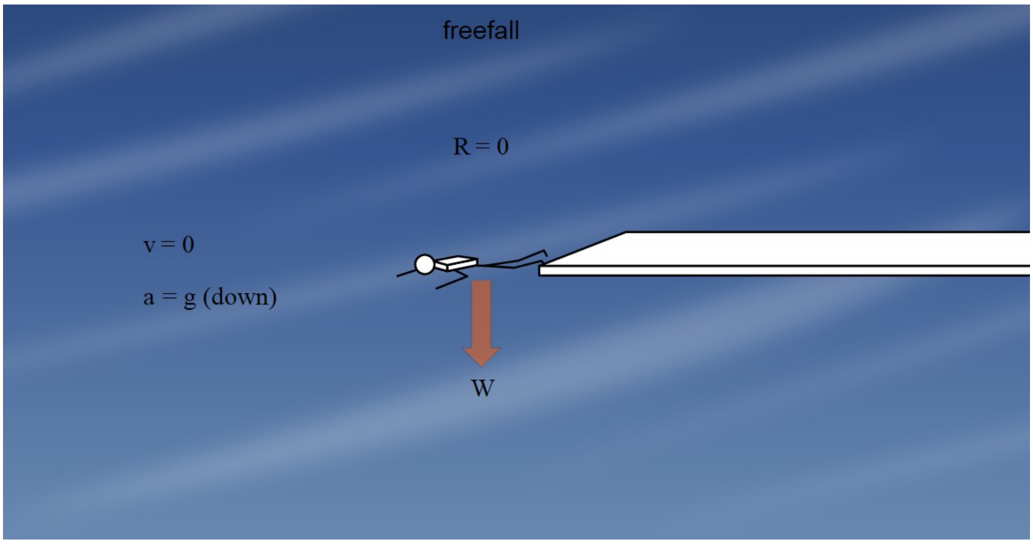

Figure 2.17: Jumper at the beginning with zero initial velocity

The situation becomes quite complicated. The presence of an initial acceleration results in a subsequent amplification of velocity. As the velocity of an object increases, there is a corresponding rise in the magnitude of drag force acting against it, resulting in a reduction in the net force experienced by the object. The reduction in net force leads to a decrease in acceleration. The rate of acceleration is still progressing, although at a slightly reduced pace compared to its original magnitude.

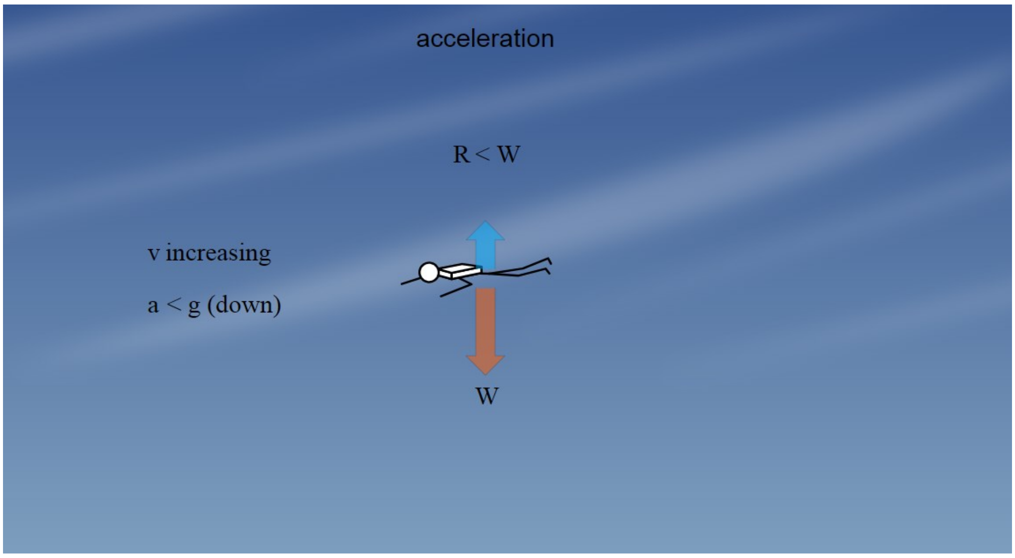

Figure 2.18: Jumper during an increase in velocity

The velocity of a jumper continues to rise, but, the force of drag also experiences a simultaneous increase. As the magnitude of drag force increases, the rate of change of velocity, or acceleration, decreases. One might envision a scenario in which the forces of drag and weight reach a condition of equilibrium. Jumper is in equilibrium. He continues to move, but no longer accelerate. He has achieved his maximum speed.

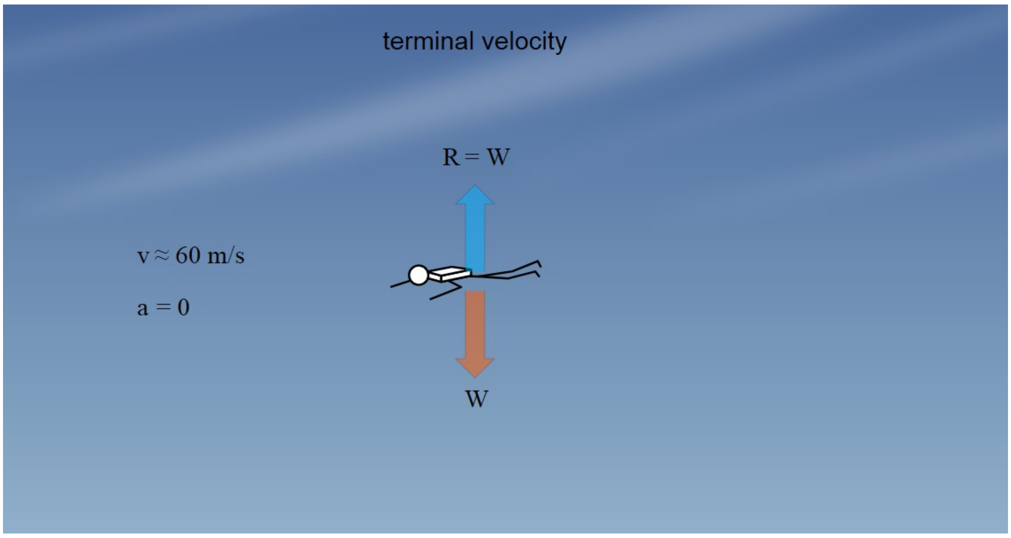

Figure 2.19: Jumper at constant velocity state

As a result of this observation, we can say that, if we maintain a constant position on the accelerator pedal while driving a car, we will eventually attain a terminal velocity. Eventually, the forward propelling force of the tires on the road will equal the backward drag force of the air. This is the case where aerodynamics affects the top speed and acceleration of our vehicles.

And as a result, if we will make a change in vehicle drag coefficient, there will be a change in vehicle top speed:

	V1(Cd=0,35)	**V2(Cd=0,29)**
DETAILS	S=2,1m2;W=1600 kg, PE=150Cv	S=2,1m2;W=1600 kg, PE=150Cv
TOP SPEED [KPH]	207	220

Table 2.1: How is a change in drag coefficient increases top speed [18]

Above indicated table contains experimental results that clearly explains how top speed is dependent on vehicles drag coefficient. And in our example ΔCd of 0.6 results in ΔVmax of 13 kph.

As a direct consequence of above-mentioned explanations and experimental results in this section, we can tell that acceleration has the same effect from the change of drag coefficient, as it is linearly dependent from the velocity of the vehicle. Meaning that it has small impact in low velocity region, compared with its considerable effect in high velocity region of a given vehicle.

2.2.3 Effect on braking distance and time.

To investigate this topic lets continue with a above exploration of parachute jumper case. Now think about the situation in which the parachute opens.

This is the case until the parachute is deployed. The act of deploying the chute results in a substantial increase in the projected area, hence causing a corresponding increase in aerodynamic drag. Currently, the magnitude of the up-drag force surpasses that of the downward gravitational force. The overall force and acceleration have an increasing direction. Once a parachute is initially deployed, the velocity of the falling object is directed downwards, but the acceleration experienced by the object is directed upwards. The deceleration caused by the parachute leads to a reduction in speed, which aligns with the primary objective of utilizing this device.

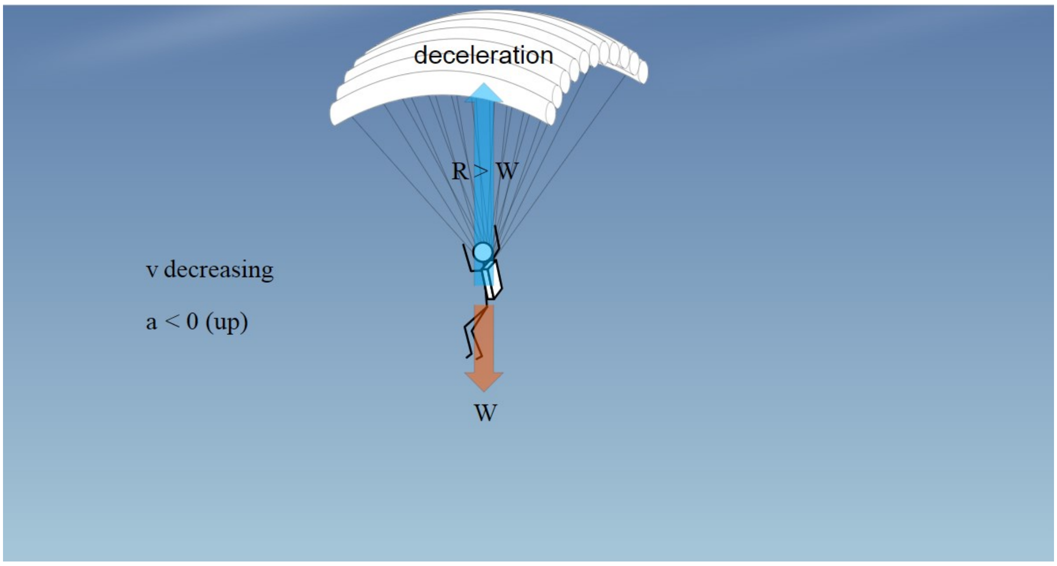

Figure 2.20: Jumper during a decrease in velocity with the parachute open

Speed decreases, so drag reduces. The phenomenon of drag leads to a decrease in net force. Ultimately, the resultant force becomes balanced, leading to the disappearance of acceleration and the obtaining of a modified terminal velocity, characterized by a more favorable landing experience.

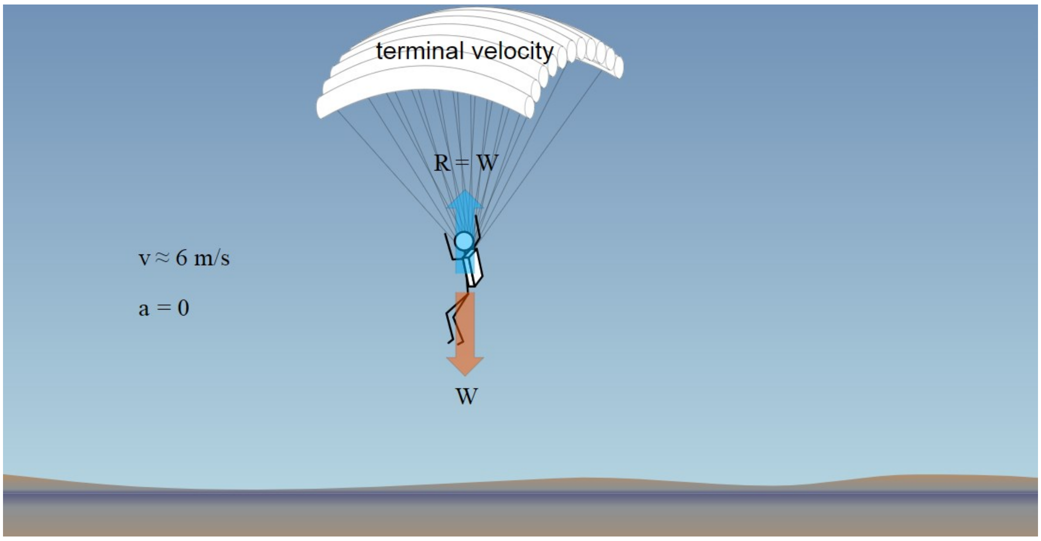

Figure 2.21: Jumper at constant velocity with the parachute open

And if we compare this net force zero condition with braking vehicle case with its terminal velocity equal to zero, we can recognize the impact of drag force and aerodynamics in general to the braking distance and time of the moving vehicle.

Consequently, if we continue our investigation with reference to road vehicles and observe a researches conducted on vehicle longitudinal braking dynamic model, we can observe that during vehicle braking, vehicle deceleration is dependent on the opposing friction force generated between the vehicle wheel and the road, as well as the vehicle's aerodynamic forces. This consists primarily of the wheel rolling resistance force, the vehicle lift and drag forces, and the wheel braking force. Vehicle aerodynamic forces cannot be ignored due to their effect on longitudinal vehicle dynamics, particularly at high speeds. To assure it all, lets review research results below.

In this case, the influence of vehicle aerodynamic forces is studied under various conditions. The first situation occurs when the vehicle is free-rolling from an established initial speed. Figure 2.22 illustrates the difference in braking distance and time when the vehicle is free-rolling at various initial speeds.

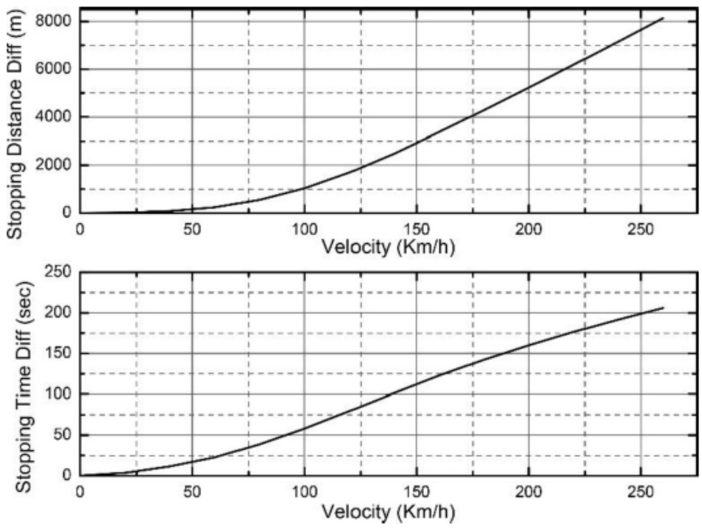

Figure 2.22: Influence of Aerodynamic Forces (Drag and Lift) on the Free Rolling Stopping Time and Distance [19]

The second condition is when the vehicle's braking performance is optimal. Figure 2.23 illustrates the difference in braking distance and time when the vehicle is in a braking condition with different initial speeds.

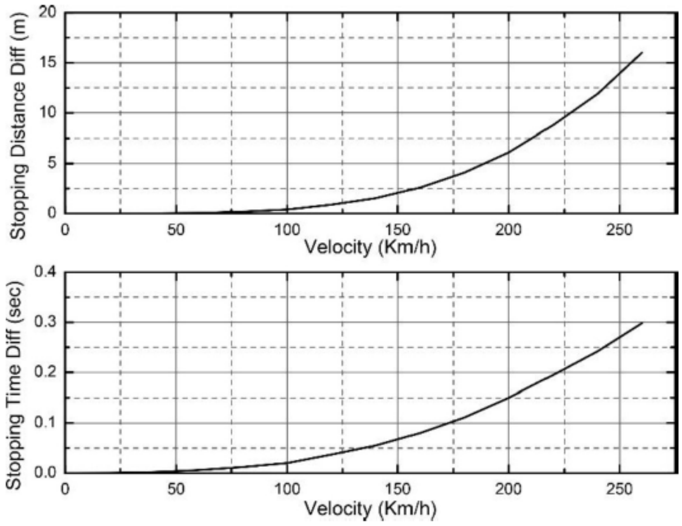

Figure 2.23: Influence of Aerodynamic Forces (Drag and Lift) on Braking Stopping Time and Distance [19]

It is important to note here that the front shape and auxiliary aerodynamic equipment that assist the vehicle's braking will also contribute to the stopping distance.

Figure 2.24: Action of the rear wing of the Bugatti Veyron Grand Sport Vitesse during high-speed braking.

If we consider the case with Bugatti Veyron Grand Sport Vitesse, when braking from velocities greater than 200 kilometers per hour, the rear wing acts as an air brake [20]. It is inclined to a 55-degree angle in less than 0.4 seconds. Created maximum air resistance and rear downforce increase deceleration values from 1.4 G by an additional by 0.6 G while maximizing braking stability.

As illustrated in Figures 2.22, 2.23 and 2.24, the aerodynamic forces of the vehicle cannot be disregarded when calculating braking distance and time, particularly at higher vehicle velocities.

2.2.4 Effect on cornering ability (speed in curve)

Due to its curvilinear motion path, a vehicle's aerodynamic performance can be substantially impacted when it travels around a corner [21]. The flow's yaw angle will vary along its length, and its relative velocity will increase with distance from its central axis of rotation. Particularly in motorsport, aerodynamic analysis of vehicles in the cornering condition is a crucial design parameter. Most racing cars are designed to generate downforce despite the loss of straight-line speed in order to make significant gains in the corners. The recognition of this fundamental truth did not occur until the mid-1960s. However, significant enhancements in cornering, acceleration after cornering, braking (particularly at high speeds), and lateral stability can be achieved by effectively harnessing the capabilities of aero-assisted tire performance. As a result, the utilization of aerodynamic downforce, resulted in a notable improvement in cornering capabilities. This, in turn, led to a substantial rise in cornering velocities from the 1960s to the mid-1990s, as depicted in the figure below. During that time period, the cornering acceleration experienced a significant increase, transitioning from a value lower than the gravitational acceleration (g) to nearly 4g. This change can be attributed to the heightened utilization of aerodynamic downforce.

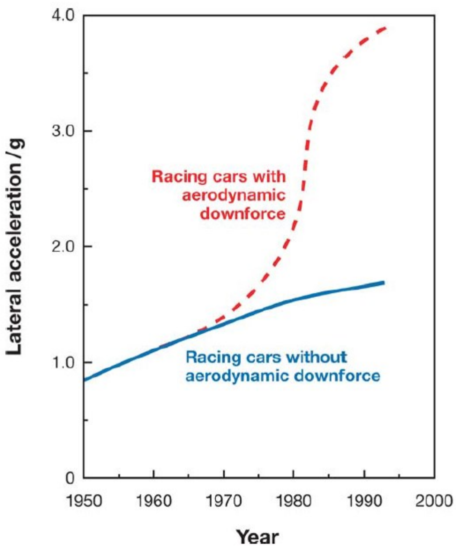

Figure 2.25: Rise in maximum cornering acceleration (1950-2000 years).

The figure provided above illustrates the greatest cornering speeds achieved by race vehicles of significant power during the specified time period, specifically those belonging to categories such as open wheels or prototypes. The graph depicts the overall progression of maximum tire traction, equivalent to the friction coefficient, over time, as seen by the solid line. In contrast, the dashed line illustrates the notable surge that transpired following the implementation of aerodynamic downforce. An intriguing characteristic of that phenomenon is the variation in tire traction, when considering fixed downforce-generating devices, in relation to speed. This implies that during a high-speed braking event, the initial deceleration may reach 4-g, however, it is imperative for the driver to promptly decrease the braking force as the steady reduction in vehicle speed would lead to a decrease in tire adhesion.

Below, we can observe an example of a vehicle with a mass of 600 kg and a frontal area of 1.47 sq. m performing a turning maneuver at a high constant speed.

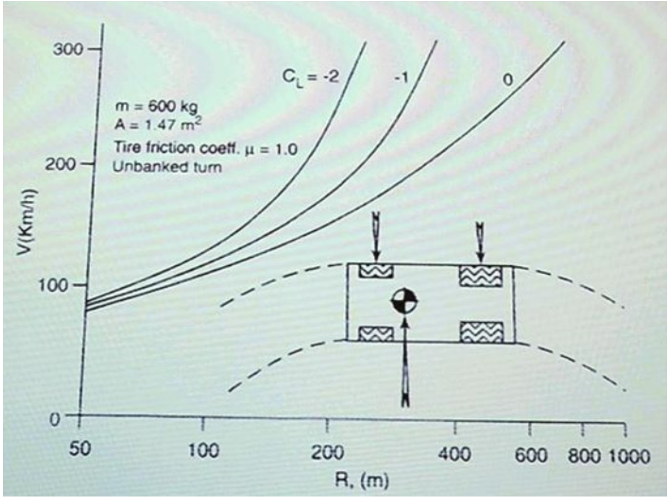

Figure 2.26: Effect of a negative lift (downforce) during cornering at high speeds [22]

From this figure, we can derive that the same vehicle with increased downforce will turn on a radius of 200 m with an increase in speed of 100 kilometers per hour, which is an outstanding result for this vehicle taking into consideration that the mass of the vehicle was left unchanged.

“We spoke to customers and realized they wanted a vehicle that is geared even more towards agility and dynamic cornering. An unadulterated, uncompromising driving machine. Consequently, the vehicle is called Chiron Pur Sport.” - Stephan Winkelmann - Bugatti President. That’s how a vehicle with one of the best performances during cornering is described. In fact, Bugatti Chiron Pur Sport is an outstanding vehicle with its new ESC Sport Plus mode enabling the driver to reach lateral acceleration up to 1,6 g.

Figure 2.27: Design features of Bugatti Chiron Pur Sport

Everything in this aggressive and brave evolution of the Chiron concept has been geared toward agility in every sense, resulting in a confident and muscular appearance. The new front bumper features larger air intakes, a larger lower diffuser, and a wider rendition of the recognizable horseshoe grill. The downforce and aerodynamic performance are improved by reshaped front fenders with integrated air vents. The flat front end and dynamic design highlight the Pur Sport's unique and stunning nature.

The presence of a big diffuser and a stationary rear spoiler (1.9 m. long) contributes to the generation of significant downforce at the rear of the vehicle, simultaneously enhancing maneuverability. Inspired by elements of motorsport and science fiction, the rear wing mounts and bumper diffuser create an X-shaped design that is aggressive and sporty.

2.2.5 Effect on lap time

When increasing the car's aerodynamic downforce coefficient, it is essential to consider the relatively lower increase in drag force or drag coefficient. This drag force, upon reaching a certain value, reduces the speed in a straight line by an amount sufficient to cancel out the effect of increased downforce. Therefore, for extremely high coefficients of downforce, the effect on lap time due to improved cornering is nullified by the decrease in straight-line performance caused by the increase in drag coefficient. The optimum aerodynamic configuration for each vehicle is determined by the critical downforce coefficient, which is the value above which drag cancels out the effect of downforce on the lap time.

In the research conducted on Formula SAE car [23] for determination of critical downforce coefficient the Buddh International Circuit was chosen and inserted into the OptimumLap software. The recorded circuit timing for the FSAE - not aero car, without any additional aerodynamic enhancements, on the Buddh International circuit, is determined to be 139.54 sec. The initial values for the coefficient of drag and the coefficient of downforce are 0.6 and -0.01, respectively. The negative value of C_{DF0} indicates that the vehicle is subject to lift forces. To proceed with the remaining simulations, it is necessary to obtain the drag coefficient corresponding to each assigned downforce coefficient.

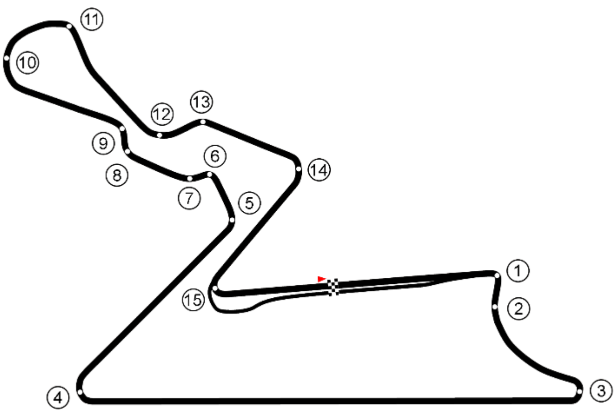

Figure 2.28: Buddh International Circuit

The equation denoted by provides the relationship between the coefficients of lift and drag. As we all know, downforce is the negative value of lift, therefore C_{L0} and C_{L0} are therefore negative in terms of downforce.

$$C_D = k(C_L - C_{L0})^2 + C_{D0} \tag{2.10}$$

where,
C_D - Coefficient of drag (after aerodynamic improvements)
C_L - Coefficient of lift (after aerodynamic improvements)
C_{L0} - Coefficient of lift (before aerodynamic improvements) = 0.01

C_{D0} - Coefficient of drag (before aerodynamic improvements) = 0.6
C_{DF0} - Coefficient of downforce (before aerodynamic improvements) = -C_{L0} = -0.01
C_{DF} - Coefficient of downforce (after aerodynamic improvements) = -C_L
k - Polar coefficient (ranges from 0.03 - 0.04) = 0.04

The equation is solved for increasing values of C_{DF} from 0.1 to 2.5, with C_{DF0} and C_{D0} remaining constant at -0.01 and 0.6 and displayed in the following table.

C_{DF0}	C_{L0}	C_{DF}	C_L	C_{D0}	C_D
-0.01	0.01	0.1	-0.1	0.6	0.600
-0.01	0.01	0.5	-0.5	0.6	0.610
-0.01	0.01	1	-1	0.6	0.632
-0.01	0.01	1.5	-1.5	0.6	0.689
-0.01	0.01	2	-2	0.6	0.758
-0.01	0.01	2.1	-2.1	0.6	0.775
-0.01	0.01	2.2	-2.2	0.6	0.792
-0.01	0.01	2.3	-2.3	0.6	0.810
-0.01	0.01	2.4	-2.4	0.6	0.829
-0.01	0.01	2.5	-2.5	0.6	0.848

Table 2.2: C_{DF} to C_D iteration

Then, for each individual set of C_L and (its corresponding) C_D, the software simulates the lap time and calculates the respective lap time(s). At a certain value of C_L, the lap time curve reverses direction and begins to increase; this is the Critical Lift coefficient. The graph presented beneath depicts the relationship between lap time and downforce coefficient. The initial trend of the relationship has a negative slope, which subsequently transitions to a positive slope subsequent to the achieving the critical downforce coefficient.

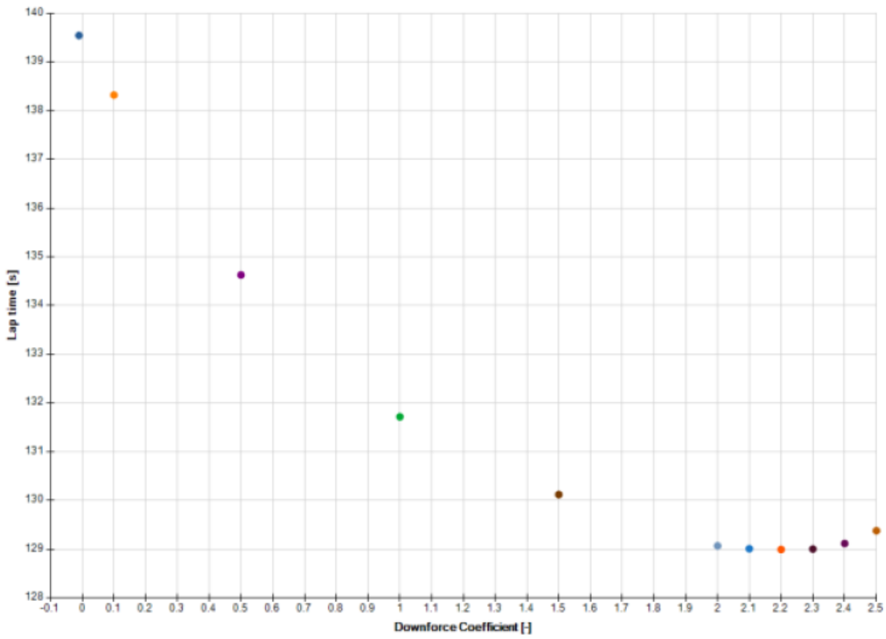

Figure 2.29: Downforce coefficient and lap time correlation

The determined critical C_{DF} for the no aerodynamic car (FSAE) on the Buddh International track is 2.2 based on the above figure, and the corresponding lap time is 128.950 seconds, which is approximately 10 seconds faster than the initial configuration without aerodynamic downforce. The lap duration exhibits an unwanted increase once the C_{DF} is surpassed. Therefore, the aerodynamic improvements should be designed to achieve a coefficient of a downforce of 2.2.

At first glance, it seems that a 10 second difference is not worth efforts made to optimize aerodynamics, but in a race consisting of approximately 370 laps (in 2021, Toyota with Conway, Kamui Kobayshi, and Jose Maria Lopez completed 371 laps in the Le Mans 24 Hours), the difference would become 3700 seconds, which is enormous and a significant advantage over the competition, one that guarantees victory.

2.2.6 Stability to side wind.

The driver's capacity to maintain control over the vehicle while driving on the road might be influenced to some extent by external crosswind disturbances. Crosswind disturbances are inherently present on open highways and their impact on driving stability escalates as vehicle speeds increase.

Typically, a favorable characteristic is the presence of reduced longitudinal and yaw motion reaction to crosswinds, as this will effectively reduce the amount of steering adjustments required by the driver. In the context of a conventional passenger car, it is common for the center of pressure (CP) to be positioned prior to the neutral steering point (NSP), according to depicted in the accompanying image.

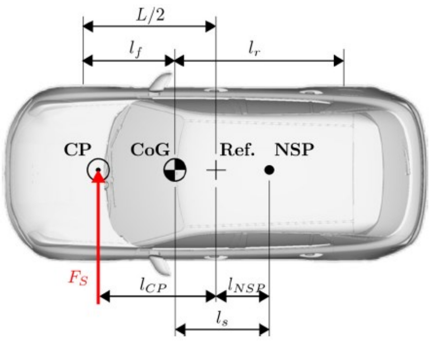

Figure 2.30: The longitudinal positions of the aerodynamic centre of pressure (CP), the centre of gravity (CoG), a geometric reference point midway between the axles (Ref), and the neutral steering point (NSP) depicted from a top view of a vehicle *[24]*.

The NSP, or neutral steering point, establishes the specific location at which a lateral force can be exerted on a vehicle without inducing a yaw rotation. Consequently, in the presence of a crosswind, the vehicle would experience a turning motion away from the direction of the wind, resulting in an aerodynamically unstable condition. The inherent instability shown by passenger vehicles presents a significant obstacle in the development of stable high-speed vehicles, hence posing a formidable challenge for the automotive sector. The heightened emphasis on investigating vehicle handling in conjunction with unstable aerodynamics can be attributed to several factors, including safety concerns, the perceived amount of control, and the anticipated comfort experienced today's automobiles.

Unstable flow conditions on roadways arise from the presence of turbulence in the ambient wind, flow disruptions induced by other cars, and barriers located alongside the route. Experimentation has demonstrated that on-road turbulence has a significant impact on the aerodynamics of vehicles and that freeway traffic experiences turbulence intensities of up to 15%.

The ISO 12021:2010 guidelines include a methodology in which a vehicle is driven at 100 km/h into a zone with a crosswind of 20 m/s, this leads to a relative flow angle of ψ = 35.8 (the figure below illustrates how the vehicle velocity, v_x, and horizontal wind components, w_x and w_y, influence the relative flow magnitude, V_{mag}, and angle ψ).

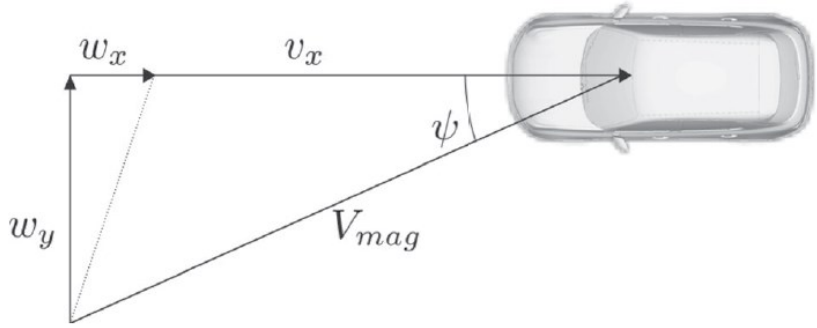

Figure 2.31: Relationship between flow angle, and flow velocity, Vmag, and vehicle velocity, vx, and horizontal wind components, wx and wy.

The high velocity winds of 20 m/s generate significant aerodynamic forces and induce a noticeable motion response in the vehicle, which becomes valuable in quantifying inequalities among various vehicles and configurations.

During a research study of sidewind sensitivity, simulation software was used to examine the effects of a sudden sidewind [24]. By analyzing steering wheel angle torque, roll angle, etc., the impact on the vehicle's stability and safety can be observed with clarity. In the figures below, the steering wheel angle and steering torque deviation of a vehicle traveling at a constant speed of 80 km/h on a straight flat road with μ=0.85 and a crosswind velocity of 100 km/h originating from both the left and right fans (acting in a periodically alternating sequence) are depicted.

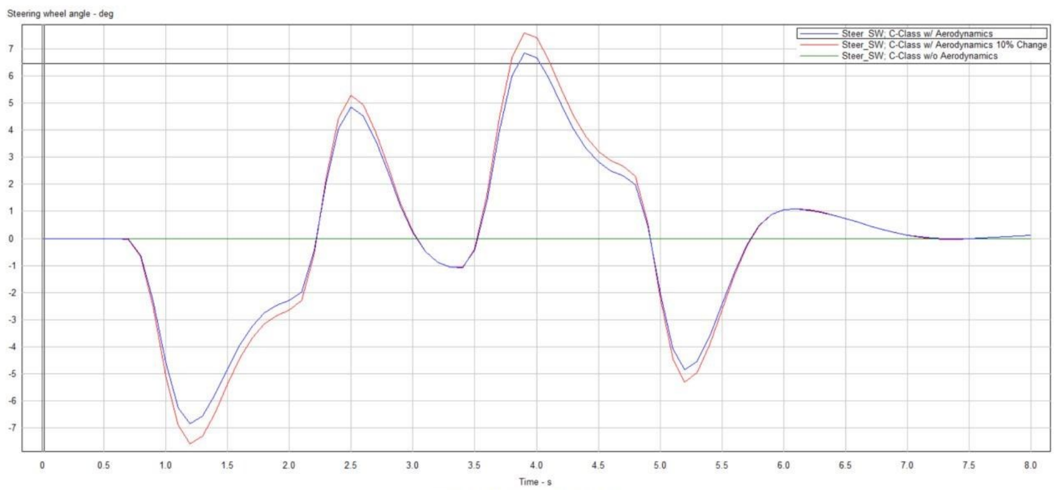

Figure 2.32: Deviation in steering wheel angle caused by crosswinds

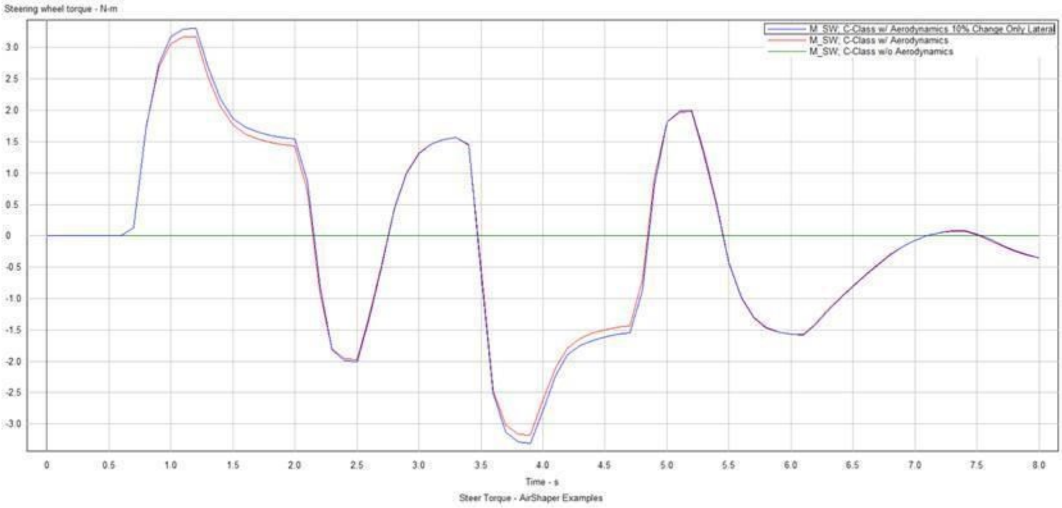

Figure 2.33: Crosswind comparison of time versus steering torque

Nevertheless, more exact results are obtained in wind tunnel analysis using its turntable option. One of these wind tunnels is present in Volvo with its 6.6-meter-diameter turntable and test yaw angle of +/- 30 degrees. Wind speed can reach 250 km/h, and moving ground can reach 260 km/h. More brief information about wind tunnels is given in the next section.

Figure 2.34: The Volvo Cars Wind Tunnel, Volvo C30 testing

Knowing the influence of a side wind force is of greatest significance in the development of cars that prioritize safety, as well as in the formulation of an effective control strategy for autonomous vehicles. The parametric sensitivity analysis revealed that the longitudinal placement of the center of gravity has the greatest effect on crosswind sensitivity, followed by the aerodynamic coefficient of yaw moment gradient. Other crucial vehicle dynamic characteristics included vehicle mass, yaw mass moment of inertia, and tire base. Increasing these parameters improved the stability of the crosswind. Both tire and suspension parameters offer practical approaches to enhancing crosswind stability performance. It was determined that increasing the lateral tire cornering stiffness was advantageous, and that the side force steer gradients at both the front axle and particularly the rear axle were significant. Both the front axle side force steer and the rear axle side force steer exhibited a robust non-linear interaction with the roll steer. Therefore, the conclusion is that the suspension setting can be modified significantly to enhance crosswind stability.

2.3 Wind tunnels overview

2.3.1 Definition of aerodynamic wind tunnels

The utilization of wind-tunnel testing for full-scale or model-scale components is a commonly used methodology that informs intricate design choices in thermal-fluid systems and facilitates fundamental exploration of fluid phenomena. There are numerous occurrences in which theoretical and/or computational methods prove insufficient, either due to the intricate nature of the problem or the absence of appropriate computational resources. Wind-tunnel testing is frequently employed as a cost-effective methodology due to several factors, including the financial implications associated with various types of full-scale testing. These charges can be linked to wind-tunnel tests by appropriately aligning the parameters.

Wind tunnels are commonly utilized in various research institutes, universities, industrial settings, and governmental bodies for a diverse range of purposes. These wind tunnels can be categorized in numerous manners.

Figure 2.35: Pininfarina Wind Tunnel

Wind tunnels can also be categorized according to their operation flow regime and the accompanying relevant dimensionless characteristics. The characterization of an incompressible fluid flow, such as air, is commonly done primarily through the utilization of its Reynolds number. The primary characteristics of compressible gaseous flow are defined by the values of its Mach and Reynolds numbers, respectively. The primary characteristics that define the flow of liquids are the Reynolds and Froude numbers. The significance of these characteristics cannot be overstated, as achieving dynamic similarity is a fundamental objective of wind-tunnel testing. Dynamic similarity refers to the condition when all pertinent dimensionless parameters align between the model being tested and the full-scale system. However, it is important to acknowledge that attaining dynamic similarity is often challenging in practice.

Wind tunnels are frequently categorized based on their size from a practical perspective. For instance, wind tunnels with low speeds (Mach number less than 0.3) exhibit a range of sizes, ranging from compact tunnels with test sections less than approximately 1 m × 1 m, to expansive tunnels that can accommodate full-scale autos, trucks, and massive models of aircraft components. High-speed transonic and supersonic wind tunnels are frequently utilized, despite their dimensions are generally less than those of low-speed wind tunnels because to the higher power demands associated with their operation. Wind tunnels can be categorized based on their specific applications.

Wind tunnels can be categorized based on their intended use. Several examples of specialized tunnels used for various research purposes include: tunnels equipped with moving ground planes to conduct automobiles testing, icing tunnels designed to study the impact of ice formation on airplanes wings, climate tunnels used to simulate different kinds of environments, smoke tunnels employed for flow representation, propulsion tunnels utilized for evaluating engines for airplanes, spin tunnels dedicated to studying the spin recovery of airplanes, and stability tunnels employed to investigate flight dynamics.

2.3.2 Wind tunnel characteristics

Drive system

The tunnel drive system, which states how the working fluid is transported through the test section, is a defining characteristic [25]. The selection of the optimal operational mode for various drive systems is based on the medium and operational regime.

In the context of an air tunnel, the two main propulsion mechanisms employed are a compressor and a fan. In the initial scenario, compressed air is sourced from a compressor, typically stored in tanks, and directed to the tunnel via a regulated valve or regulator. In the latter scenario, the axial or centrifugal fans / blowers are utilized to either exert a pushing or pulling force on the air within the test section. Fans and blowers can be categorized into two types of drives: shaft-driven or belt-driven. The choice between these drive systems is determined by factors such as cost considerations and the required performance characteristics.

Compressor-driven facilities are a cost-effective solution that can achieve significant pressure ratios, making them a favoured choice for high-speed facilities with demanding stagnation pressure requirements. The trade-off refers to the finite quantity of air that is allocated for a given test. Due to the inability of conventional compressors to sustain the required continuous mass flow, the duration of experiments conducted in these tunnels is sometimes restricted to just minutes or less. This limitation is dependent upon factors such as the beginning pressure, volume of the storage tank, and the rate of mass flow. Fan-based systems have the capability to function in a continuous manner; nevertheless, it is important to note that the associated costs exhibit a significant increase in proportion to the volume rate of flow and power requirements.

Fans usually show optimal performance when operating in conjunction with lower-speed systems. One instance of a compressor-driven facility is the 20-inch Supersonic Wind Tunnel at NASA Langley Research Center. The 14’ × 22’ Subsonic Tunnel at NASA Langley is a fan-driven facility of considerable size.

Figure 2.36: The 14’x22’ Subsonic Tunnel at NASA Langley

Operating fluid

When achieving dynamic similitude is hard several options are available. Initially, it is possible to modify the working fluid utilized in the tunnel, deviating from the one employed in the full-scale application. However, in cases where the working fluid differs from the ambient fluid or is not suited to ambient circumstances, such as pressured air or water, it becomes necessary to utilize a closed-circuit facility that is appropriately sealed to prevent any leakage.

An alternative approach involves employing a compressed gas as an operating fluid. The observed consequence of a certain temperature is an increase in density, which in turn aids in achieving a matching Reynolds number. Considerations should be taken into account for the amplified dynamic loading, which is directly proportional to the dynamic pressure.

Alternately, the flow characteristics can be modified by cooling the gas medium. This can be accomplished through the use of a cryogenic system to increase fluid density and decrease viscosity. Such facilities need substantial thermal insulation and extensive refrigeration systems.

Duct circuit

Wind tunnels can be constructed with either open or closed duct circuits. At one end of the tunnel circuit, an open-circuit facility draws air from ambient, passes it through the tunnel, and then exhausts to ambient. Closed circuit tunnels retain a constant mass of air, without accounting for leakage, and circulate flow through the various wind tunnel components in a closed loop.

Open-circuit tunnels usually show reduced fabrication costs and require less physical space. The process of visualizing flow in the test area is made simple due to the continuous circulation of new fluid and the ease of implementing targeted seeding. A disadvantage of open-circuit tunnels is that, for a given speed, they typically require more energy to operate. Additionally, considerably more flow conditioning may be necessary to achieve flow quality comparable to that of an equivalent closed-circuit tunnel. The tunnel's entrance and exit must be clear of obstructions. Additional seeding material is necessary for the purpose of flow visualization due to the absence of a straightforward mechanism for recycling the seeding particles. The operational aspects of tunnels are contingent upon their design and location, with the influence of local weather conditions playing a significant role. One possible approach to regulate the flow conditions, specifically the temperature and relative humidity, involves situating the wind tunnel within a spacious enclosed chamber equipped with a heating, ventilation, and air conditioning (HVAC) system that surpasses the demands imposed by the wind tunnel.

Closed-circuit facilities, despite spending extra construction expenses, exhibit lower running costs compared to open-circuit facilities when operating circumstances are similar. Although the process of purging seed material demands additional effort, it results in a reduced quantity of material needed for a specific experiment. However, the seed rapidly generates a homogeneous "fog" within the tunnel, facilitating uniform but global (rather than localized) seeding. In the majority of instances, the operation of the tunnel is not significantly affected by local weather conditions. Additionally, the process of flow conditioning is less complex due to the greater regulation of input flow conditions. Nevertheless, the alteration of thermodynamic properties may occur when air is heated as a result of the recycling air that passes by the drive system as well, which is often positioned in line with the flow channel to facilitate cooling. To prevent this issue, it is necessary to implement a flow cooling control system.

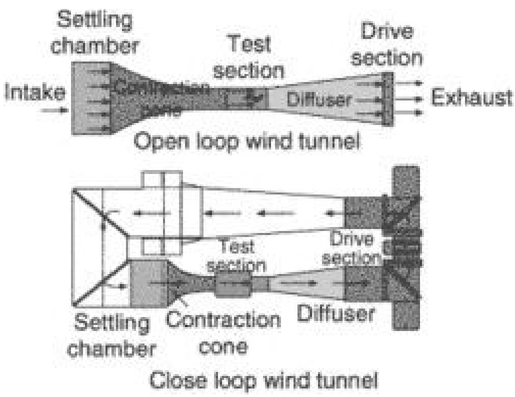

Figure 2.37: Open and closed-circuit wind tunnels.

After all, an effective wind tunnel should provide the acquisition of precise and reliable measurements of either steady or unstable data, based upon the specific application requirements. It is imperative that the turbulence strength within the test section be sufficiently reduced in order to enable the comprehensive examination of the desired physical phenomena. An instance that illustrates the necessity of exceptionally low levels of turbulence in boundary-layer transition studies. The test portion should exhibit a consistent and stable flow pattern, without any unwanted fluctuations. Additionally, efforts should be made to reduce the impact of secondary flow effects within the contraction. In order to reduce flow unsteadiness, noise, and decrease losses, it is essential to prevent flow separation inside the tunnel circuit. In order to accurately replicate freestream circumstances, it is essential that the test's section model and its matching streamline curvature do not significantly impact the flow by causing blockage effects. The vibrations produced by the drive system should be dampened to reduce their impact on the experiment.

Chapter 3

Introduction to aerodynamic vehicle design

3.1 Body shape effect in vehicle aerodynamics

If we start investigating a body shape evolution of vehicles, it is necessary to say that within twenty-five years of its invention, the automobile evolved from essentially an open "horseless" carriage to a fully enclosed vehicle with a clearly defined design language. This early design evolution was heavily influenced by aerodynamics, but with these enclosed structures, the emphasis shifted to shape and form. Despite the fact that some streamlined vehicle designs of the 1930s were undoubtedly "fashion followers," the original leading developments, particularly by Jaray [26], were the result of the same scientific approach to research and development that was evolving in the aircraft and airship industries.

In 1922, Jaray and his colleague Klemperer conducted experiments to determine how the proximity of simple body shapes to the ground affected their aerodynamic performance. Their discovery of a "half-body" teardrop shape with wheels yielding a drag coefficient (C_D) of just 0.15 was less than 20% of typical automobiles of the time and remains a distant goal for modern aerodynamicists. Below figures depict the ideal streamlines discovered by Klemperer and Jaray during 1922 wind tunnel experiments.

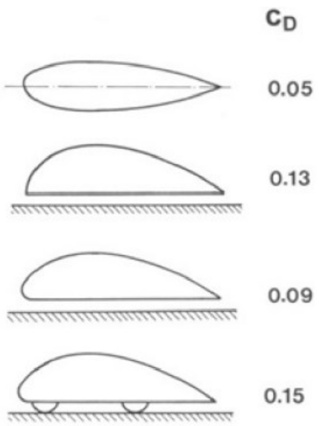

Figure 3.1: Klemperer and Jaray Test Results

Although Jaray's work was not the first one that tried to reduce the aerodynamic resistance of road vehicles, it appears to have had the greatest impact. The Chrysler Airflow is often cited as an example of the unwillingness of the public in accepting automobiles with aerodynamic shapes.

Figure 3.2: Chrysler Airflow Coupe 1934

The Chrysler Airflow demonstrates that automobiles in the 1930s were aerodynamically streamlined also for reasons other than speed. Reduced use of fuel was emphasized as one of the streamlined design's multiple advantages.

In 1950's, due to the smaller proportions of vehicles in Europe, angular bodies were adopted less frequently for mass-produced automobiles, and when rear fins were included, they were significantly smaller. European aerodynamic concept vehicles, such as the Alfa Romeo BAT (Berlinetta Aerodinamica Tecnica) series, maintained the curvaceous body styles that extended to the rear fins.

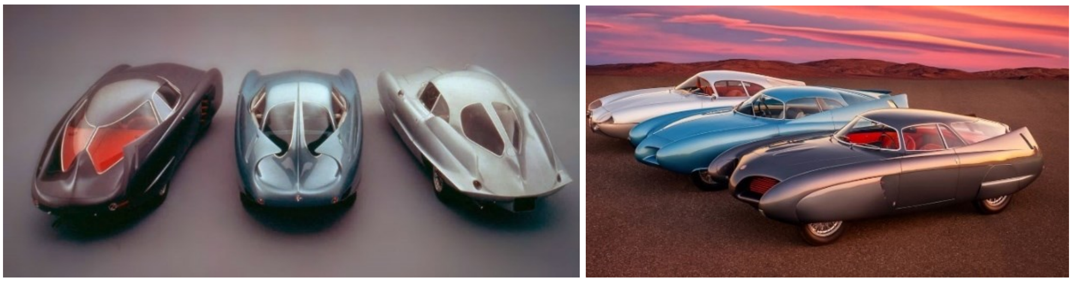

Figure 3.3: Alfa Romeo BAT 5, BAT 7, BAT 9

Alfa Romeo contracted the services of Bertone to develop a total of three BAT prototype vehicles seen in the aforementioned image. These vehicles were designed with careful attention to the impact of aerodynamic drag, following thorough research conducted on the subject matter. Every automobile was manufactured using a particular Alfa Romeo 1900 chassis. The first automobile, BAT 5, was introduced at the 1953 Turin auto show with a drag coefficient of C_D=0.23. The BAT 7 along with BAT 9 were unveiled during the Turin Auto Shows in the years 1954 and 1955, respectively.

With a drag coefficient of C_D=0.19, BAT 7 represented the top level of aerodynamic development in the series, whereas BAT 9 demonstrated an evolution that was closer to a production sports car.

The gradual reduction of aerodynamic drag for passenger cars is illustrated in the graph below. The passed nature of the curve depicts the advancements in testing technology and the legislative requirements for improved fuel economy and lower emissions.

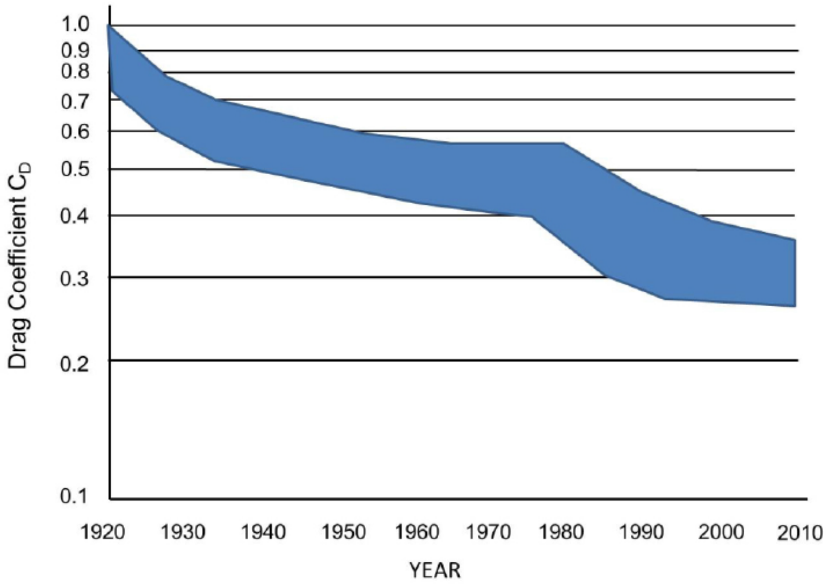

Figure 3.4: Reduction of passenger car drag coefficient in a 90-year period (1920-2010)

Many of the shape requirements needed to attain low drag are already present in all ready existing passenger vehicles. C and D class vehicles, including the BMW E90(C_D=0.26) and Mercedes E-Class coupe(C_D=0.24), are equipped with features such as roof curvature, boat-tailing, tyre coverage, optimal trunk lid positioning, separation-controlling features, and low-drag door mirrors.

Figure 3.5: BMW 3 Series Sedan E90 and Mercedes E-class Coupe

Thus, it appears feasible to achieve relatively low drag while maintaining the appearance of a conventional passenger car. In fact, it could be argued that these forms have been "masked" through the use of feature lines, glazing, exterior ornamentation, and proportions. With the aid of styling, aerodynamic requirements could be integrated at the outset of the design process. For some manufacturers, their corporate visual identity and styling elements also contribute to a more aerodynamic shape.

3.2 Add-on devices effect in vehicle aerodynamics

Add-on devices installation on a car's body design play a significant role in reducing vehicle drag force, therefore improving fuel and energy efficiency.

The analysis of the study carried out on XAM 2.0 (eXtreme Automotive Mobility), the prototype created by the H2politO team at Politecnico di Torino for participation in the urban concept segment of the Shell Ecomarathon Competition, provides a clearer understanding of the approach being discussed [27].

The aim of this study is to decrease the aerodynamic drag of a prototype city car by the implementation of conventional aerodynamic components, such as a spoiler, finlets, rear underbody, front bumper, and rear dam, and wheel cover. The study begins with a computational fluid dynamics (CFD) analysis conducted on the first version of the XAM 2.0 (eXtreme Automotive Mobility) vehicle. Subsequently, the sections of the vehicle that are deemed crucial are examined for potential enhancements in aerodynamics. A computational fluid dynamics (CFD) analysis is conducted to investigate the aerodynamics of a vehicle. The purpose of this analysis is to develop various add-on features that will be constructed and afterwards tested in the Pininfarina Wind tunnel.

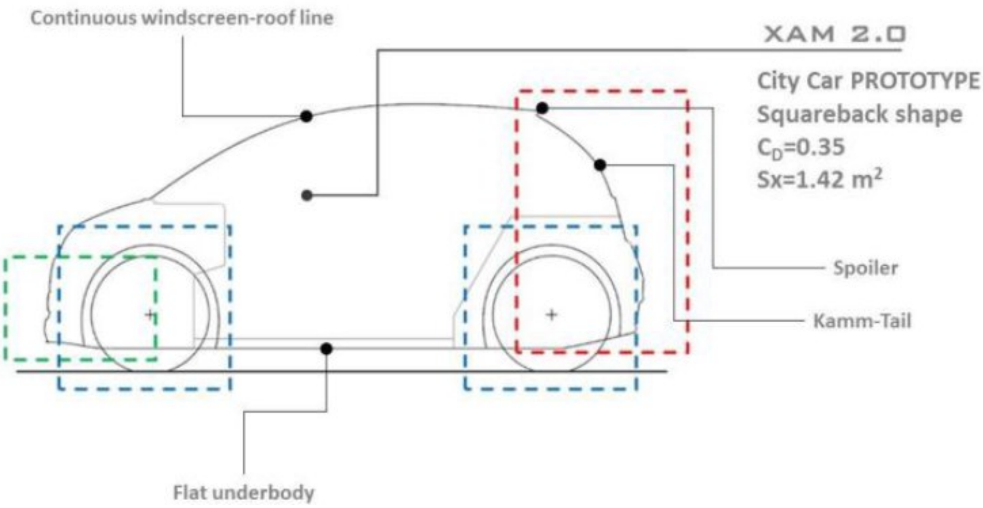

Figure 3.6: Sketch of the XAM 2.0 baseline model and areas impacted by modifications (squares).

The initial model displayed notable aerodynamic characteristics, specifically designed to minimize drag. These features include a seamless connection between the windshield and roof, which reduces disturbances in the uppermost region of the windshield where it meets the roof.

Additionally, a spoiler is incorporated to effectively separate the air stream from the roof, thereby minimizing wake dissipation. Furthermore, the vehicle's underbody is flat and the wheel arches are covered, preventing the formation of flow-dissipating vortexes caused by the mechanical system of the vehicle.

The drag coefficient (C_D), which is of the basic model, as determined by wind tunnel testing, is 0.35 at a speed of 50 km/h, with a frontal area measuring 1.42 m2. Following the initial examination of the baseline model, CAD versions of the aerodynamic components (specifically, the rear diffuser, and front bumper, spoiler, and finlets) are generated using Alias software by Autodesk. These models are then incorporated into the virtual model of STAR-CCM+ software, where multiple computational fluid dynamics (CFD) simulations are conducted to evaluate the efficacy of the implemented changes.

Subsequently, the impact of the aerodynamic features analyzed through computational fluid dynamics (CFD) is assessed in practical conditions. These features are fabricated using rapid prototyping technological advances and affixed to the vehicle. Subsequently, a series of physical tests is conducted inside the Pininfarina Wind Tunnel to verify their efficacy in minimizing drag.

Based on a benchmark evaluation of the most effective aerodynamic solutions implemented on road cars, the recommended features include a rear diffuser, frontal bumper, and spoiler, finlets, lokari dams, and wheel shields. It should be noted that the last two items were exclusively tested within the confines of an actual wind tunnel. The primary function of the first component is to prevent the passage of air underneath the vehicle from entering the wheel properly, thus minimizing disruptions to the wheels. On the other hand, the wheel shield serves to mitigate the turbulence that is caused by the rotation of the wheels.

In the context of producing the CFD-studied features, a selection of technologies and materials was made, taking into account the optimal balance between mechanical strength, cost, weight, quality, and shape. The bumper has been constructed using carbon-fiber material due to its specific size, placement, and shape. In contrast, the spoiler, finlets, and lokari dam have been manufactured using ABS material through the utilization of rapid-prototyping technology. This approach ensured the attainment of desired qualities at a reduced cost. The diffuser, on the other hand, is constructed using a machined block of foam, which is subsequently filled with fissures. Following the completion of the production process, a red paint is applied to all the characteristics of the car in order to emphasize them in relation to the other parts, as depicted in the accompanying image.

Figure 3.7: In a wind tunnel test, the vehicle's aerodynamic components (from left to right: bumper, spoiler and finlets, lokari dams, diffuser) are mounted.

Wind tunnel experiments were conducted at the Pininfarina winds tunnel facility. The floor of the facility features a specialized conveyor belt known as the T-belt. These experiments replicate the ground effect phenomenon observed in real-world scenarios. The wheels are situated on roller that are linked to a three-axis dynamometer. This section outlines the three fundamental elements of the force exerted on the vehicle as a result of aerodynamic influences, namely lift, drag, and skin friction. Additionally, it highlights the interaction of these forces with the ground as they pass through the vehicle's wheels.

The experiments were conducted at three distinct velocities (30, 50, and 70 km/h), employing a 14-hole probe positioned 150 mm after the vehicle to collect data. Similar to the approach employed in the computational fluid dynamics (CFD) study, each aerodynamic characteristic is systematically implemented in the wind tunnel, building upon the most optimal configuration from the preceding iteration. In total, a set of 51 vehicle configurations equipped with aerodynamic characteristics were subjected to testing. The acquisition data time for each test was consistently set at 40 seconds, while the Basic Suction System (BSS) and T-Belt devices were enabled for all tests. The TGS, which stands for Turbulence Generation System equipment, on the other hand, is not operational. The findings from the wind tunnel experiment conducted at a velocity of 70 km/h are presented in the upcoming figure.

The optimal outcome of the automobile fitted with a rear diffuser, bumper, spoiler, and finlets is indicated in red. This configuration represents the ultimate design that was subjected to computational fluid dynamics (CFD) testing.

The optimal result found in both real-world and virtual cases is:
– CFD analysis: Spoiler at 6 inches, Finlets at 4 inches, Bumper, and Rear Diffuser
– Wind Tunnel analysis: Spoiler at 9◦ + Finlets at 8◦ + Bumper + Rear Diffuser

AERO FEATURE	CFD	WIND TUNNEL	∆CFD-WT
REAR DIFFUSER	-2.85%	-3.12%	0.27
FRONT BUMPER	-2.56%	-2.64%	0.09
SPOILER	-1.13% (at 6°)	-0.90% (at 9°)	0.23
FINLETS	-0.76% (at 4°)	-1.21% (at 8°)	0.45
TOTAL	**-7.30%**	**-7.86%**	**0.56**

Table 3.1: C_D reduction correlation between CFD and WT

Figure 3.8: Best results at 70 km/h in the wind tunnel

The observed decrease in drag can be attributed to the adoption of conventional aerodynamic characteristics, which are supplementary components added to the vehicle after its outward shape has been established. The merging of elegant designs and aerodynamic functions through active or passive airflow control systems could lead to additional advancements in aerodynamics. These considerations should be incorporated into the initial conceptualization of the car.

The analyzed characteristics enable a significant decrease in the coefficient of drag (C_D) by over 7% in the most optimized configuration, resulting in a corresponding reduction in fuel consumption of approximately 2 kilometers per liter.

Chapter 4

Introduction to vehicle aerodynamics CFD Simulation

4.1 History and applications

CFD is now recognized as a subset of computer-aided engineering (CAE) tools used widely in every field. Its way of modeling fluid flow phenomena provides designers and engineers the capability of a simulated wind tunnel on their desktop. The field of computational fluid dynamics (CFD) has undergone significant advancements that beyond the original conceptualizations of pioneers such as Navier, Stokes, and Da Vinci. Computational Fluid Dynamics (CFD) has grown as an integral component in the design process of aerodynamic and hydrodynamic systems, including various modes of transportation such as airplanes, trains, vehicles, rockets, ships, and submarines. Furthermore, CFD finds applicability in the optimization of any mobile machinery or manufacturing procedure invented by humankind. But how did it reach this point?

Heraclitus' ancient postulate "Everything flows" was the consequence of his philosophical thinking. Archimedes made significant contributions to the sciences of static mechanics and hydrostatics, as well as developing methods for measuring the density and volumes of things [28].

The return of these concepts in Southern Europe occurred during the Renaissance, wherein notable artists such as Leonardo Da Vinci began to meticulously investigate the natural phenomena of fluids and flow.As mentioned in the preceding chapter, the latter part of the 17th Century in England witnessed the emergence of Isaac Newton as a prominent figure after to Leonardo.

During the 19th and 18th centuries, scholars made notable contributions in their efforts to quantitatively characterize the dynamics of fluid motion. The renowned equation known as Bernoulli's equation was derived by Daniel Bernoulli, whereas Euler's equations, which represent the principles of momentum conservation for an inviscid fluids as well as mass conservation, were proposed by Leonhard Euler. During this period, two notable individuals made significant contributions to the study of fluid flow. These individuals were Claude Louis Marie Henry Navier, a French scholar, and George Gabriel Stokes, an Irish scholar. Navier and Stokes incorporated the concept of viscous transport within the Euler's equations, leading to the development of the renowned Navier-Stokes equation.

This set of differential mathematical equations published approximately two centuries ago serve as the foundation for the contemporary computational fluid dynamics (CFD) activity.

These equations contain several expressions related to the conservation of momentum, mass, pressure, species, and turbulence. The equations exhibit a high degree of interdependence and complexity, rendering their resolution impractical until the emergence of advanced computer technology in the years 1960 and 1970. Consequently, it was only during this period that real flow issues could be effectively addressed within manageable timeframes.

Jean Le Rond d'Alembert, Joseph Louis Lagrange, Siméon-Denis Poisson, Jean Louis Marie Poiseuille, John William Rayleigh, Osborne Reynolds,M. Maurice Couette, and Pierre Simon de Laplace were also influential 19th-century theorists of fluid flow [28].

During the first decades of the 20th century, significant efforts were dedicated to the improvement and development of theories related to boundary layers along with turbulence in flow of fluids. Ludwig Prandtl's significant contributions include the proposal of a boundary layer theories, the development of the mixing length principle, advancements in understanding compressible flows, the introduction of the Prandtl number, and numerous other contributions that are now widely accepted and utilized in various fields. Theodore von Karman conducted an analysis on the phenomenon that is currently referred to by the name von Karman vortex street. Geoffrey Ingram Taylor is credited with proposing a statistical theory about turbulence and introducing the concept of the Taylor microscale. The idea of Kolmogorov scales and a universal energy spectrum within turbulent motion was introduced by Andrey Nikolaevich Kolmogorov. Additionally, George Keith Batchelor made important additions to the study of homogeneous turbulence.The question of who conducted the very initial CFD calculations in a modern sense is a subject of debate. However, it is widely acknowledged that Lewis Fry Richardson from the Kingdom of England was the pioneer in developing the very first numerical weather forecasting system.

Thom conducted the first numerical calculation regarding flow past the cylinder in 1933, which was subsequently reported in England. In 1953, Kawaguti in Japan was able to obtain an explanation for flow surrounding a cylinder. This achievement was accomplished through the use of a mechanically desk calculator, with Kawaguti dedicating twenty hours per week over a period of 18 months to complete the work!

In the 1960s, the theoretical division of NASA at Los Alamos in the United States contributed a number of numerical methods that are still used in CFD today, including Particle-In-Cell (PIC), Marker-and-Cell (MAC), Vorticity-Stream function methods, Arbitrary Lagrangian-Eulerian (ALE) methods, and the ubiquitous k - e turbulence model.

In the 1970s, a team led by D. Brian Spalding at Imperial College, London, created Parabolic flow codes (GENMIX), Vorticity-Stream function based codes, the SIMPLE algorithm, and the TEACH code, as well as the current form of the k-e equations. They went on to devise Upwind differencing, 'Eddy break-up', and 'presumed pdf' combustion models.

1980 witnessed the publication of "Numerical Heat Transfer and Fluid Flow" by Suhas V. Patankar, possibly the most notable book on CFD to date and the source of a thousand CFD codes.

Beginning in the early 1980s, a significant number of commercial CFD codes entered the open market. Instead of maintaining to develop in-house CFD codes, prominent companies around the world started adopting the use of commercial CFD software.

Therefore, commercial computational fluid dynamics (CFD) software relies on complicated sets of non-linear mathematical expressions. The equations are solved through an iterative process using sophisticated computer algorithms that are integrated into Computational Fluid Dynamics (CFD) software. These equations are solved iteratively using the CFD software's embedded complex computer algorithms. And now, the cumulative effect of such software is to enable the user to computationally model any flow field, given the geometry of the object being modeled, the physics and chemistry, and some initial flow conditions. The outputs generated by CFD software can be analyzed through various graphical representations, such as color plots displaying velocity vectors, pressure contours, lines representing constant flow field properties, or through "hard" numerical data and X-Y graphs.

Let's start further investigating on applications of CFD tool [29].

CFD Simulation for Cavitation Prevention

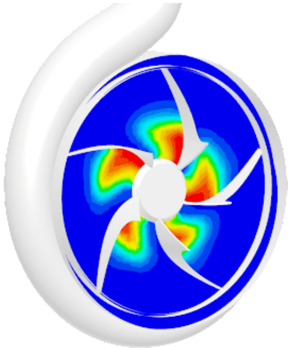

Figure 4.1: Cavitation simulation example using CFD

Cavitation simulation via CFD can assist engineers in establishing mini thresholds that would be hard to detect in the real world. They can evaluate at a very fine grade to compare alternative products and designs in order to enhance their projects' adaptability, durability, and safety.

Simulating Rotating Equipment using CFD

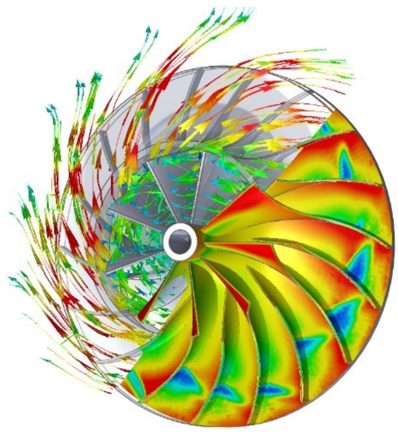

Figure 4.2: Load acting case simulation example of a rotating equipment using CFD

Using CFD simulation, a variety of design variables can be evaluated to determine the optimal design for rotating machinery. Compressors, steam pumps, gas turbines, and turbo-expanders share a common characteristic: a cyclic load acting on the structure.

Simulation of Laminar and Turbulent Flow Using CFD

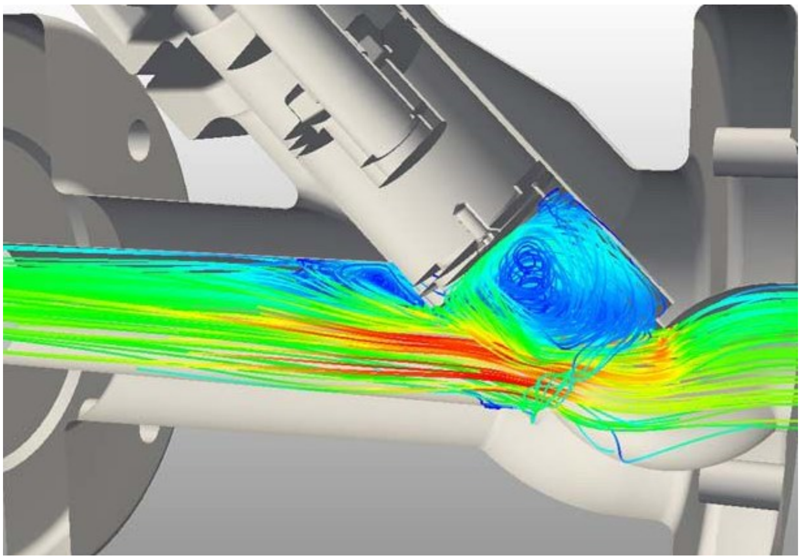

Figure 4.3: Laminar and turbulent flow simulation example using CFD

CFD simulations employ turbulence models to determine the influence of turbulence on a CAD-engineered design.

CFD Simulation Applications for Heating, Air Conditioning, and Ventilation (HVAC)

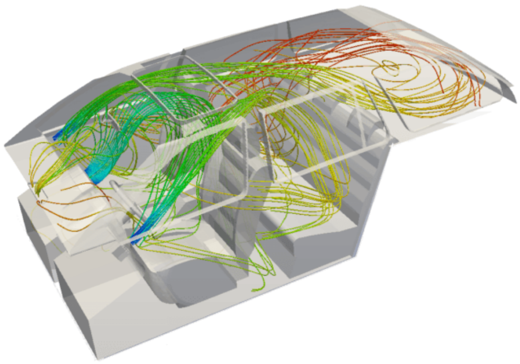

Figure 4.4: HVAC simulation example using CFD

Many manufacturers of HVAC equipment use the CFD simulation to accelerate the prototyping and validation of new designs. Engineers can analyze the prospective functionality of their products in various spaces and configurations using CFD simulation.

Simulation of Batteries with CFD

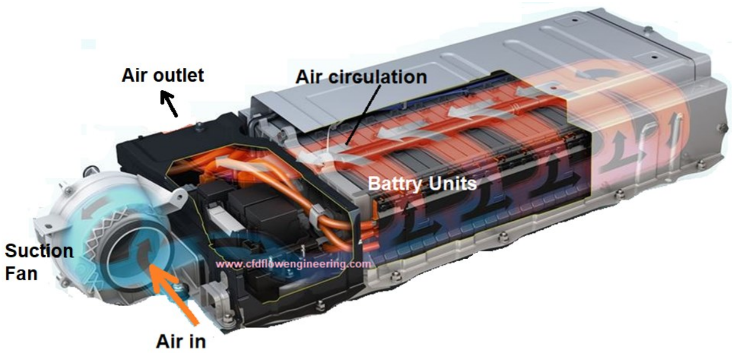

Figure 4.5: Battery operation system simulation example using CFD

CFD simulation can play a significant role in improving the performance and safety of batteries by reducing the amount of time and resources required for physical testing. CFD software can assist battery manufacturers in visualizing in 3D and resolving issues related to rapid discharging, increased ambient heating, and overcharging, which affect not only battery life but also consumer safety.

CFD Simulation of Aerodynamics

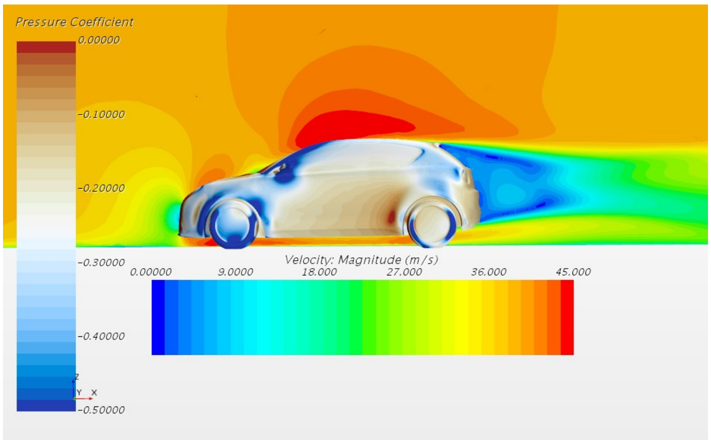

Figure 4.6: Car aerodynamics simulation example using CFD

Automobile designers, aerospace engineers, and manufacturers of sports equipment all use simulation software to reduce drag and improve the performance of their products. Simulation enables engineers to test dozens or hundreds of iterations of very small design modifications to optimize performance, prior to going into production. This is in addition to the ability to design aerodynamic products without investing in many physical prototypes.

Simulation of Heat Transfer and Thermal Management Using CFD

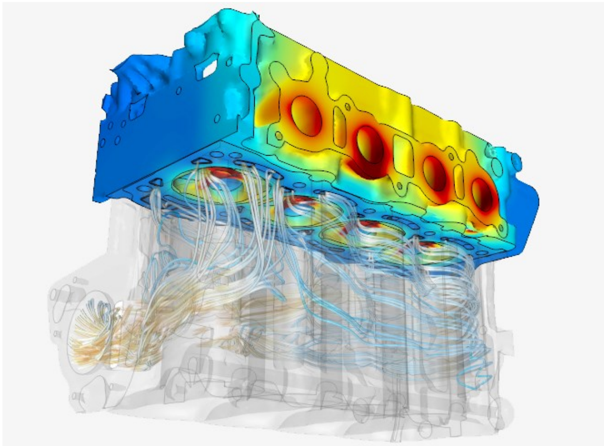

Figure 4.7: Heat transfer simulation example using CFD

In order to optimize heat transfer in automobile engine designs, etc., CFD simulation is utilized. It is also essential to a multitude of other simulation categories (such as HVAC) where heat transfer is an integral part of a product's primary function.

Simulation of Pipes and Valves with CFD

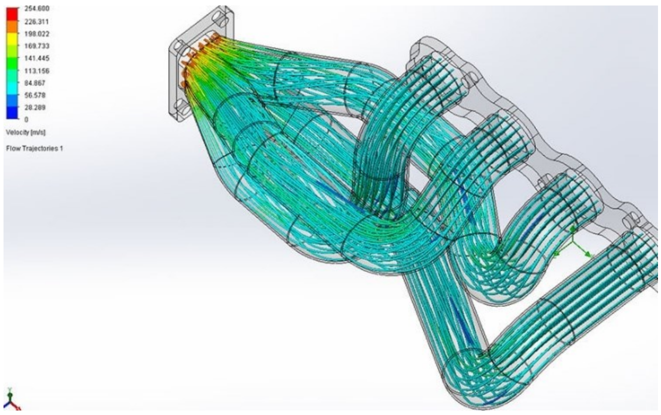

Figure 4.8: Pipes functioning simulation example using CFD

Engineers can model the functioning of an entire system of pipelines or isolate a single component (such as a valve) using CFD simulation to reduce the likelihood of failure. CFD simulation could also be used to analyze the failure of deteriorating infrastructure, providing engineers with a more accurate picture of what transpired.

Electronics cooling simulation using CFD

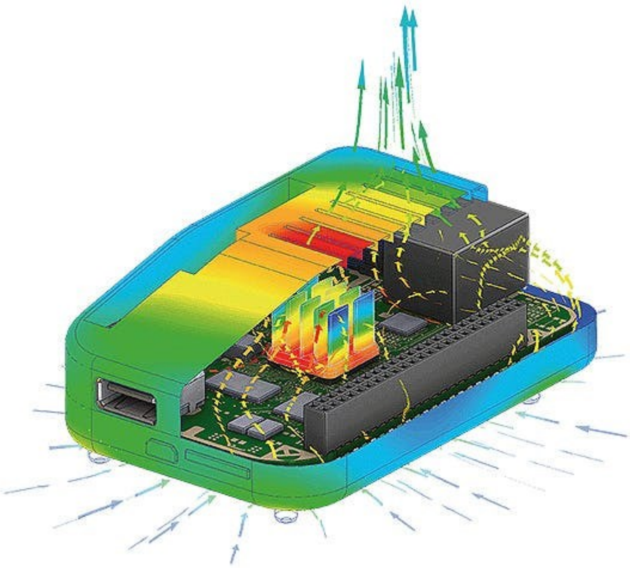

Figure 4.9: Electronics cooling simulation example using CFD

All modern electronics require some type of heat management, be it heatsinks, vents, ventilation or a thermal components. This is because GPUs and CPUs begin to malfunction when they become overheated. These components must be kept relatively cold (usually below 85°C) to maintain performance. Without extensive simulation or testing, electronic manufacturers would frequently release products that failed due to overheating (such as phones, toys, computer processors, etc.).

CFD simulation can be utilized to evaluate and organize the optimal placement of components (heatsink, fan, etc.) to prevent overheating of sensitive chips.

CFD Simulation of Reacting Flows and Combustion

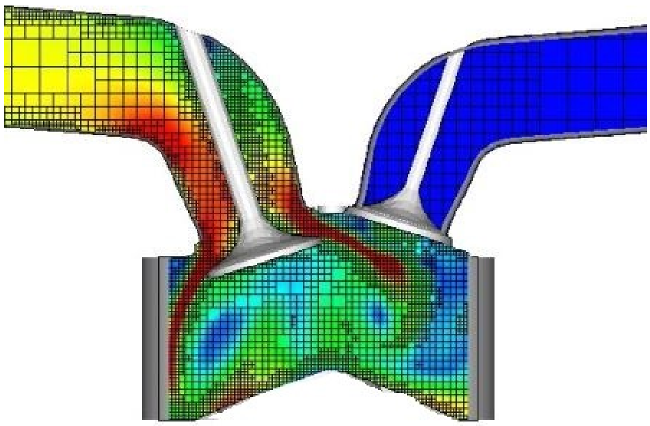

Figure 4.10: Combustion process simulation example using CFD

Understanding the fundamental chemistry and physics of reacting flows is essential to improving energy efficiency, fuel flexibility, and decreasing emissions in the aerospace, automotive, and other industries.

In this regard, CFD simulation performs well. It can deal with complex, multi-physics problems, such as reacting flows, without costly physical testing, providing manufacturers with insights about their products that would be virtually impossible to calculate manually.

However, there are numerous other applications of CFD tools in the modern world, including simulations of turbomachinery, incompressible and compressible fluids, and many others. Evidently, the majority of CFD software will not update our CAD model. Instead, they provide us with a "vector field" that indicates the necessary deformation for optimizing our model. The designer is then responsible for manually modifying the design.

4.2 Computational Fluid Dynamics process

In a CFD software analysis, the calculation of fluid flow and its physical properties, including velocity, pressure, viscosity and density, and temperature, is performed using specified operating conditions. Simultaneous calculation of these quantities is necessary to obtain a precise and real solution [30].

Each commercial and/or open-source CFD utility relies on a mathematical model and numerical method to predict the desired flow physics. The Navier-Stokes (N-S) equations drive the majority of CFD software. While the majority of terms in the Navier-Stokes equations remain constant, additional terms can be added or subtracted depending on the physics. If heat transfer, phase change, or chemical reactions must be considered, for instance, additional terms will be added to the governing equations.

In order to perform a precise and successful CFD analysis, it is crucial to take into account the appropriate operating conditions, numerical methods, and physics. If this is done correctly, performance insights can be obtained rapidly, resulting in a final product that performs better and is more efficient.

The CFD analysis procedure consists of three main steps: pre-processing, processing, and post-processing [30].

Pre-processing is the initial step in CFD simulation, which, if performed correctly, can aid in defining the simulation's parameters precisely.

The first step in this process involves identifying the specific domain that is of interest and dividing it into smaller segments. This includes tasks such as preparing the geometry, creating a mesh, defining material properties, and establishing boundary conditions and layers.

Processing includes solving the governing equations associated to physics of a flow using a software like ANSYS FLUENT, ANSYS CFX, Star CCM, CFD++, OpenFOAM etc..

Every simulation process within a CFD program must follow to a predetermined series of steps. Simulations are, after all, a series of steps that must be followed in order to prevent getting stuck or getting error messages in the following stages.

Each of these stages is interdependent on the others, which is why pre-processing is so important to begin with.

Post-processing is a procedure in which, after obtaining results from the simulation phase, the results are analyzed. Using available methods such as vector charts, contour charts, data curves, and streamlines, this can be performed. Thus, we will receive precise data and graphic representations.

4.3 Pre-processing

The accuracy of a CFD analysis depends on the skill and precision of the person implementing it. The designer's ability to set up the model accurately during the pre-processing stage is crucial, as any errors or oversights at this stage will have an impact on the analysis results in later stages. It is essential that the geometric model is devoid of errors or flaw, and common issues include:

- Model gaps
- Absent or overlaying faces
- Open geometries such as free faces and edges

The model should be a "closed" solid, free of the aforementioned defects, after preparation. Once this is accomplished, there are a few additional stages to the preprocessing for CFD analysis.

Problem Evaluation

Problem evaluation is the foundation of our simulation; we need to know the problems we are planning to solve in order to establish our objective and settings accurately.

Then consider the physics of the problem we are attempting to solve. Is the objective to analyze the characteristics of both turbulent and laminar flow in blood? Or are we assessing the heat transmission of a newly designed head of cylinders?

We will be able to avoid incorrect simulation results by defining our model with the correct parameters if our problem analysis is precise.

Geometry

After defining our physics, we must construct a two- or three-dimensional geometry based on our problem analysis.

There are some problems which can be resolved in two dimensions, saving time and money by reducing computational requirements.

Meshing

Because improper meshing can have a cumulative impact on our analysis, it requires careful consideration. This step involves dividing the physical domain of our environment into cells or control volumes.

The cells are characterized by the flow of fluid calculations that govern them. Designers must rely on their knowledge and assumptions to determine the flow profiles of these cells.

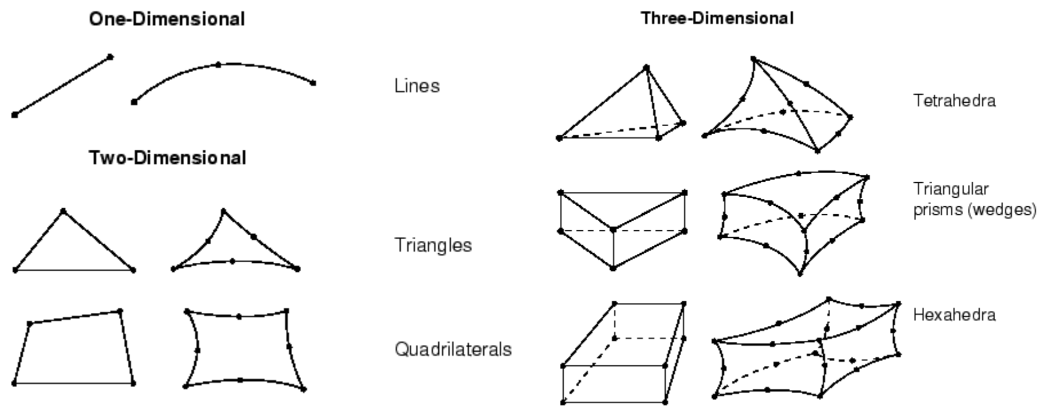

Figure 4.11: Cell shapes

Typically, engineers conduct convergence studies to establish the optimal equilibrium between accuracy and available simulation resources. This can be achieved by restricting high mesh density to the load path and areas of interest in the model.

For an accurate assessment of stress, denser meshes are also required for shapes, such as fillet radii, that are subjected to significant amounts of concentrated stress.

In regions that are further away from stress concentrations or load paths, larger and less dense elements can be used to create the mesh.

The purpose is to create meshes that accurately depict the geometric shape without wasting simulation resources. As a result, meshes are typically denser (composed of finer elements) in regions where calculations are important.

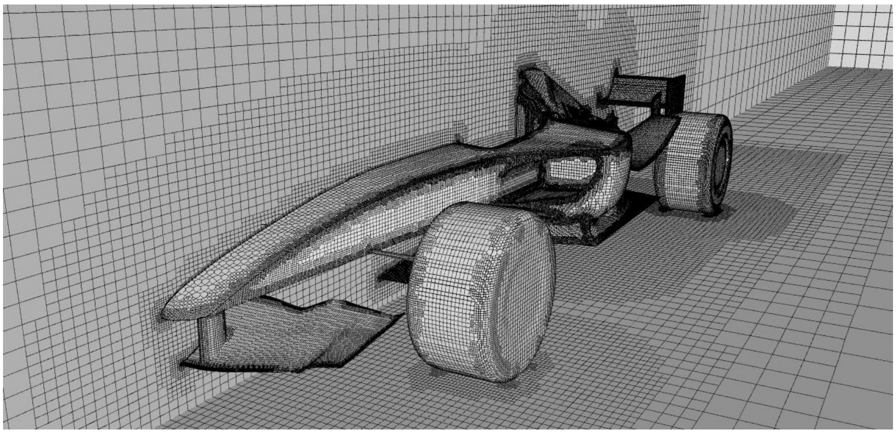

Figure 4.12: Irregular mesh density in F1 car

Setup Solver

During this phase, we will be tasked with defining the conditions of the problems we intend to solve. For instance, boundary conditions, turbulence model and fluid type.

Because the numerical solutions are preconfigured, it is crucial to understand the physics of our problem. Furthermore, we must understand how the method operates. In terms of processing, we can select the processors and iterations required to achieve convergence.

4.4 Processing

The Navier–Stokes equations, which describe many single-phase fluid flows such as gas or liquid, form the fundamental basis for nearly all CFD problems. Once the simulation is started in a software the equations below are solved in a steady-state or transient phase in an iterative way:

$$\frac{\partial \rho}{\partial t} + \frac{\partial(\rho u)}{\partial x} + \frac{\partial(\rho v)}{\partial y} + \frac{\partial(\rho w)}{\partial z} = 0 \tag{4.1}$$

Above equation represents the three-dimensional unsteady form of the **Navier–Stokes continuity equation**. Where x, y and z represents spatial coordinates of some domain. u, v and w represents velocity components in x, y and z direction respectively. ρ represents density.

$$\frac{\partial(\rho u)}{\partial t} + \frac{\partial(\rho u^2)}{\partial x} + \frac{\partial(\rho uv)}{\partial y} + \frac{\partial(\rho uw)}{\partial z} = -\frac{\partial(p)}{\partial x} + \frac{1}{Re_f}\left[\frac{\partial \tau_{xx}}{\partial x} + \frac{\partial \tau_{xy}}{\partial y} + \frac{\partial \tau_{xz}}{\partial z}\right] \tag{4.2}$$

$$\frac{\partial(\rho v)}{\partial t} + \frac{\partial(\rho uv)}{\partial x} + \frac{\partial(\rho v^2)}{\partial y} + \frac{\partial(\rho vw)}{\partial z} = -\frac{\partial(p)}{\partial y} + \frac{1}{Re_f}\left[\frac{\partial \tau_{xy}}{\partial x} + \frac{\partial \tau_{yy}}{\partial y} + \frac{\partial \tau_{yz}}{\partial z}\right] \tag{4.3}$$

$$\frac{\partial(\rho w)}{\partial t} + \frac{\partial(\rho uw)}{\partial x} + \frac{\partial(\rho vw)}{\partial y} + \frac{\partial(\rho w^2)}{\partial z} = -\frac{\partial(p)}{\partial z} + \frac{1}{Re_f}\left[\frac{\partial \tau_{xz}}{\partial x} + \frac{\partial \tau_{yz}}{\partial y} + \frac{\partial \tau_{zz}}{\partial z}\right] \tag{4.4}$$

Above three equations represent the three-dimensional unsteady form of the **Navier–Stokes momentum equations** in x, y and z directions. p is a pressure and τ is a stress tensor [31].

$$\frac{\partial(E_T)}{\partial t} + \frac{\partial(uE_T)}{\partial x} + \frac{\partial(vE_T)}{\partial y} + \frac{\partial(wE_T)}{\partial z} = -\frac{\partial(up)}{\partial x} - \frac{\partial(vp)}{\partial y} - \frac{\partial(wp)}{\partial z} - \frac{1}{Re_f}\frac{1}{Pr_f}\left[\frac{\partial q_x}{\partial x} + \frac{\partial q_y}{\partial y} + \frac{\partial q_z}{\partial z}\right] + \frac{1}{Re_f}\left[\frac{\partial}{\partial x}(u\tau_{xx} + v\tau_{xy} + w\tau_{xz}) + \frac{\partial}{\partial y}(u\tau_{xy} + v\tau_{yy} + w\tau_{yz}) + \frac{\partial}{\partial z}(u\tau_{xz} + v\tau_{yz} + w\tau_{zz})\right] \tag{4.5}$$

Above equation represents the three-dimensional unsteady form of the **Navier–Stokes energy equation.** q is a heat flux.

For a wide variety of fluid mechanics problems, however, it is not necessary to solve the full governing Navier-Stokes equations (4.1)-(4.5). The RANS (Reynolds Averaged Navier-Stokes) equations are a simplified set of equations obtained by averaging the terms of the equations [32]. The use of RANS necessitates the inclusion of a so-called turbulence model. Simulation of nearly all everyday phenomena and industrial processes, where the flow is described as turbulent, requires turbulence models. The selection and implementation of the turbulence model has a substantial effect on the simulation's outcome and computational time.

In most instances, the flow around certain objects is highly unstable and turbulent. In addition to a turbulence model, it is necessary to solve the governing equations for each mesh cell at a series of discrete times, as the flow field varies over time. Stepping forward in time requires a temporal discretization in addition to the spatial discretization.

4.5 Post-processing

As the demand for simplified access to real-world modeling increases, enhanced data visualization of CFD results promotes more informed decisions. Large datasets generated by CFD simulations are represented effectively through post-processing.

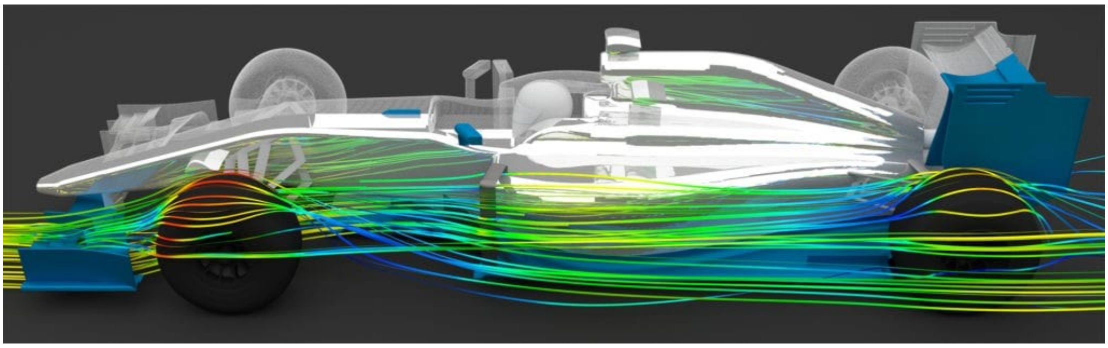

Figure 4.13: Streamlines representing an airflow around the F1 car attained using N-S equations

To be more precise, post-processing is the extraction of meaningful results from solution data obtained from solving each simulation problem. Two main types of post-processing exist: qualitative, or visualization-based, and quantitative, or number-based.

There are numerous methods for post-processing simulation output data in order to assess and extract the appropriate data. Among them are:

- Plots produced by result control items
- Tables and graphs for specific outputs
- Graphic post-processing for 3D simulation result visualization
- Download of the result database for on-site post-processing

Chapter 5

Evaluation of the aerodynamic performance of the Tesla Cybertruck with CFD Simulation

5.1 Geometrical model

To start our simulation, we obtained a 3D model of the Tesla Cybertruck [33]. This unofficial car geometry with flat underbody may not be accurate in the details nor include the most recent modifications to the vehicle, but it should be sufficient for evaluating the aerodynamic performance of this design as a whole.

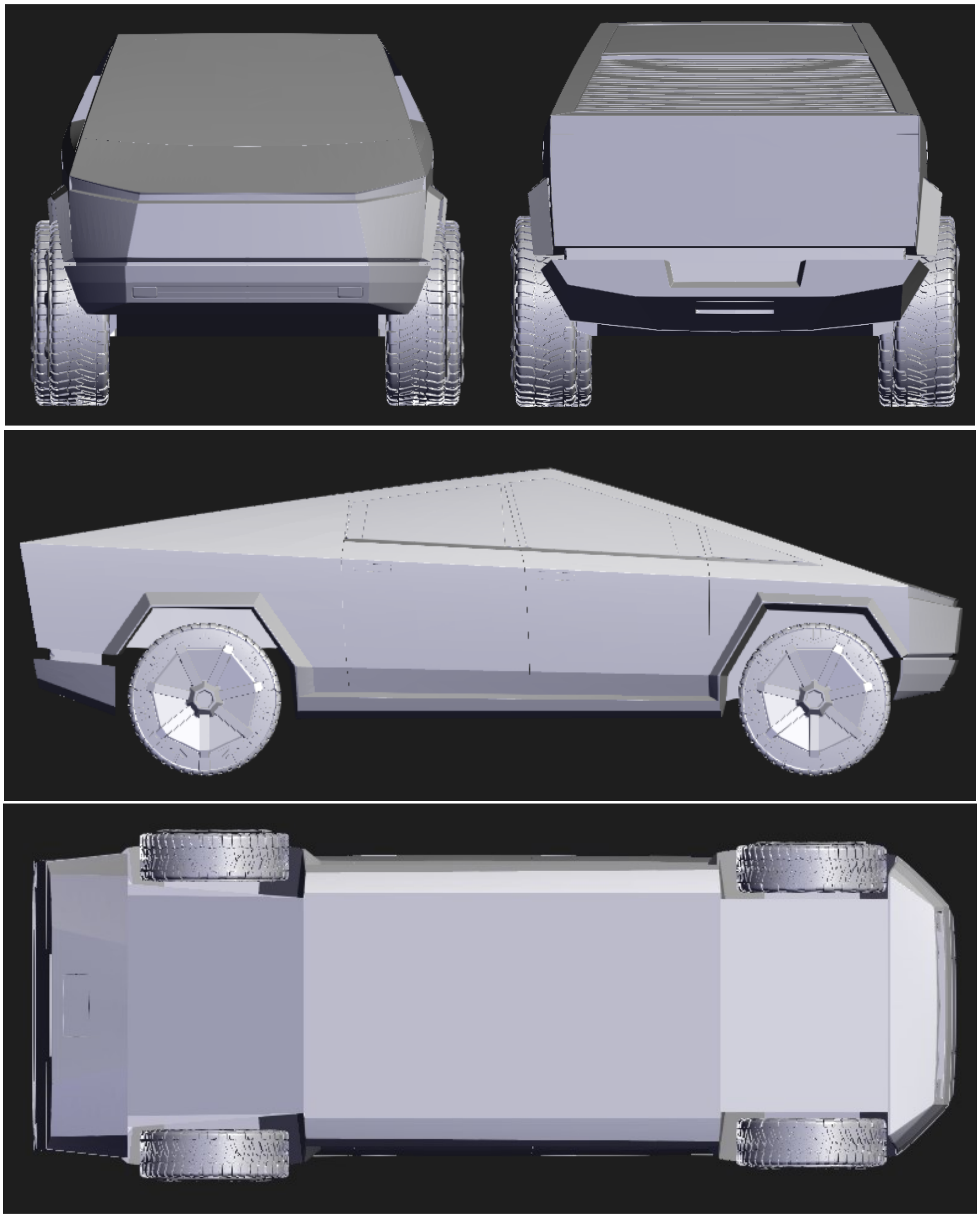

Figure 5.1: Front, back, side and underbody view of Tesla Cybertruck 3D model

In order to start our work, we have imported our geometry into the STAR CCM+:

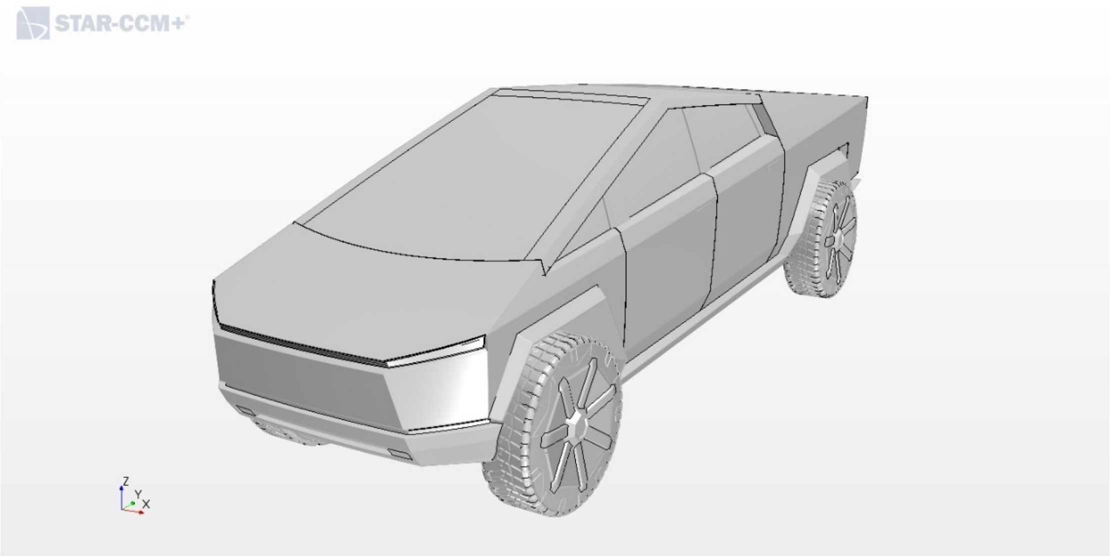

Figure 5.2: Imported geometry on STAR CCM+

After importing our geometry, there are usually some steps to execute. To be more specific, to start working on this geometry, it should not contain penetrations and be a water-tight model. Since our geometry resulted in a large number of errors during the surface repair process in STAR CCM+, we decided to perform a surface wrapping operation:

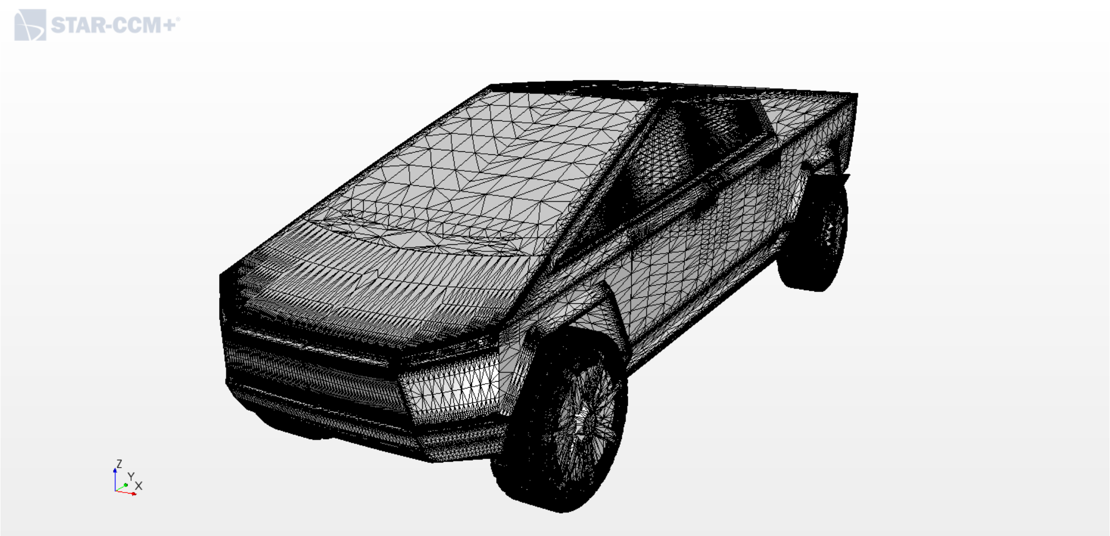

Figure 5.3: Surface wrapped geometry on STAR CCM+

The next work to be done was to create a domain, which will perform in our CFD simulation as a wind tunnel, and it defined a finite region for us in which we had set up a flow of interest:

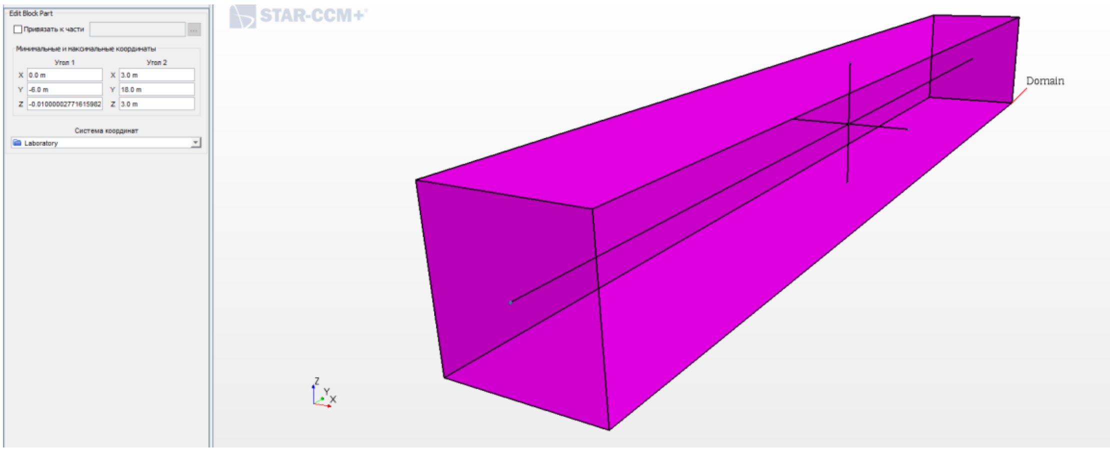

Figure 5.4: Domain on STAR CCM+

Following this, the next operation was a Boolean subtract operation to imprint the half of the car model into the domain, since the air flows inside a domain and we want it to flow around a car. Additionally, in our case, symmetrical geometry was considered a necessity due to our computational device's hardware limitations:

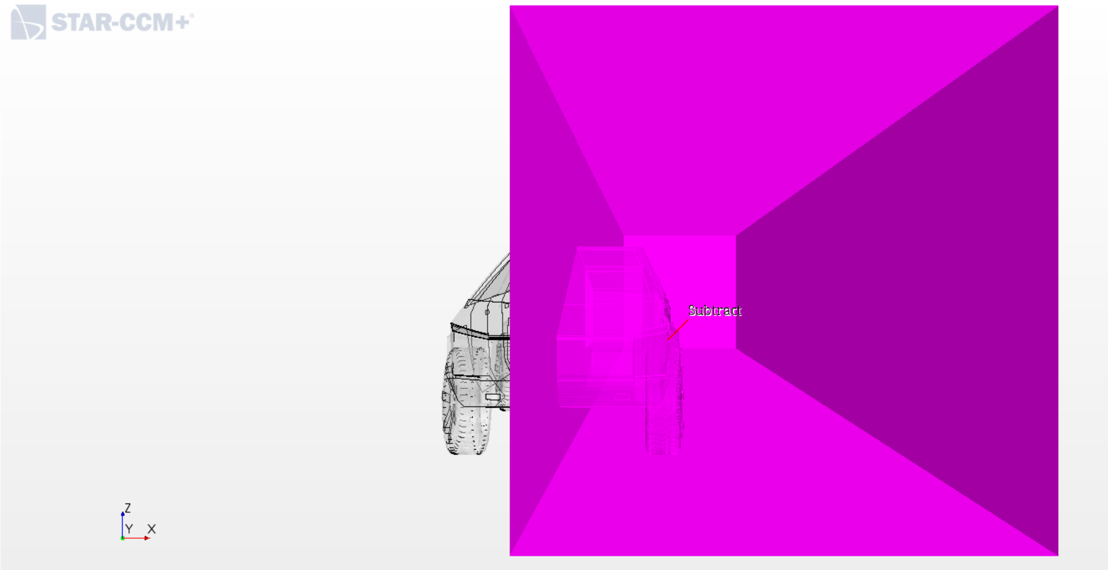

Figure 5.5: Subtracted region which includes half of the car and domain on STAR CCM+

But before switching to meshing, we needed to create a region where air could flow. In our case, it is the subtracting part. So, in this region, we assigned boundary layers and other setup parameters for region parts:

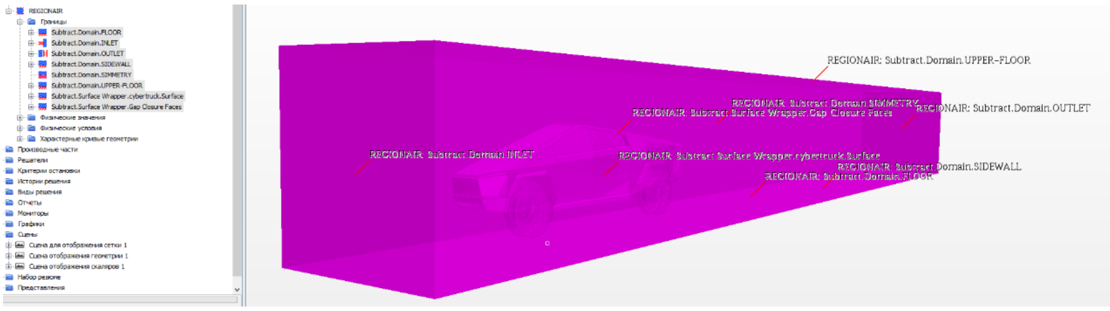

Figure 5.6: Assigned regions for parts on STAR CCM+

5.2 Meshing

What we did next was set up surface mesh and volume mesh. By meshing, we enable our CFD software to compute results related to aerodynamic performance, as all of them can be computed numerically. Then we enabled the following meshers:

- Surface remesher
- Automatic surface repair
- Polyhedral mesher
- Thin mesher
- Prism layer mesher

Subsequently, we set up the below-indicated default controls for our automated mesh operation:

- Base size: 25 mm
- CAD projection: yes
- Target surface size: 50% relative to base
- Minimum surface size: 25% relative to base
- Surface curvature: Enabled (36 pts/circle, max. 200 pts/circle, 0.005 m curvature deviation distance)
- Number of prism layers: 3
- Prism layer total thickness: 10 mm
- Mesh density: 0.7 (1.3 growth factor)

By going further, to increase the quality of our results, we refined regions where the highest gradients occur and specified boundary layers where we introduced prism layers:

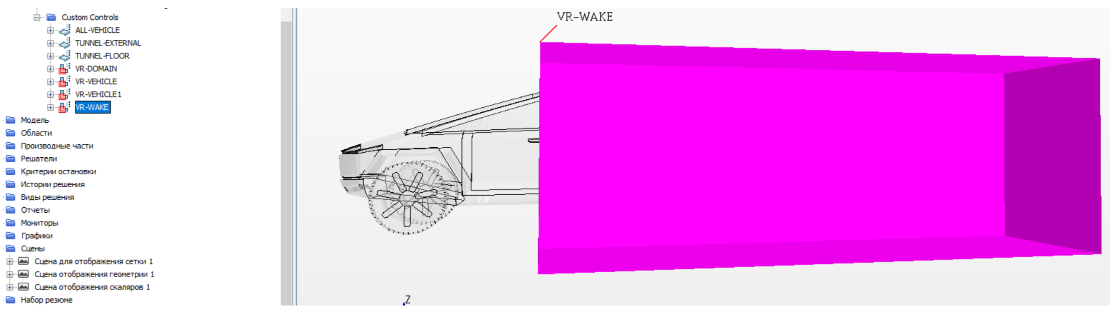

Figure 5.7: Volume refinement of the wake region on STAR CCM+

At the end, when all parameters for an automated mesh had been included, our geometry was ready for a mesh operation to be executed. By performing that, we get the following result:

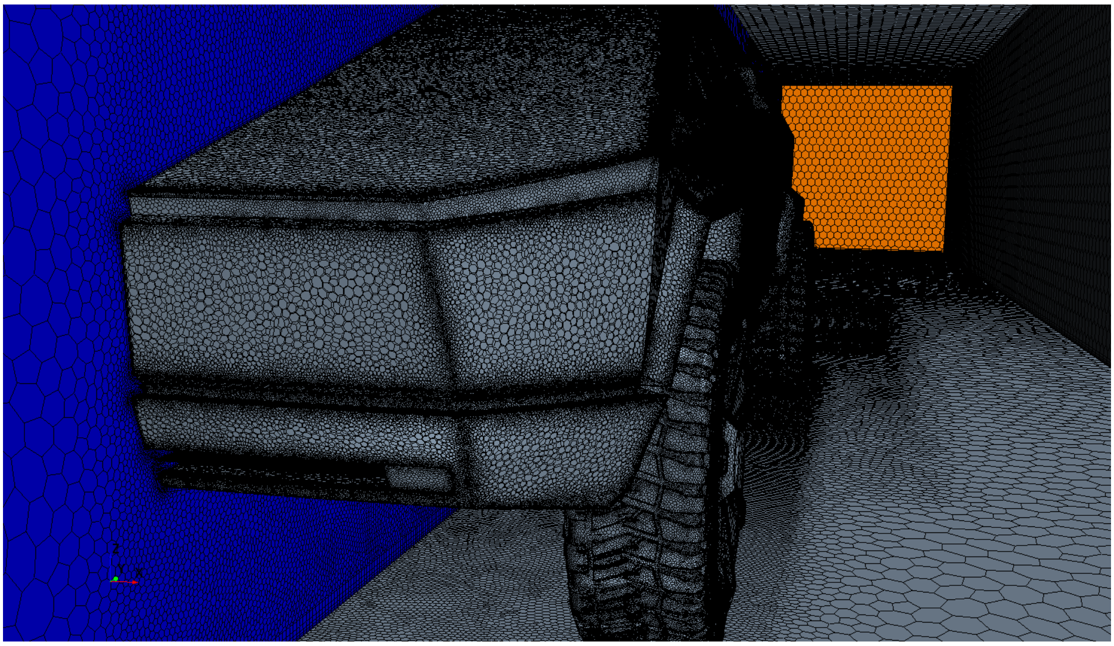

Figure 5.8: Meshed geometry on STAR CCM+

5.3 Processing

Physics setup

Our next step was to setup physics of our problem, starting with indication of external aerodynamics parameters of our car and setting models:

- Three dimensional
- Steady
- Gas
- Segregated flow
- Constant density
- Turbulent
- K-epsilon
- Cell quality remediation

Following this, we had set up:

1) Test conditions:

- RRS OFF – wheels are not rotating, and ground is fixed

2) Properties of air:

- Density: 1.225 Kg/m3

- Dynamic viscosity: 1.79E-5 Pa-s

3) Flow initial conditions:

- Velocity: [0.0; 20.0; 0.0] m/s

4) Boundary conditions for each surface:

- Inlet velocity for wind tunnel: 38.89 m/s
- Outlet pressure for wind tunnel: 0 Pa
- Front Floor of wind tunnel: slip condition
- Rear Floor of wind tunnel: no slip condition
- Half plane type of wind tunnel: symmetry
- Top floor of wind tunnel: slip condition
- Side plane of wind tunnel: slip condition
- All other boundaries: no slip wall

Then we had initialized a solution .

Reports setup

First report to set up was a frontal area report and we executed it by selecting all faces of our vehicle and direction of calculation (direction of flow).

Secondly, we had set up and generated reports for drag and lift force by adding all parts of our vehicle and specifying normalization values.

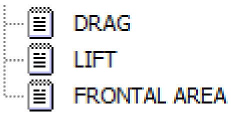

Finally, we had run the simulation .

5.4 Post-processing

After running out our simulation we can evaluate the solution through an opened monitors. One of this monitor is the residuls plot. Residuals plot is representation of convergence of a numerical solution while iterations are performed. This simulation had run for 700 iterations. Residuals are tending down, as the solution is converging, nearly close to 0.001 which is acceptable for industrial cases.

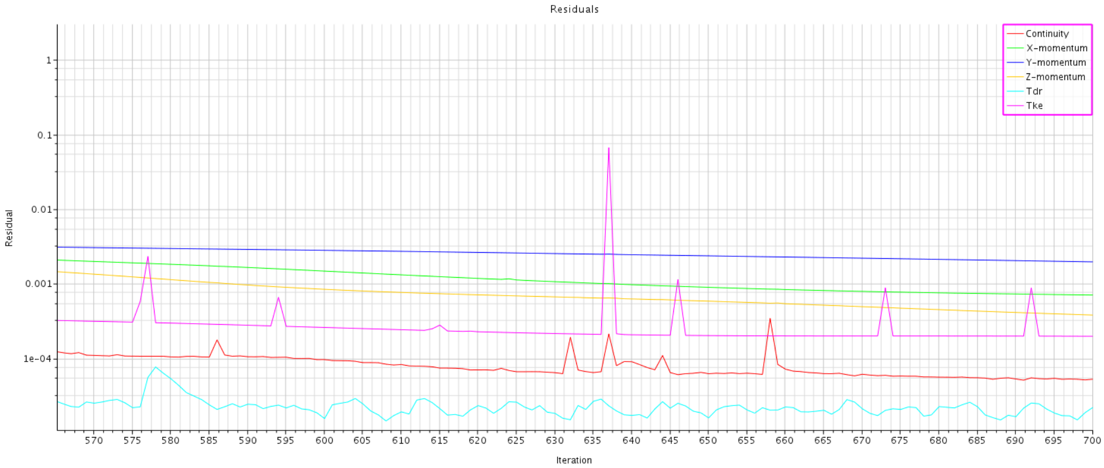

Figure 5.9: Residuals convergence plot of final steps on STAR CCM+

Force convergence is also important and consequently we can identify their convergence to a specific value after some steps in Drag monitor.

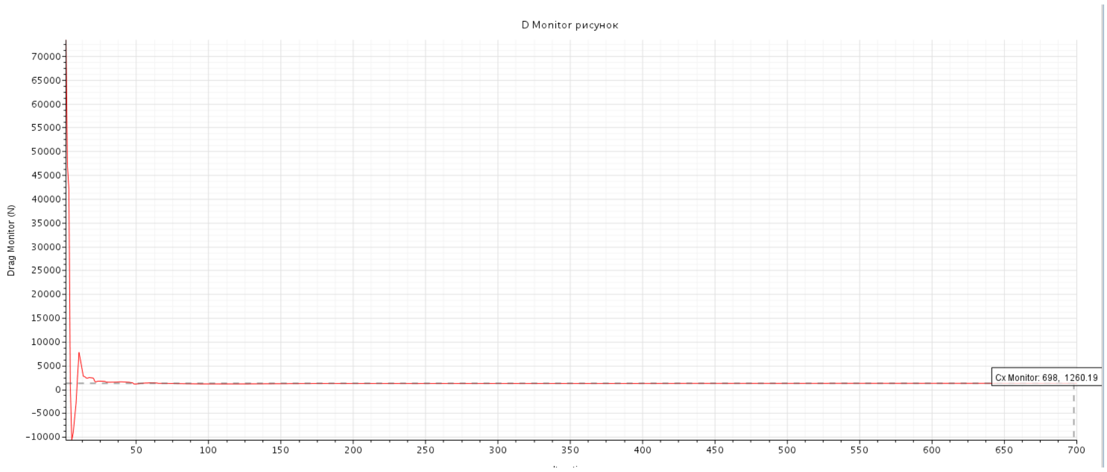

Figure 5.10: Force of drag convergence plot on STAR CCM+

In our case we had obtained the value of drag force equal to 1260 N, and if we want to optain the final value of drag coefficient, we can use formula (2.1) and obtain a value of **0.807** for a drag coefficient.

In addition to this we had obtained the lift force of our vehicle equal to 782 N, and if we want to optain the final value of lift coefficient, we can use formula (2.6) and obtain a value of **0.501** for a lift coefficient.

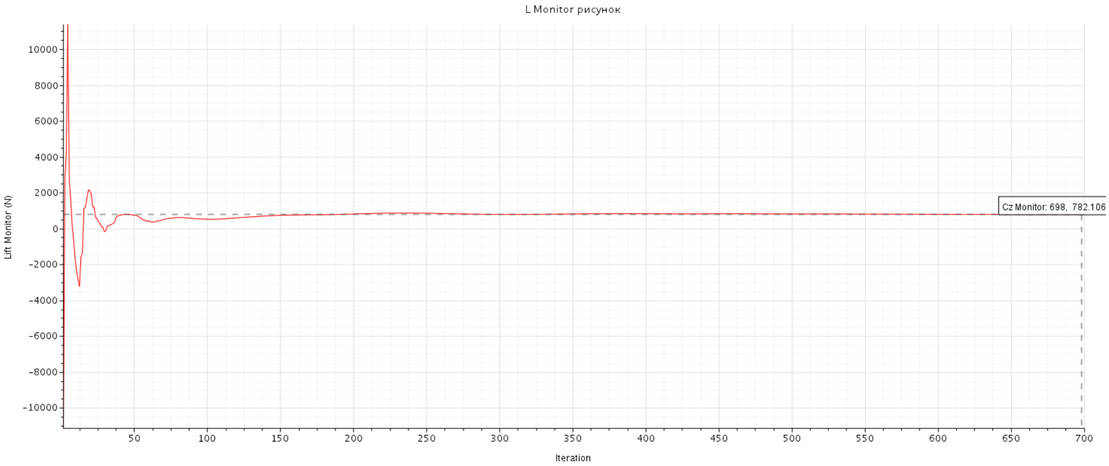

Figure 5.11: Force of lift convergence plot on STAR CCM+

Important observations were made on pressure coefficients and velocity monitors.

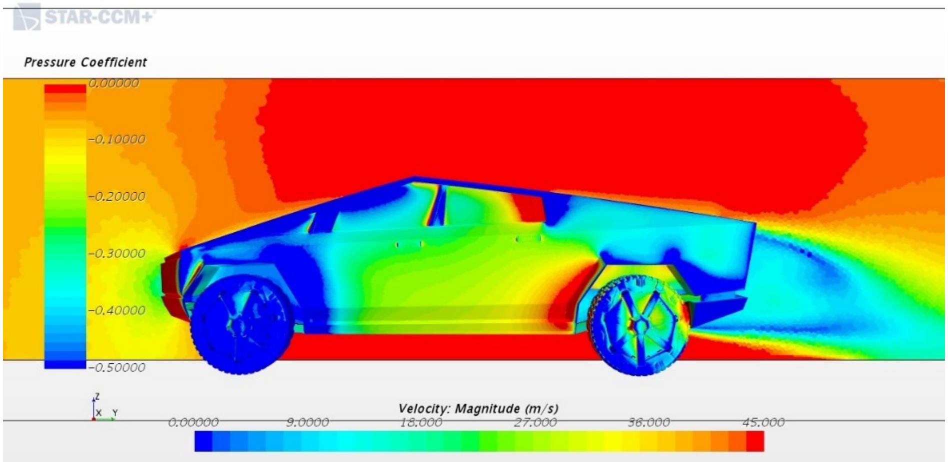

Figure 5.12: Scene of velocity magnitude on the symmetry plane on STAR CCM+ (1)

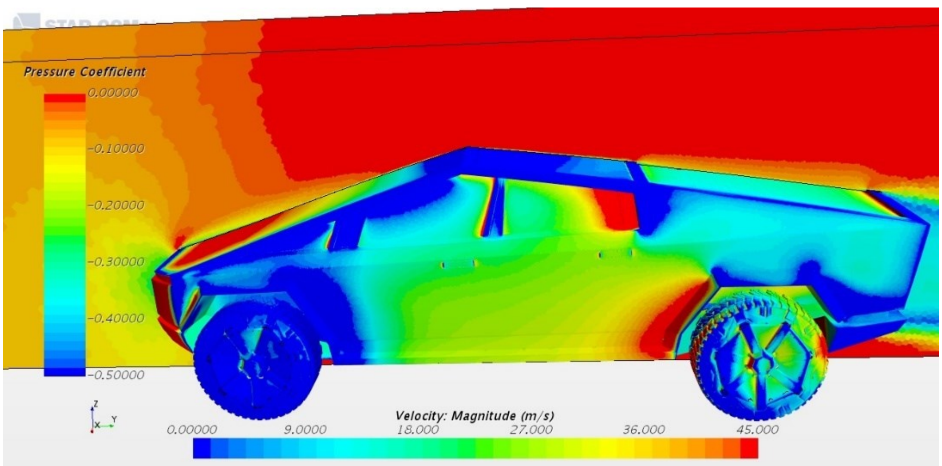

Figure 5.13: Scene of velocity magnitude on the symmetry plane on STAR CCM+ (2)

Above scenes represent velocity plane of the fluid near our vehicle, which is represented in the symmetry plane of our windtunnel. And from this graph we can obtain information about acceleration and separation regions, boundary layer development, shear layers and also wake regions (formed at the rear side of our vehicle).

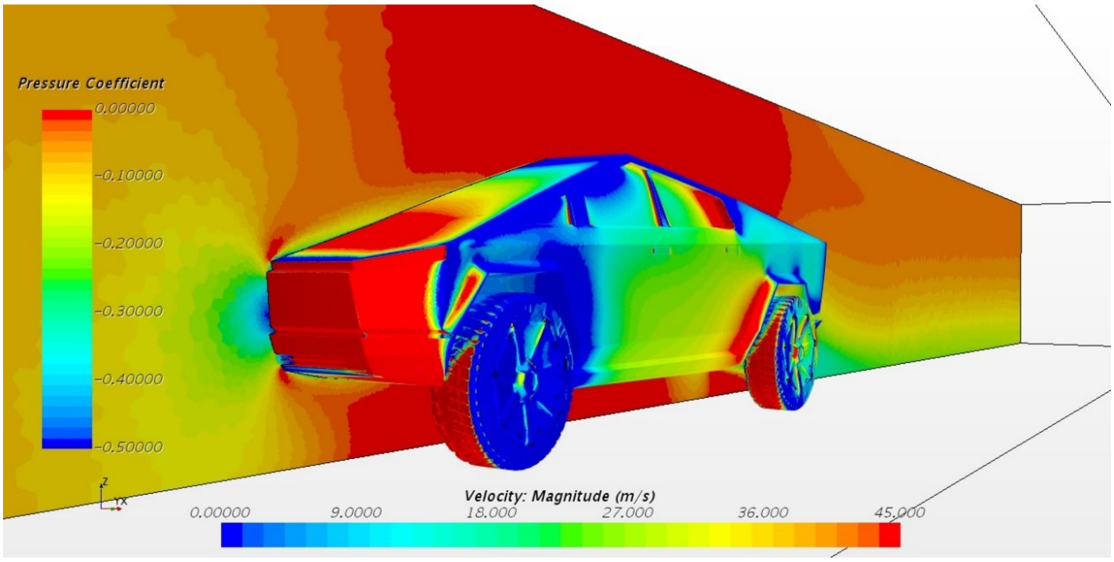

Figure 5.14: Scene of the pressure coefficient on the vehicle on STAR CCM+ (1)

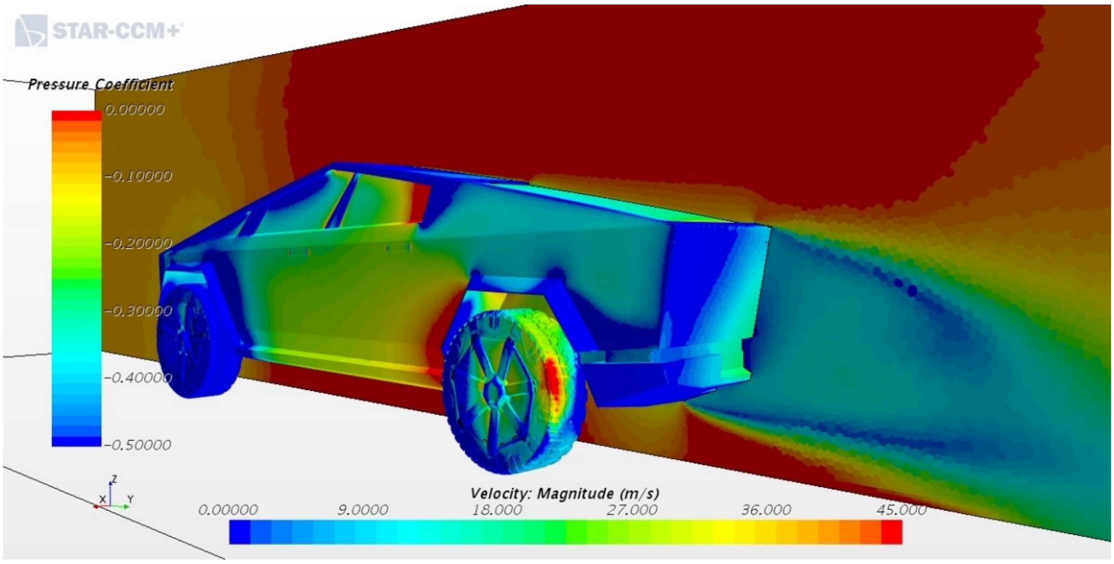

Figure 5.15: Scene of the pressure coefficient on the vehicle on STAR CCM+ (2)

Subsequently, above two scenes represent surface pressure coefficient of the vehicle. The regions with high (vehicle front) and low (vehicle side and rear) pressure coefficients can be identified from this views and vertical bar indicates the magnitude of this coefficient. It is necessary to state that, it is very important variable to evaluate an aerodynamic data, because this is the most important source of drag and lift force generation for passenger cars, and it is common to address around 90% of drag and lift generation to pressure.

Continuing, below scene represents skin friction coefficient displayer scene that is very nice representation of separation lines and wake regions.

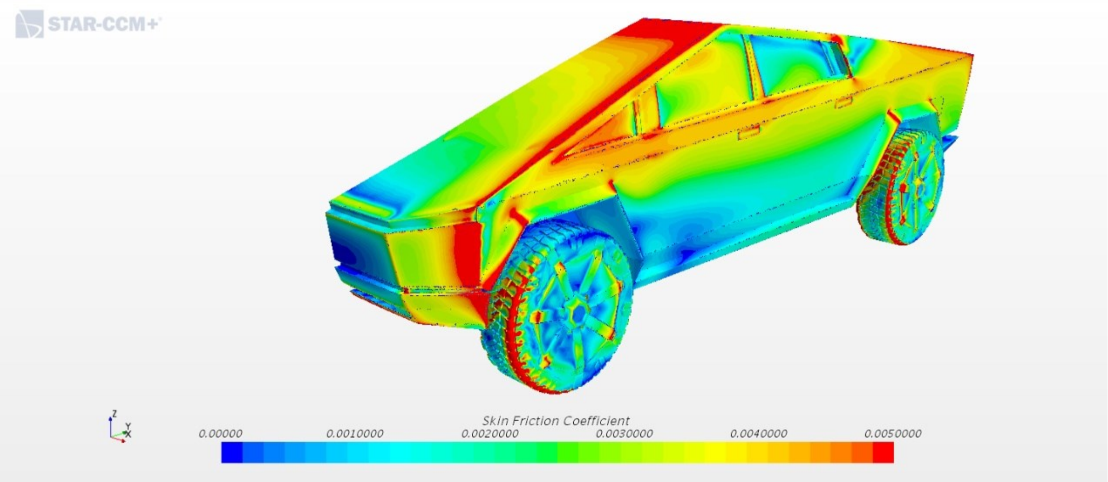

Figure 5.16: Scene of the skin friction coefficient on the vehicle on STAR CCM+ (1)

From above picture we can identify stagnation points in the front side of the front bumper of our vehicle, that is all energy of the air flow is converted into the force in this region. Also, we can identify high velocity flow attached to the side-end of front bumper, A-pillar, roof and partly in tires.

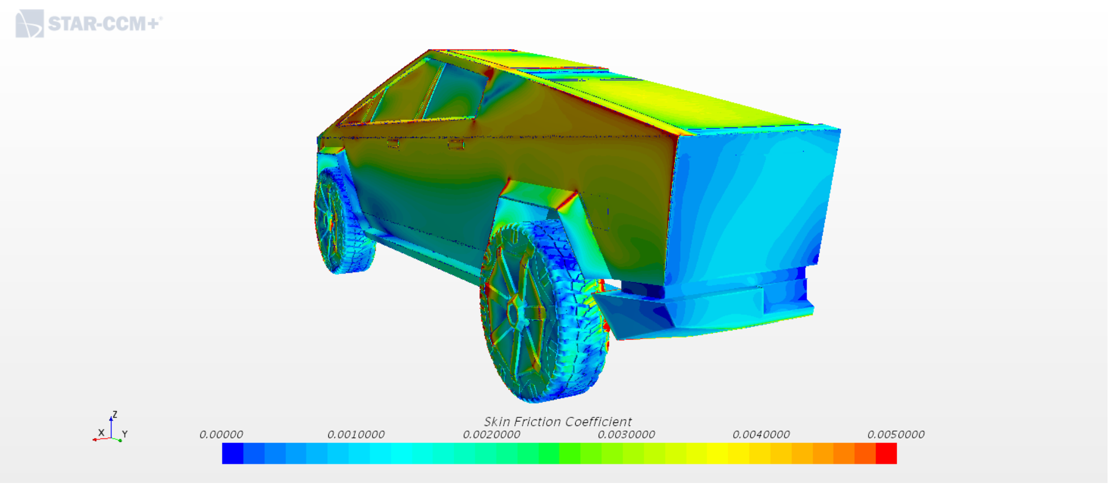

Figure 5.17: Scene of the skin friction coefficient on the vehicle on STAR CCM+ (2)

In the above picture we can visualize transition between high and low skin friction coefficients at the rear side-end that are called separation lines. It is necessary to state that, it is one of the important variable to evaluate an aerodynamic data, because this is a source of drag and lift force generation for passenger cars, and it is common to address less than 10% of drag and lift generation to friction.

Following this we had created total pressure coefficient displayer scene, which is very convenient to visualize all wake regions of our vehicle:

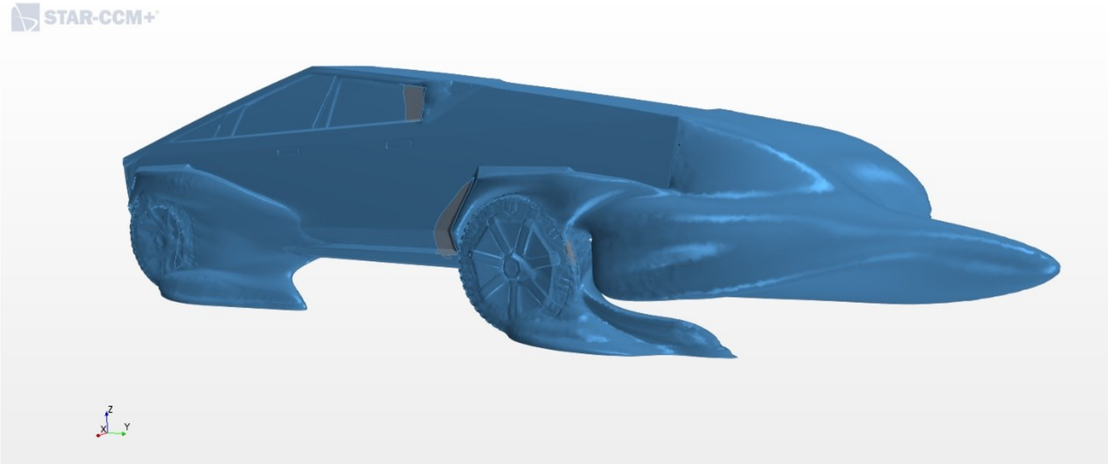

Figure 5.18: Scene of the total pressure coefficient on the vehicle on STAR CCM+ (1)

From above scene we can easily recognize huge rear wake of our vehicle and some wake regions near the wheels. And the transition regions are the same as we had mentioned in skin friction coefficient displayer scene.

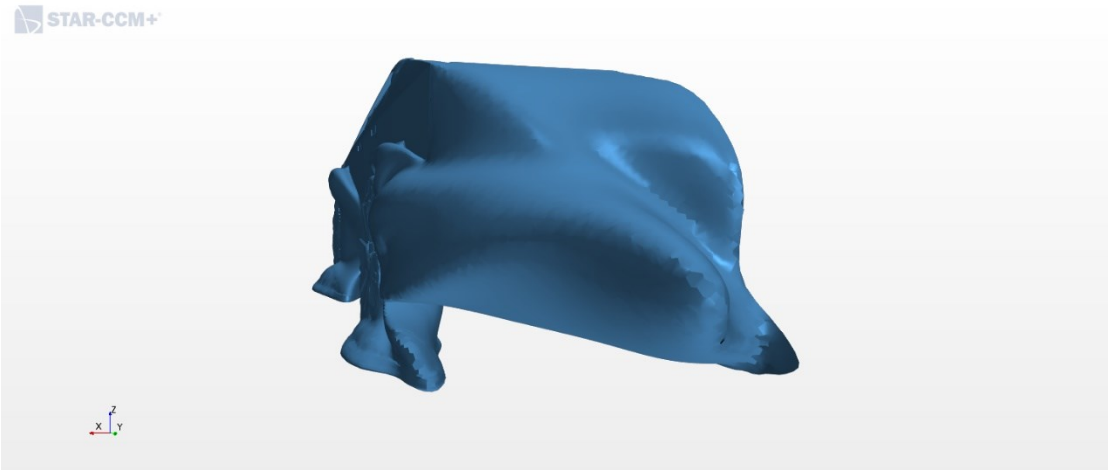

Figure 5.19: Scene of the total pressure coefficient on the vehicle on STAR CCM+ (2)

From above scene we can recognize reduction of wake formation in the vehicle rear center-end due to the shape of the rear-bumper of our vehicle.

Next scene below contains streamlines, that are representing pattern of a velocity field around a vehicle of interest.

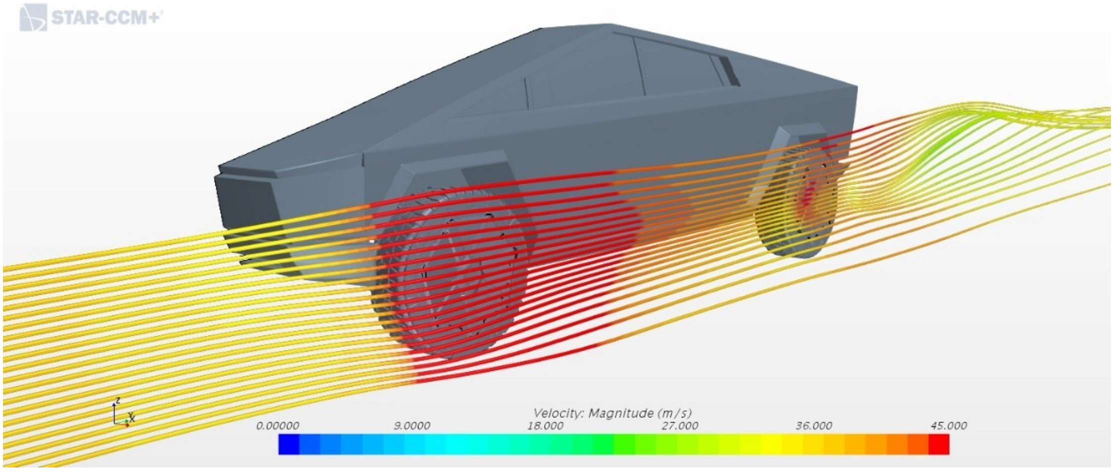

Figure 5.20: Scene of the streamlines representing velocity field pattern around a vehicle wheels on STAR CCM+

And from the above scene we can identify an acceleration at the front part of the tires and the wake region at the back of a vehicle.

Finally, from the last tool we used for post processing, we can visualize drag coefficient development along the vehicle.

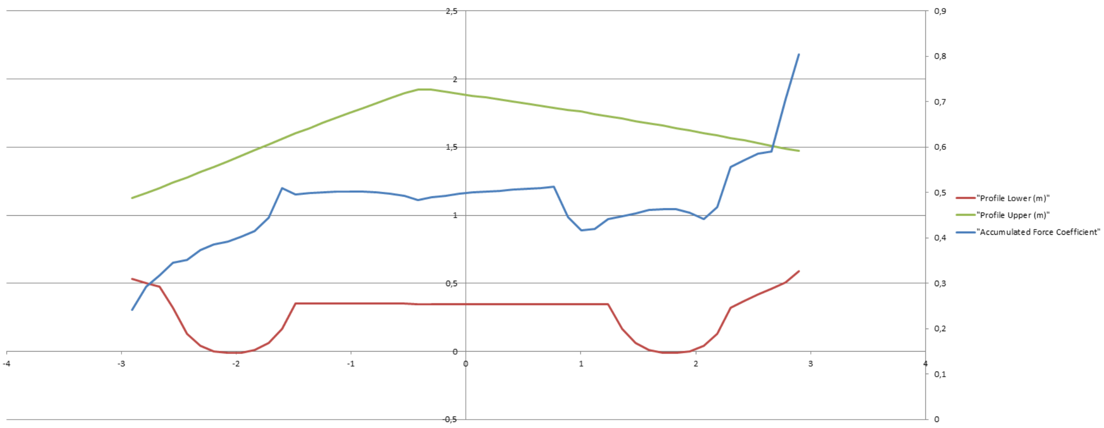

Figure 5.21: Drag coefficient development chart

We generated this chart by using STAR CCM+ for data collection about the drag coefficient development along the vehicle and Microsoft Excel for representation of imported data as a chart.

If we observe this chart, we can recognize drag coefficient plotted along x-axis of a vehicle. That means for each section drag is calculated and made an integral. According to above chart we can see that the blue line representing the regions of drag generation of our vehicle. To be more in detail, we can see drag increase near the region of front wheels. And following the blue line, we can see reduction in drag, probably it is because in this region we have negative value of pressure. By continuing, we can observe initiation of drag increase near rear wheels and finally strong increase in drag at the back of the vehicle due to the negative pressure coefficient.

Chapter 6

Improvement of the aerodynamic performance of the Tesla Cybertruck and its evaluation with CFD Simulation

After identifying a baseline configuration aerodynamic performance, it has arrived time to implement changes on the geometry by installation of default add-on details and figure out improvements by performing a CFD Simulation on STAR CCM+.

6.1 Geometrical model

We have installed front air dam, front and rear wheel spats and rear diffuser to the baseline configuration of a vehicle using SOLIDWORKS tool.

Then, in order to start our work, we have imported our geometry into the STAR CCM+:

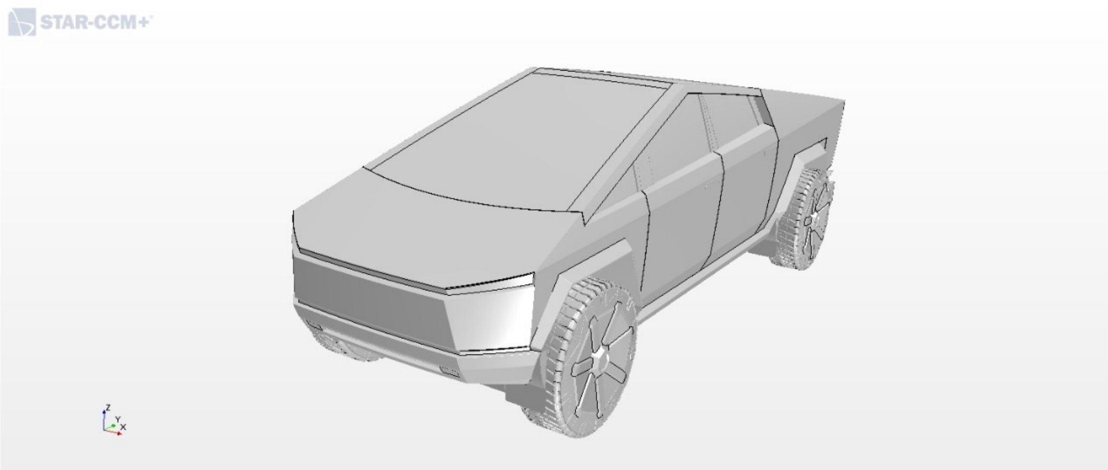

Figure 6.1: Imported geometry on STAR CCM+ with add-on details installed

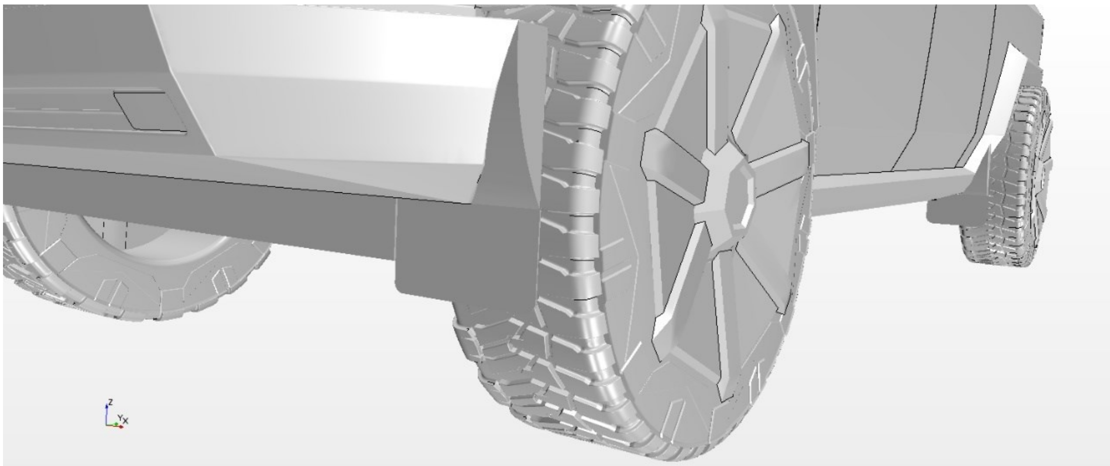

Figure 6.2: Added front air dam and front wheel spats

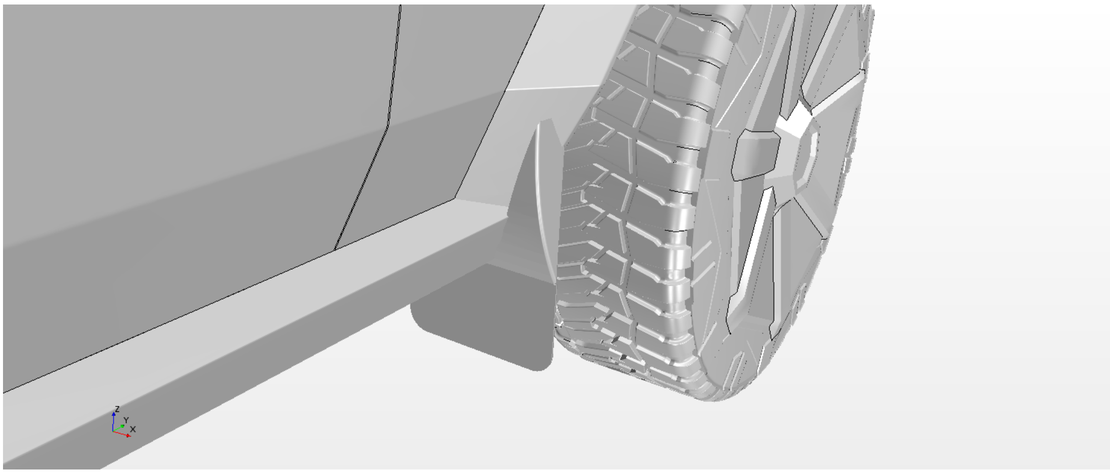

Figure 6.3: Added rear wheel spats

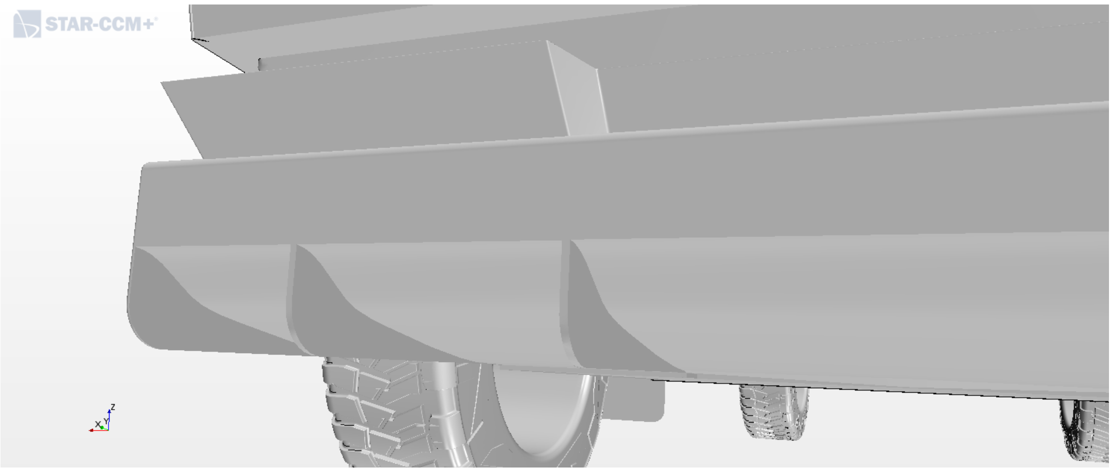

Figure 6.4: Added rear diffuser

After importing our geometry as we already know it should not contain penetrations and be a water-tight model. And again as we had improved our existing geometry, we decided to perform a surface wrapping operation.

The next work was to repeat the same post-processing steps for Geometry and the Region sections as for the baseline configuration:

- Creation of the domain
- Boolean subtract operation
- Assignment of regions for parts

6.2 Meshing

What we did next was set up surface mesh and volume mesh. Then we enabled the following meshers:

- Surface remesher
- Automatic surface repair
- Polyhedral mesher
- Thin mesher
- Prism layer mesher

Subsequently, we set up the below-indicated default controls for our automated mesh operation:

- Base size: 20 mm
- CAD projection: yes
- Target surface size: 50% relative to base
- Minimum surface size: 15% relative to base
- Surface curvature: Enabled (36 pts/circle, max. 200 pts/circle, 0.005 m curvature deviation distance)
- Number of prism layers: 3
- Prism layer total thickness: 10 mm
- Mesh density: 0.7 (1.3 growth factor)

By going further, to increase the quality of our results, we refined regions where the highest gradients occur and specified boundary layers where we introduced prism layers.

At the end, when all parameters for an automated mesh had been included, our geometry was ready for a mesh operation to be executed. By performing that, we get the following result:

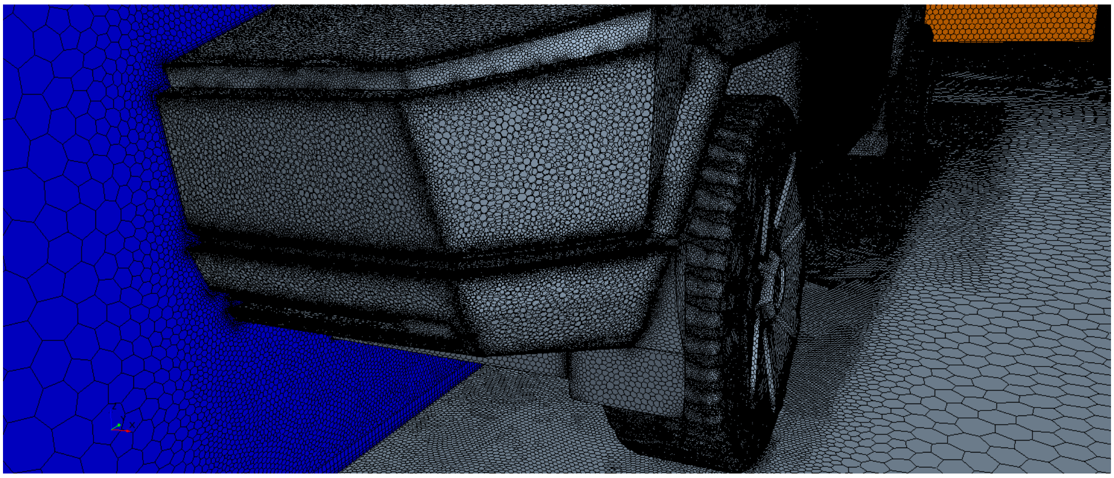

Figure 6.5: Meshed geometry on STAR CCM+ with add-on details installed

6.3 Processing

Physics setup

Our next step was to setup physics of our problem, starting with indication of external aerodynamics parameters of our car and setting models:

- Three dimensional
- Steady
- Gas
- Segregated flow
- Constant density
- Turbulent
- K-epsilon
- Cell quality remediation

Following this, we had set up:

1) Properties of air:

- Density: 1.225 Kg/m3
- Dynamic viscosity: 1.79E-5 Pa-s

2) Flow initial conditions:

- Velocity: [0.0; 20.0; 0.0] m/s

3) Boundary conditions for each surface:

- Inlet velocity for wind tunnel: 38.89 m/s
- Outlet pressure for wind tunnel: 0 Pa
- Front Floor of wind tunnel: slip condition
- Rear Floor of wind tunnel: no slip condition

- Half plane type of wind tunnel: symmetry
- Top floor of wind tunnel: slip condition
- Side plane of wind tunnel: slip condition
- All other boundaries: no slip wall

Then we had initialized a solution 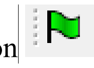.

Reports setup

First report to set up was a frontal area report and we executed it by selecting all faces of our vehicle and direction of calculation (direction of flow).

Secondly, we had set up and generated reports for drag and lift force by adding all parts of our vehicle and specifying normalization values.

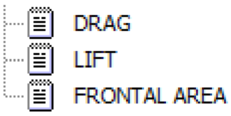

Finally, we had run the simulation .

6.4 Post-processing

After running out our simulation we can evaluate the solution through an opened monitors. One of this monitor is the residuls plot. This simulation also had run for 700 iterations. Residuals are tending down, as the solution is converging, nearly close to 0.001 which is acceptable for industrial cases.

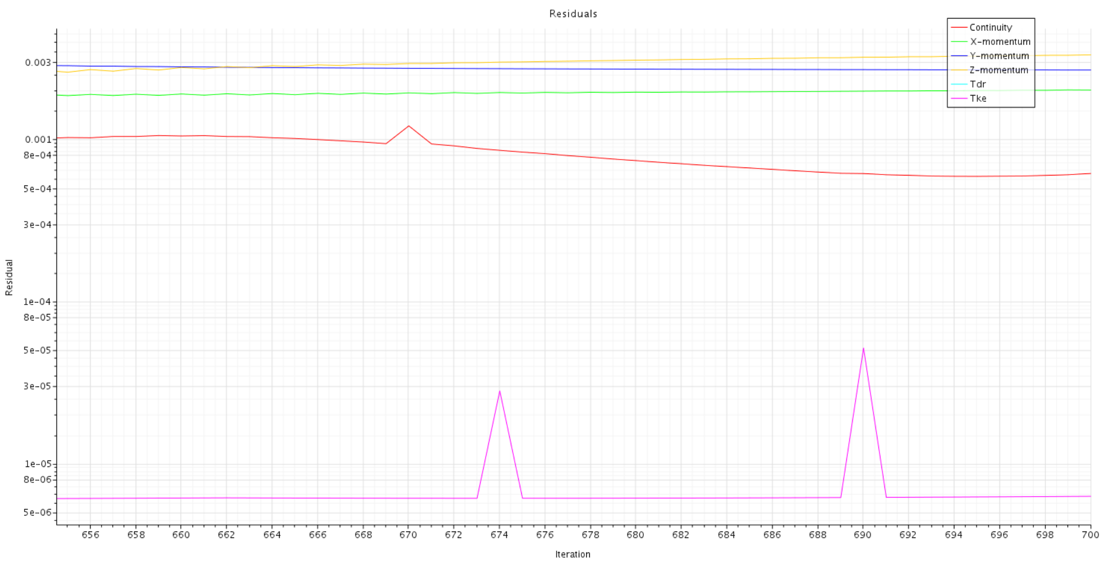

Figure 6.6: Residuals convergence plot of final steps on STAR CCM+ with add-on details installed

Drag coefficient value convergence is also important and consequently we can identify their convergence to a specific value after some steps in drag coefficient monitor:

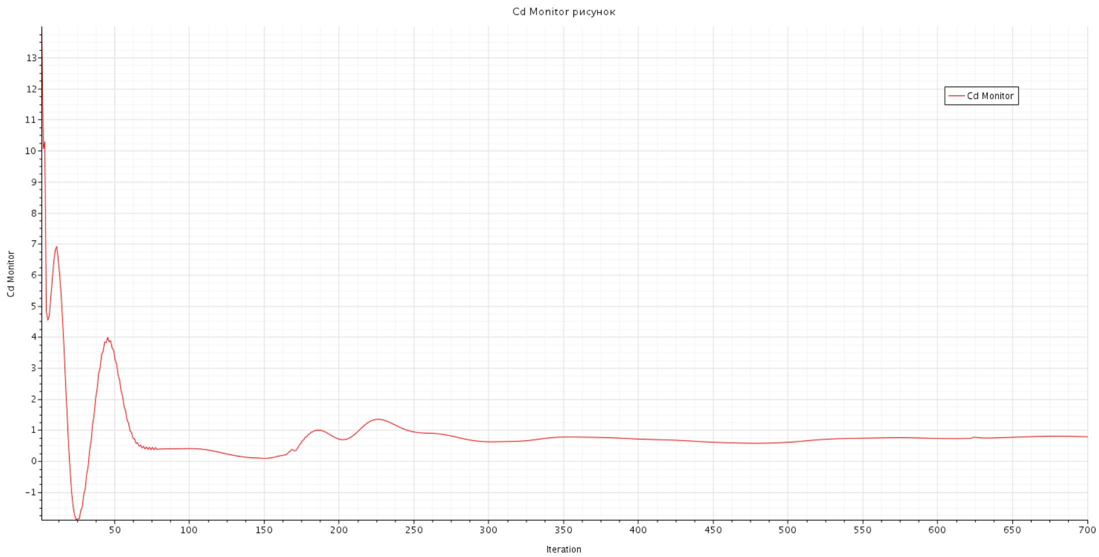

Figure 6.7: Drag coefficient convergence plot on STAR CCM+ with add-on details installed

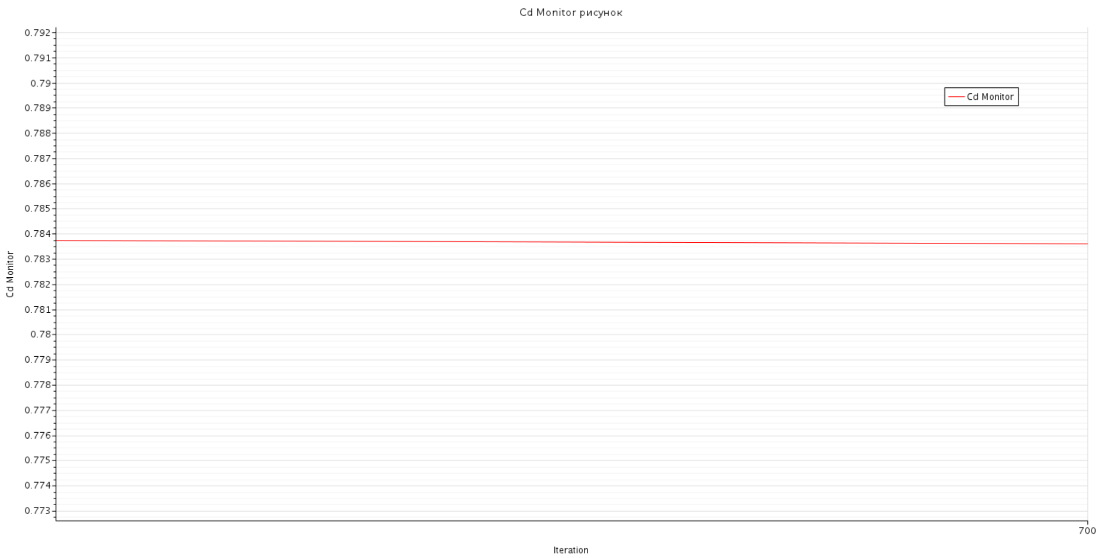

Figure 6.8: Drag coefficient plot converged value on STAR CCM+ with add-on details installed

In our case we had obtained the value of drag coefficient equal to **0.784**. In comparison to our baseline configuration drag coefficient value of **0.807**, we can recognize remarkable change in the value of drag coefficient, which is **0.023.**

Lift coefficient value convergence is also important and consequently we can identify their convergence to a specific value after some steps in lift coefficient monitor:

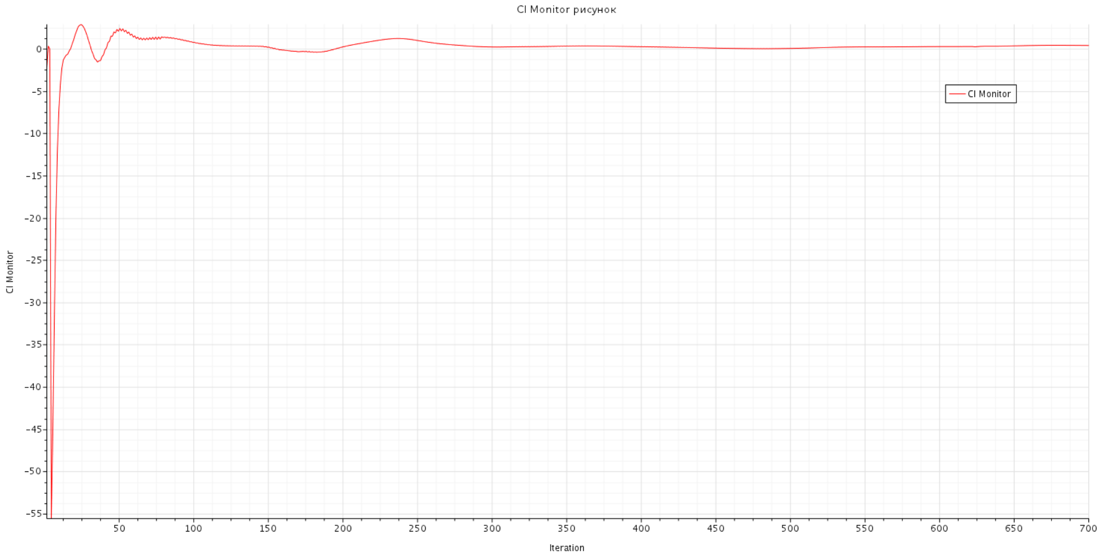

Figure 6.9: Lift coefficient convergence plot on STAR CCM+ with add-on details installed

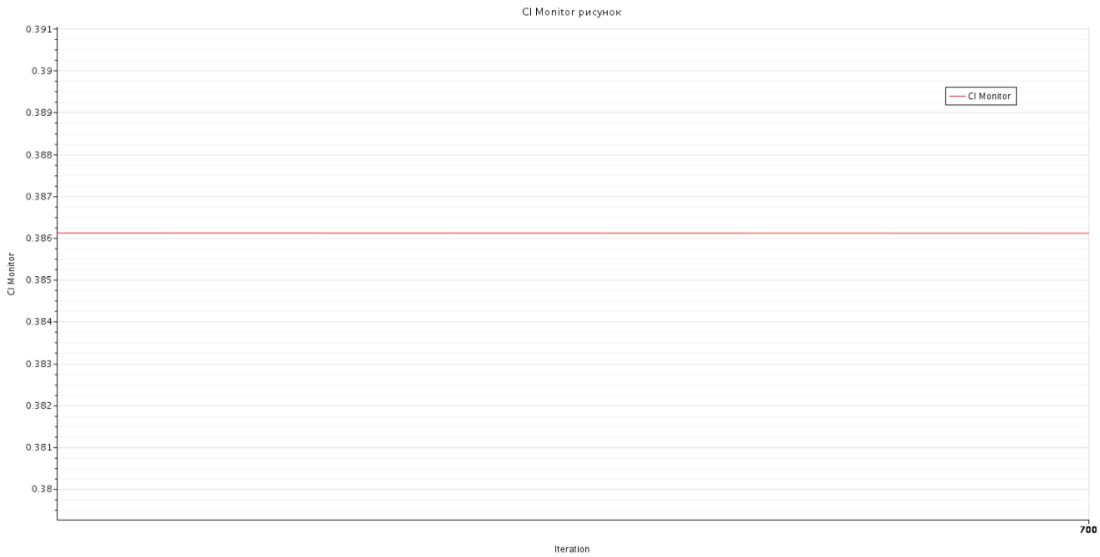

Figure 6.10: Lift coefficient plot converged value on STAR CCM+ with add-on details installed

In our case we had obtained the value of lift coefficient equal to **0.386**. In comparison to our baseline configuration lift coefficient value of **0.501**, we can recognize a big change in the value of the lift coefficient, which is **0.115.**

Air dam effect

To start investigating the effect of an air dam, we started with investigating the pressure coefficient and velocity magnitude representing scenes:

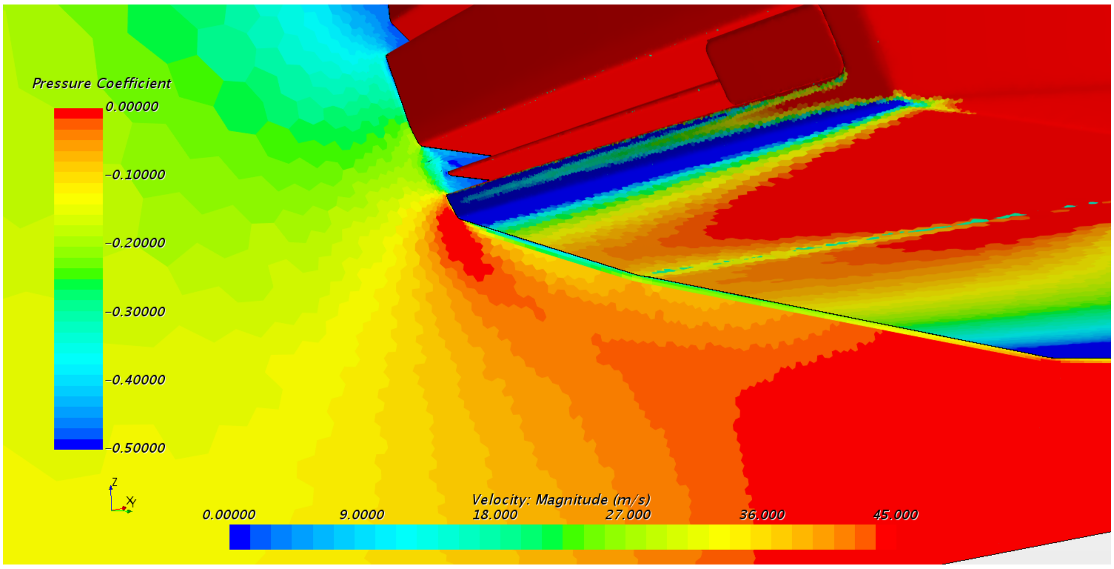

Figure 6.11: Vehicle front lower part pressure coefficient and velocity magnitude scene without air dam configuration.

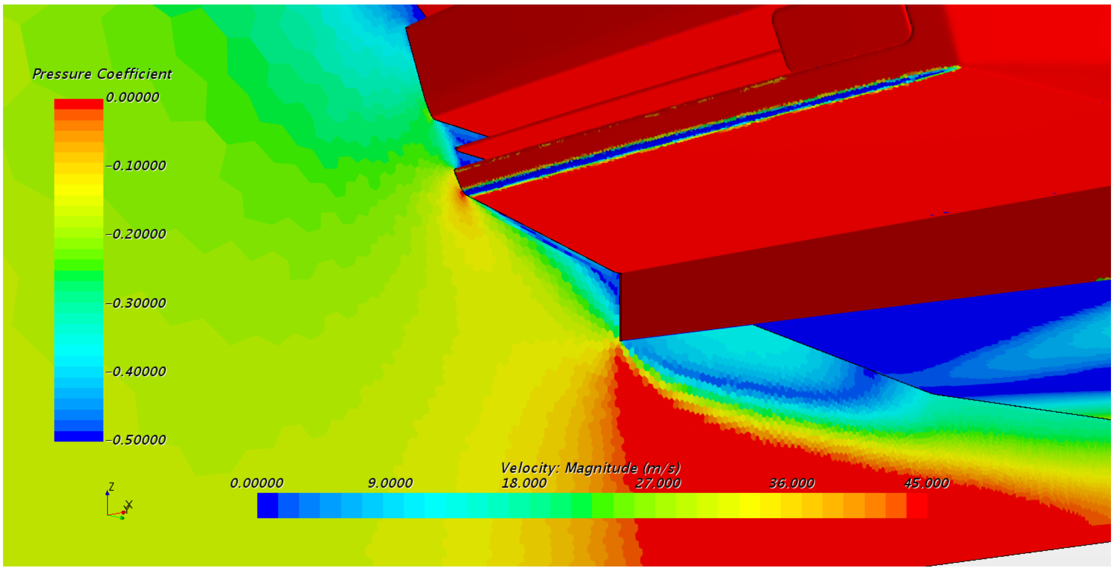

Figure 6.12: Vehicle front lower part pressure coefficient and velocity magnitude scene with air dam configuration.

If we start investigating the effect of an air dam, we can clearly see that the flow is redirected underneath the vehicle by looking on the velocity plane represented at the symmetry plane, which results on directing flows of air around the vehicle. By investigating this phenomenon, we can predict how efficiently it will work for lift decrease, by result increasing the grip of the tires.

In contrary, pressure coefficient scene represents a generation of high-pressure region near an air dam, which in opposite will cause a small resistance in the vehicle front lower part.

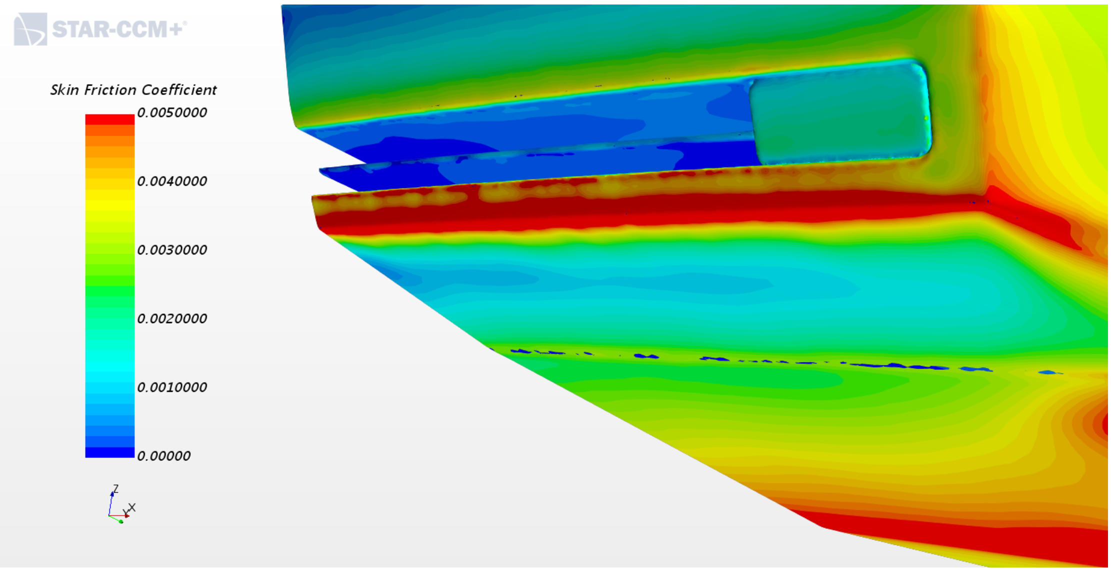

Figure 6.13: Vehicle front lower part skin friction coefficient scene without air dam configuration.

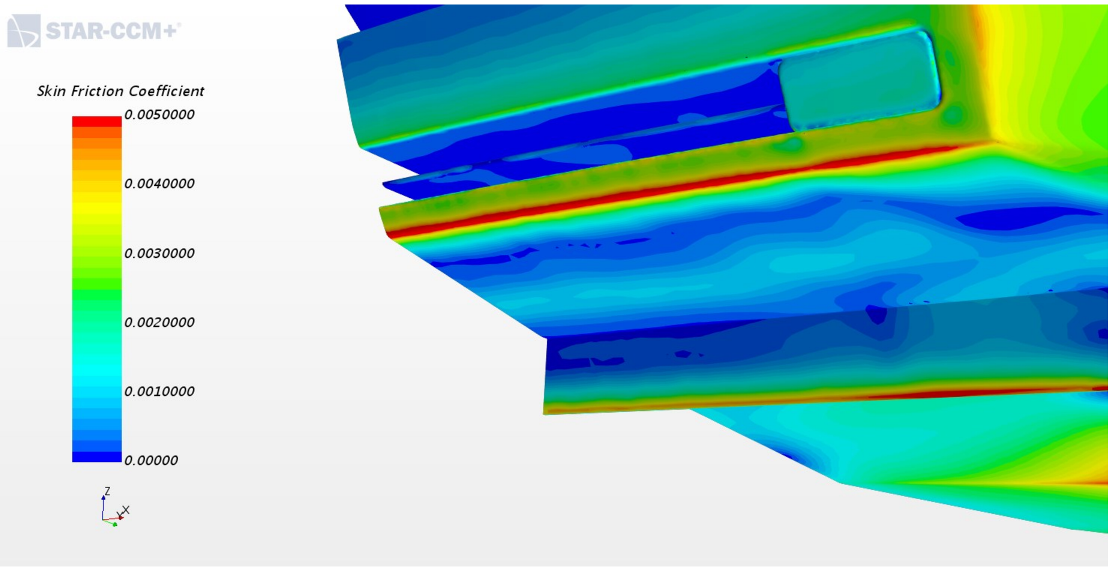

Figure 6.14: Vehicle front lower part skin friction coefficient scene with air dam configuration.

By comparing skin friction coefficient scenes of two configurations, we can recognize that high velocity flow in the vehicle front lower part is replaced by low velocity flow, obviously due to restricting air dam to the flow of an air before and after the installation location of a this detail.

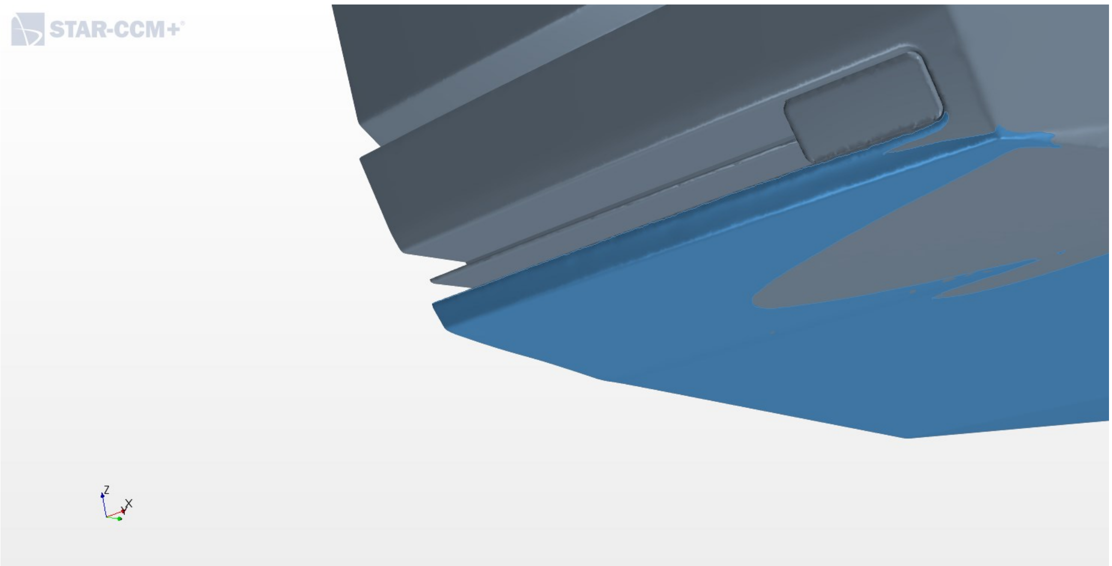

Figure 6.15: Vehicle front lower part total pressure coefficient scene without air dam configuration.

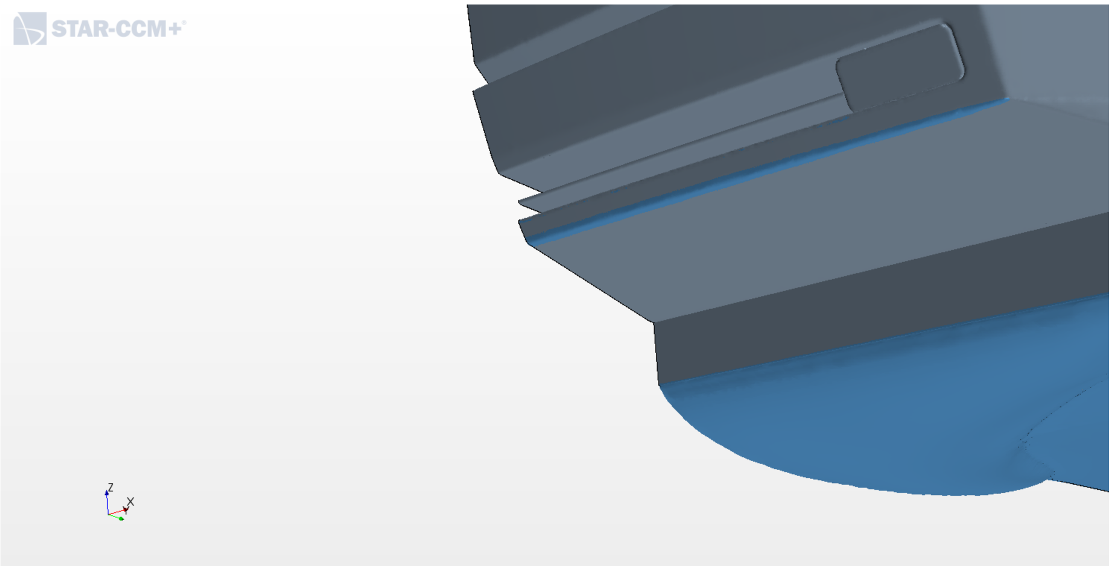

Figure 6.16: Vehicle front lower part total pressure coefficient scene with air dam configuration.

By looking into the two scenes above, which are representing total pressure coefficients with value of zero, we can easily recognize small reverse flow generation after an air dam installed position.

To conclude we can say that the air dam installed in the vehicle front lower part has contributed mainly on the reduction of lift coefficient of our car with a perturbed air flow under the vehicle, by having small effect on drag generation due to pressure generated on the surface of this detail.

Front wheel spats effect

Next, it arrived time to investigate an effect of a front wheel spats for a baseline and an improved configuration.

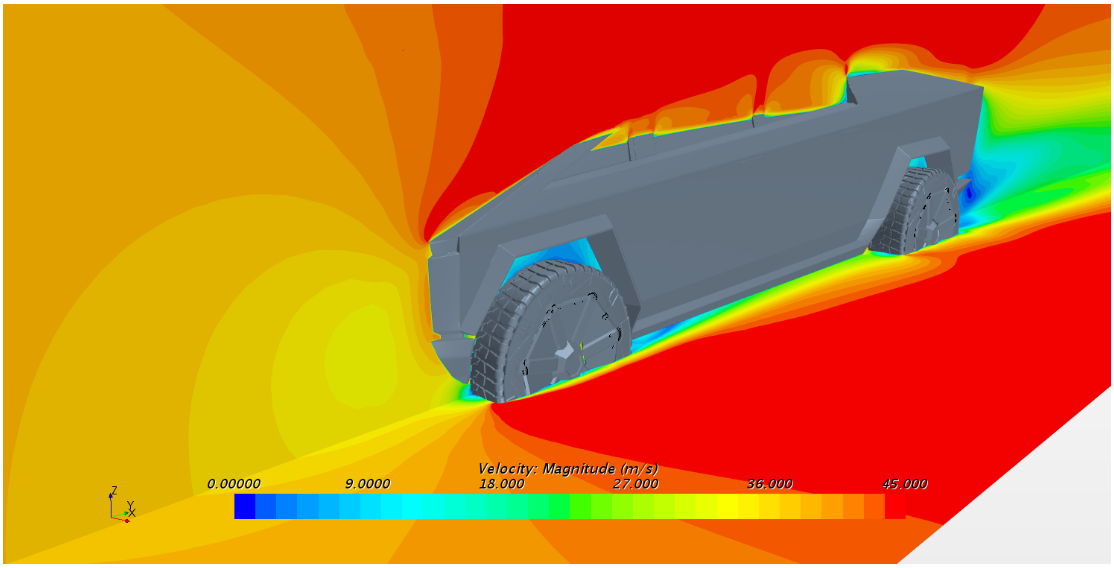

Figure 6.17: Vehicle front wheel area velocity magnitude scene without front wheel spats configuration.

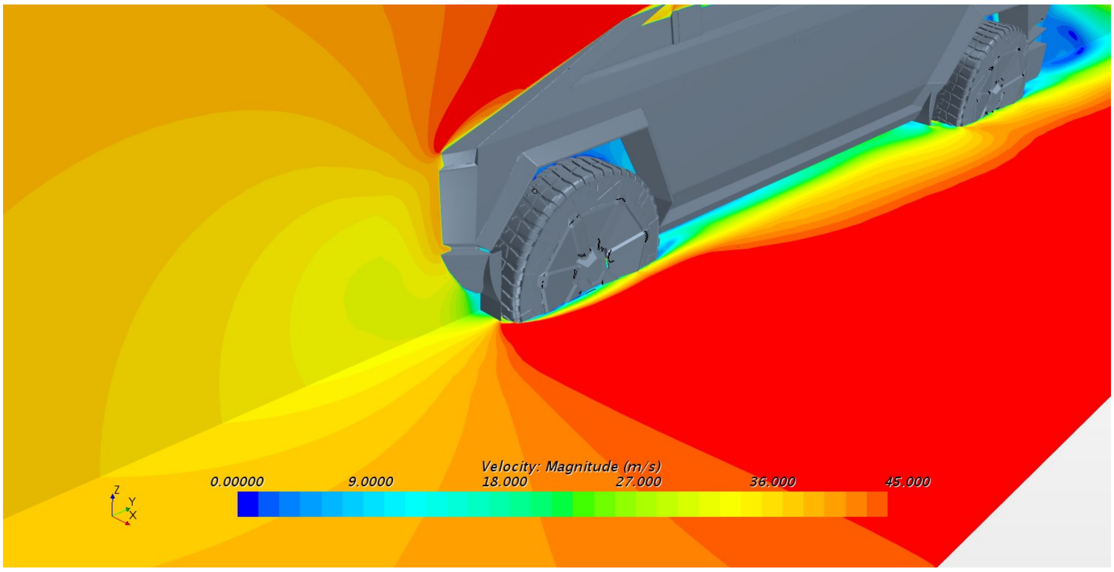

Figure 6.18: Vehicle front wheel area velocity magnitude scene with front wheel spats configuration.

From a baseline configuration we can see how high velocity flow impacts directly a front wheel and generating a remarkable wake region after the wheel underneath the vehicle. But in improved configuration we can recognize how air flow is interacting with the front wheel spats and this wake region is decreasing.

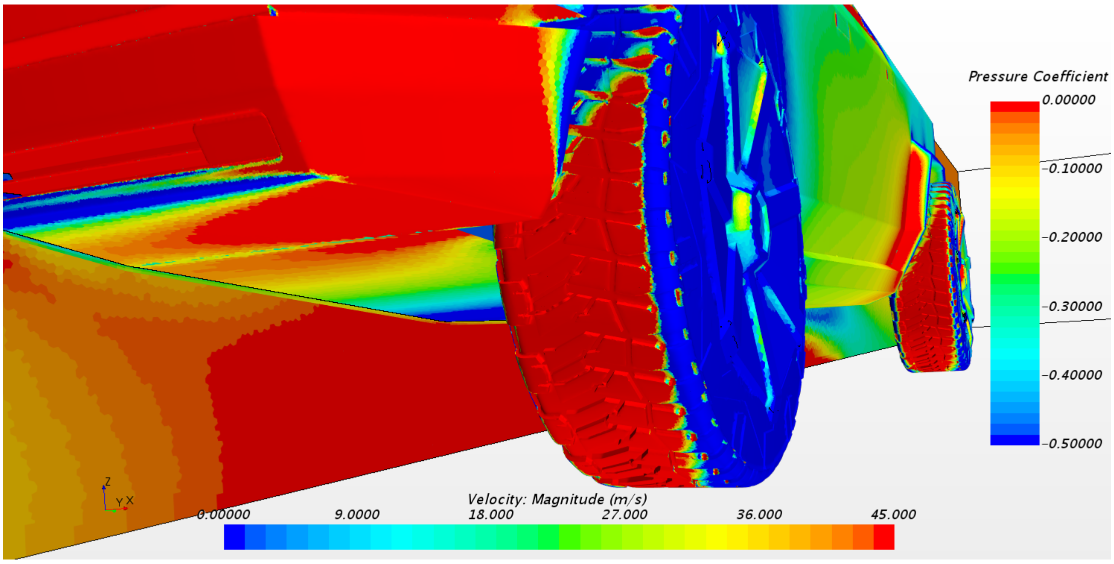

Figure 6.19: Vehicle front wheel area pressure coefficient scene without front wheel spats configuration.

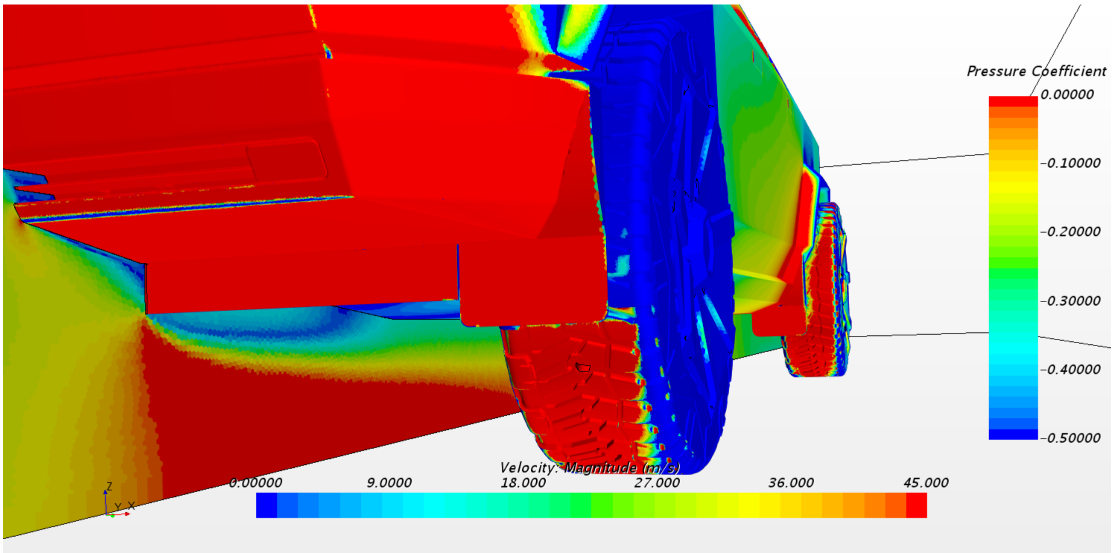

Figure 6.20: Vehicle front wheel area pressure coefficient scene with front wheel spats configuration.

By analysing front wheel spats effect on the pressure coefficient scene, we can see that the drag generation area due to surface pressure on a wheel is just transferred from the wheel on the baseline configuration, into the wheel spats in the improved version. And if investigate this scene further we can identify low pressure region increase in the improved configuration, since in this case air flow starts to accelerate farther from the wheels as represented in vehicle front wheel area velocity magnitude scene before.

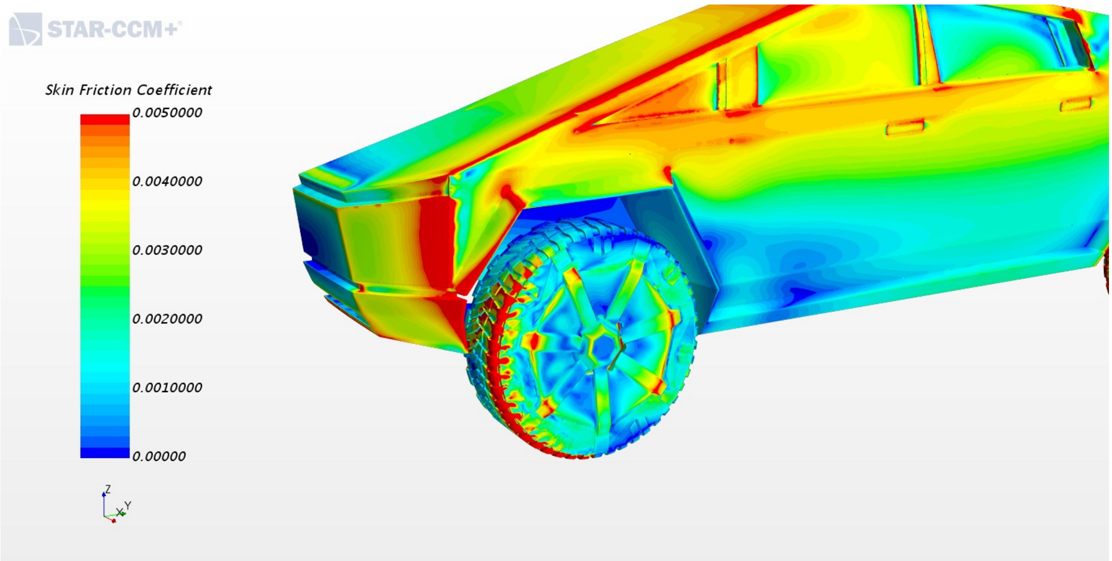

Figure 6.21: Vehicle front wheel area skin friction coefficient scene without front wheel spats configuration.

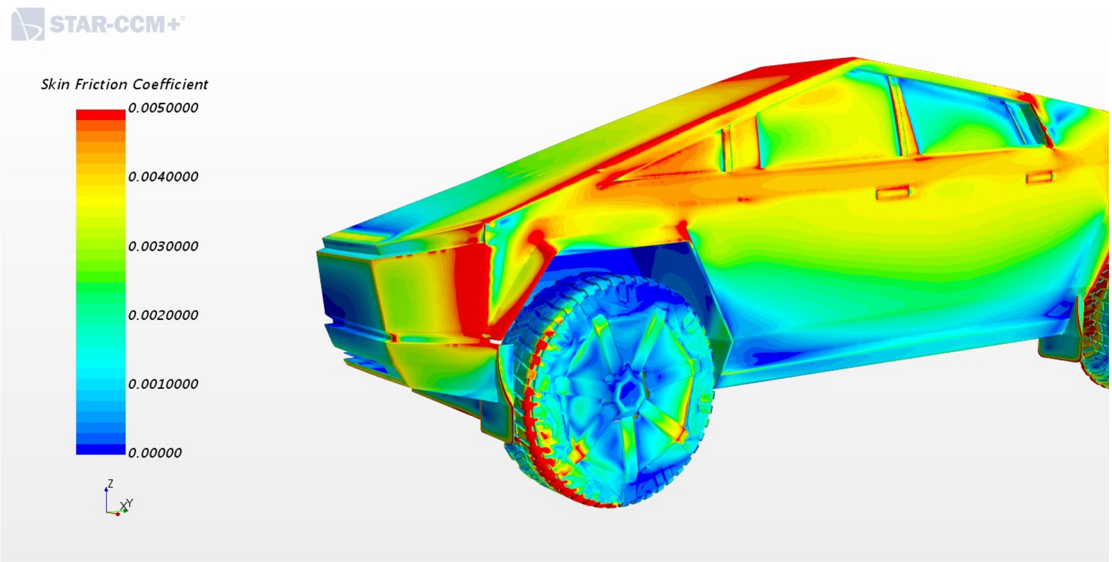

Figure 6.22: Vehicle front wheel area skin friction coefficient scene with front wheel spats configuration.

By analysing two above scenes, we can recognize the remarkable effect of a wheel spats, since in the baseline configuration the flow was less attached to the side of the vehicle. But in the improved configuration we can see more attachment of a flow to the side part of a vehicle. In addition to this we can identify the reduction of high velocity flow at the front part of a tire in the improved version.

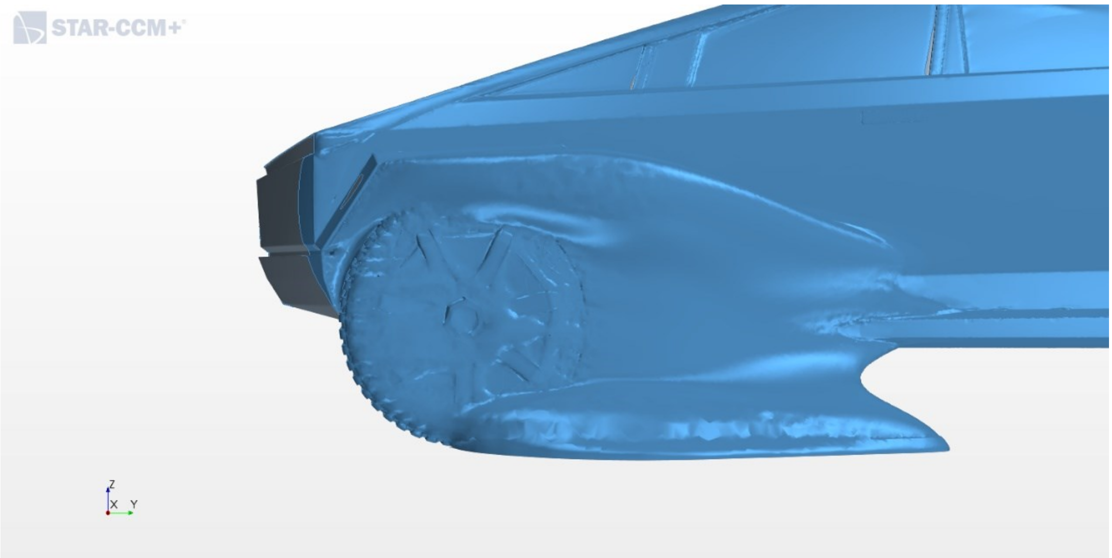

Figure 6.23: Vehicle front wheel area total pressure coefficient scene without front wheel spats configuration.

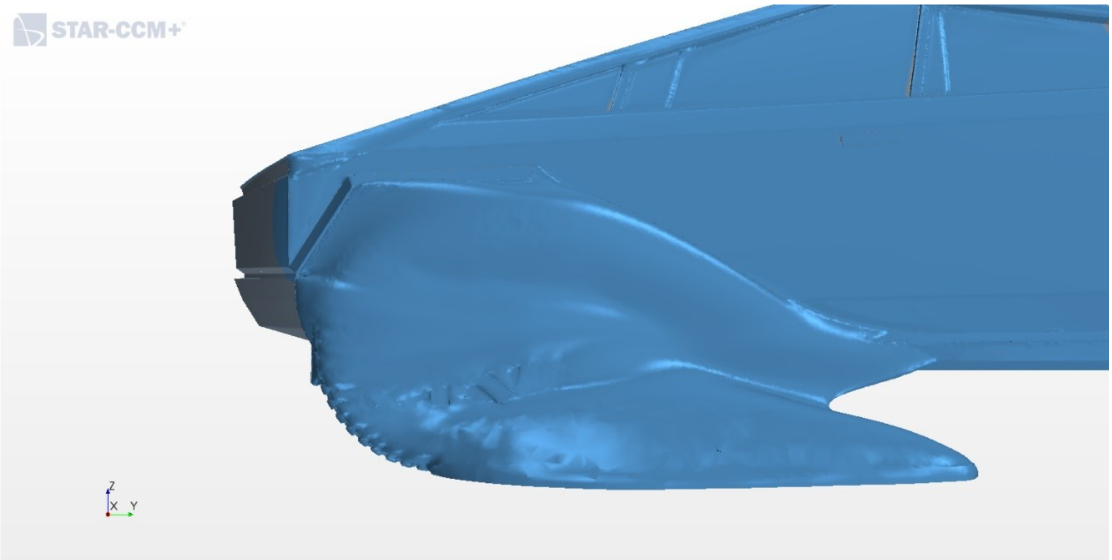

Figure 6.24: Vehicle front wheel area total pressure coefficient scene with front wheel spats configuration.

By describing further we can analyse total pressure coefficient scene. Here we can see a decrease of a wake region at the side part of the vehicle and it is obvious that this is due to the increase of an attached flow at that region. However, we can recognize an increase of wake region volume around a wheel, which is the result of an acceleration of a flow farther the wheel due to front wheel spats.

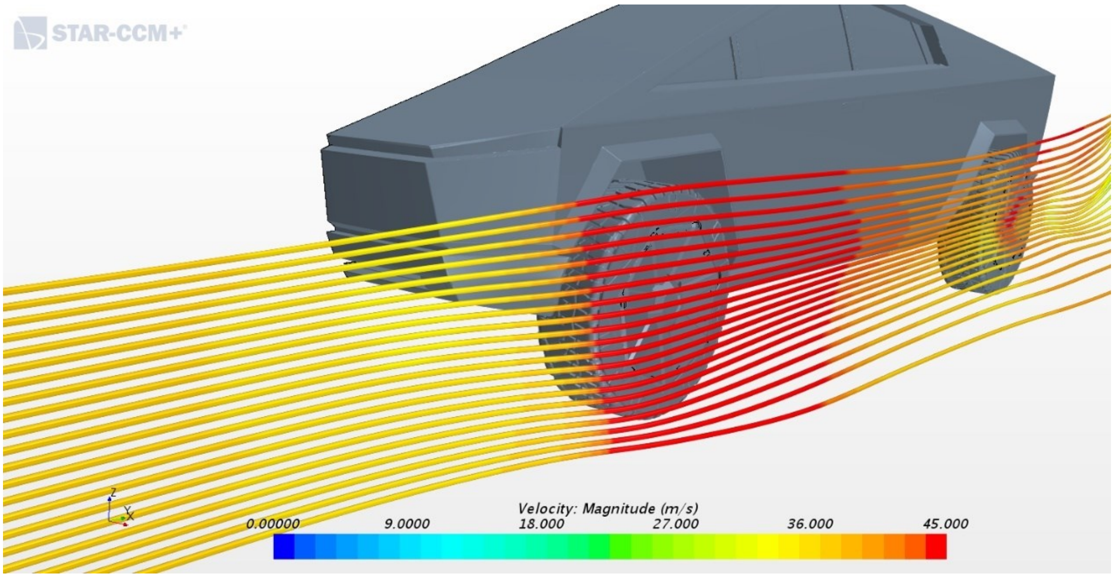

Figure 6.25: Vehicle front wheel area streamlines scene without front wheel spats configuration.

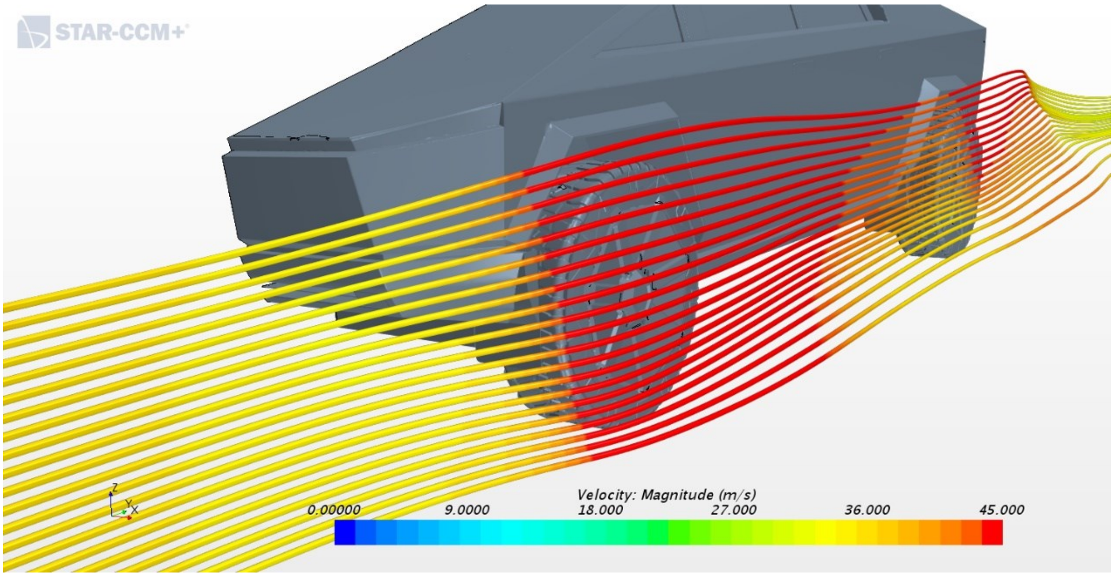

Figure 6.26: Vehicle front wheel area streamlines scene with front wheel spats configuration.

By analysing above two scenes, it is easy to see the better acceleration of a flow after the wheel region due to the effect of the front wheel spats in the improved version of our vehicle, meaning that the initial flow is less interrupted by the flow field near the wheel.

To conclude we can say that the front wheel spats have a positive impact on drag reduction and to improve stability of a vehicle by reducing air flow impact at the side part of a vehicle.

Rear wheel spats effect

Next, it arrived time to investigate an effect of a front wheel spats for a baseline and an improved configuration.

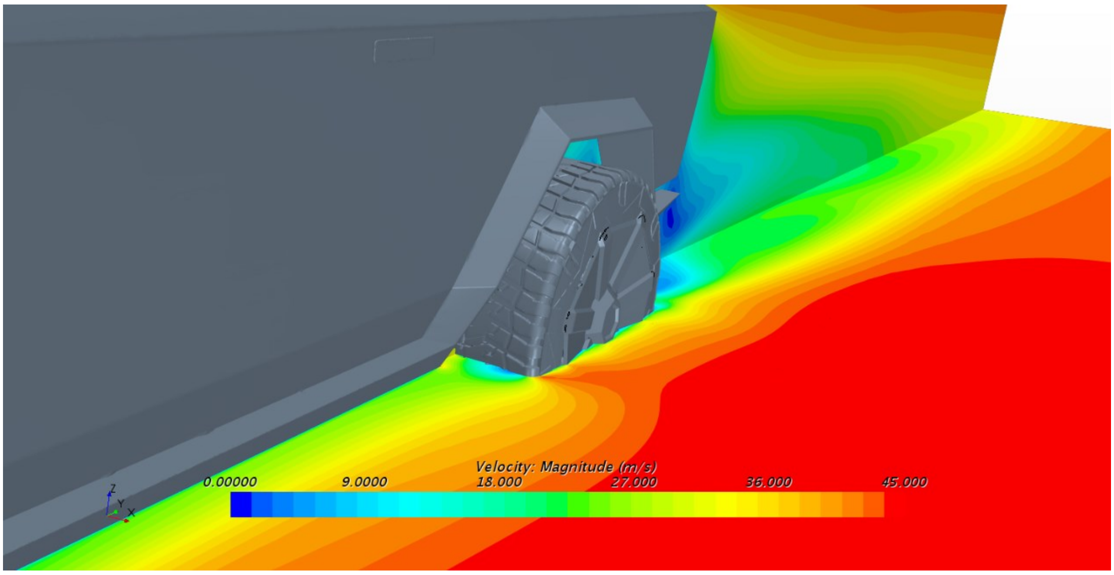

Figure 6.27: Vehicle rear wheel area velocity magnitude scene without rear wheel spats configuration.

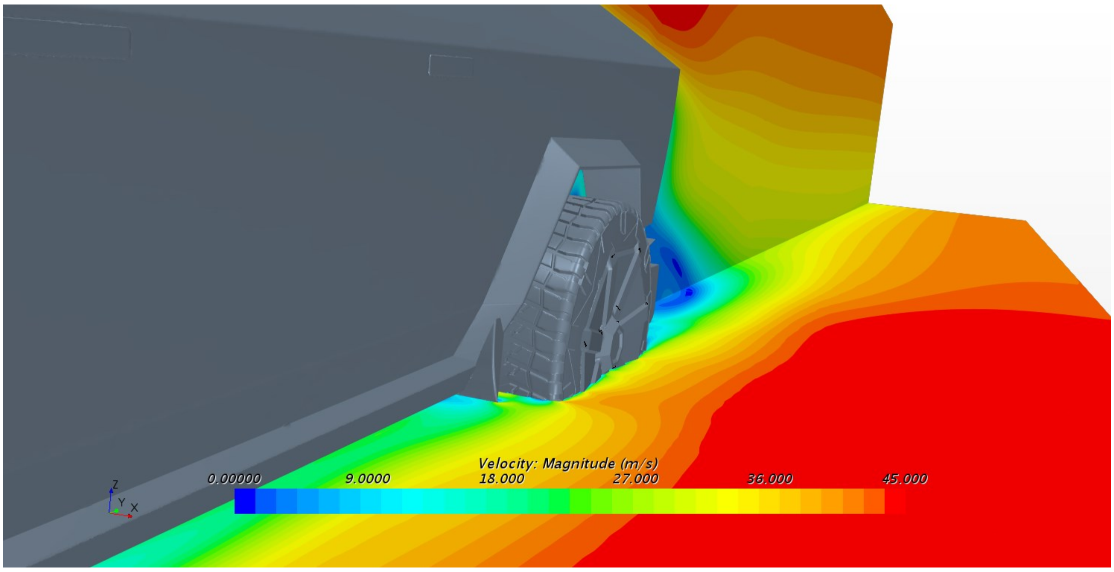

Figure 6.28: Vehicle rear wheel area velocity magnitude scene with rear wheel spats configuration.

Looking to a baseline configuration we can see how flow impacts directly a rear wheel and generating a remarkable wake region just after the wheel underneath the vehicle. But in improved configuration we can recognize how air flow is interacting with the rear wheel spats and this wake region is decreasing just after the wheel back. In addition to this, we can see flow acceleration area moved farther a wheel region in the improved configuration due to the presence of a rear wheel spats.

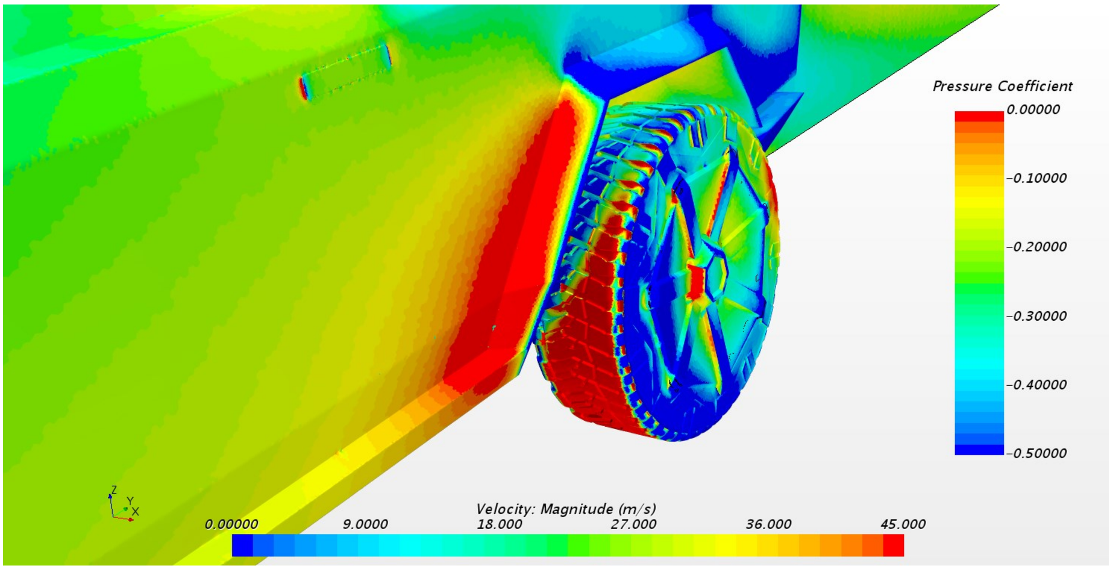

Figure 6.29: Vehicle rear wheel area pressure coefficient scene without rear wheel spats configuration.

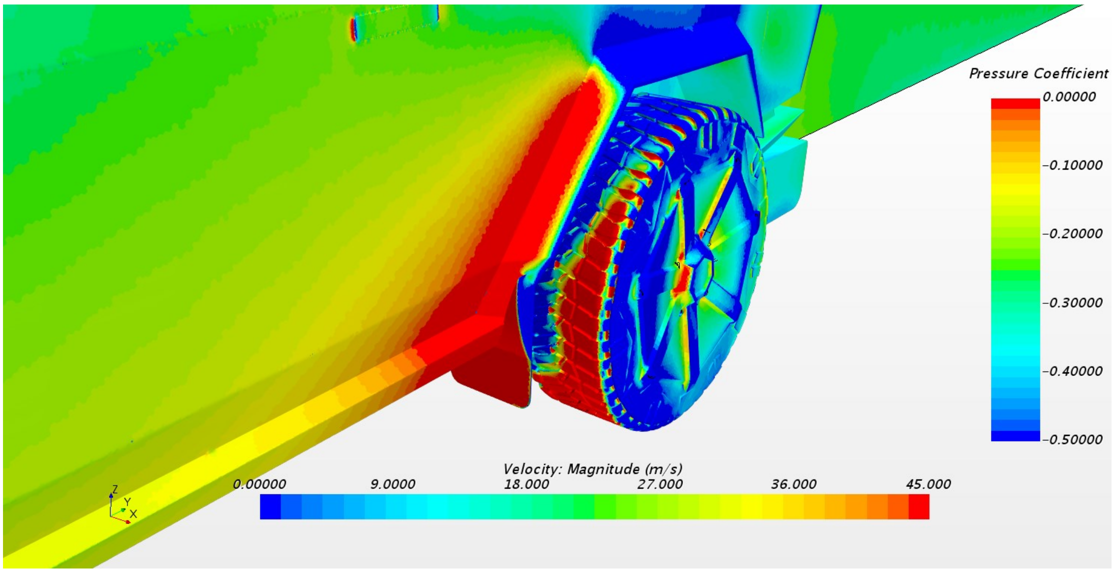

Figure 6.30: Vehicle rear wheel area pressure coefficient scene with rear wheel spats configuration.

By analysing a rear wheel spats effect on the pressure coefficient scene, we can see that the drag generation area due to surface pressure on a wheel is just transferred from the wheel on the baseline configuration, into the wheel spats in the improved version. And if investigate this scene further we can identify low pressure region increase in the improved configuration, since in this case air flow starts to accelerate farther from the wheels as represented in vehicle rear wheel area velocity magnitude scene before.

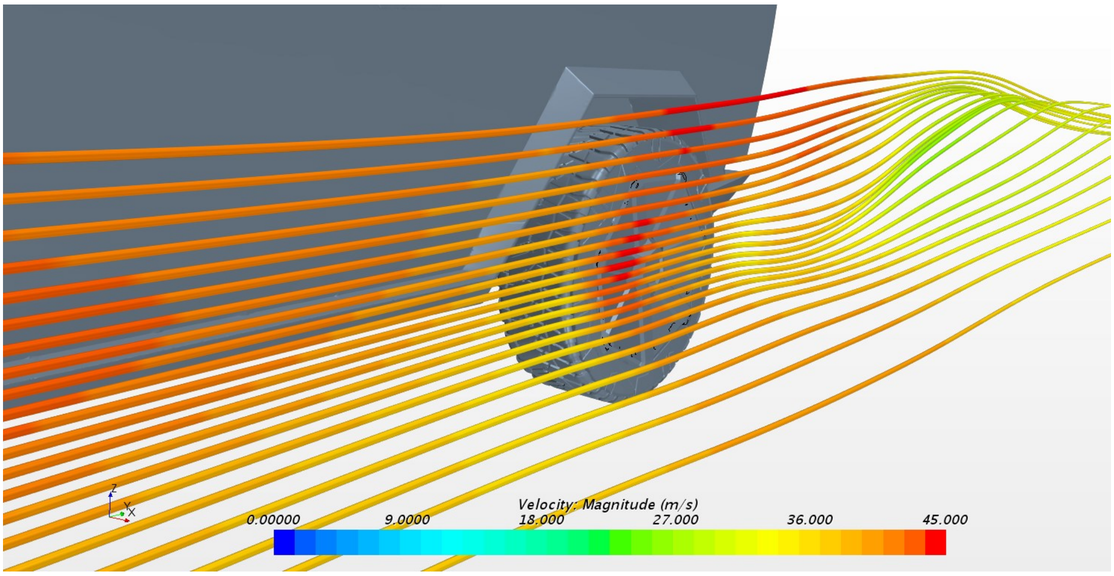

Figure 6.31: Vehicle rear wheel area streamlines scene without rear wheel spats configuration.

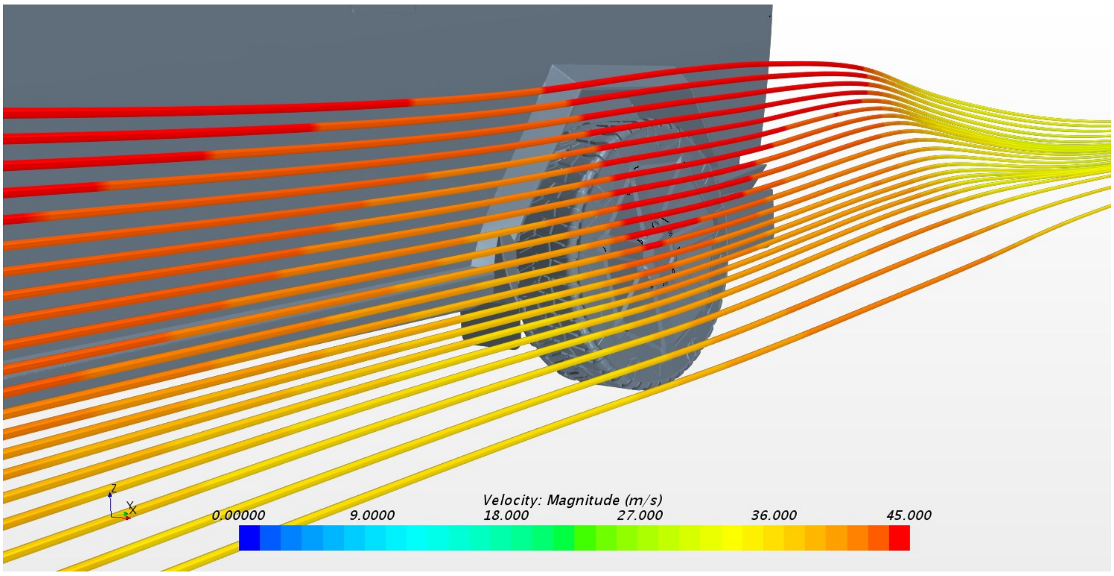

Figure 6.32: Vehicle rear wheel area streamlines scene with rear wheel spats configuration.

By analysing above two scenes, it is easy to see the better acceleration of a flow after the wheel region due to the effect of the rear wheel spats in the improved version of our vehicle, meaning that the initial flow is less interrupted by the flow field near the rear wheel.

To conclude we can say that the rear wheel spats have a positive impact on drag reduction and to improve stability of a vehicle by reducing air flow impact in the rear wheel area and at the side part of a vehicle.

Diffuser effect

Lastly, it arrived time to investigate an effect of a rear diffuser for a baseline and an improved configuration.

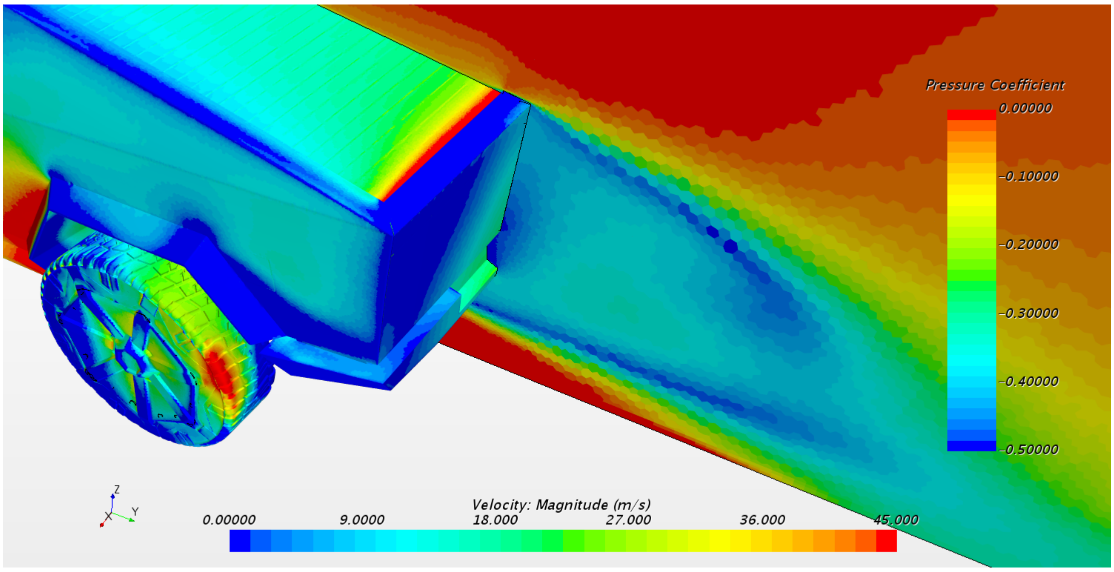

Figure 6.33: Vehicle rear part pressure coefficient and velocity magnitude scene without rear diffuser configuration.

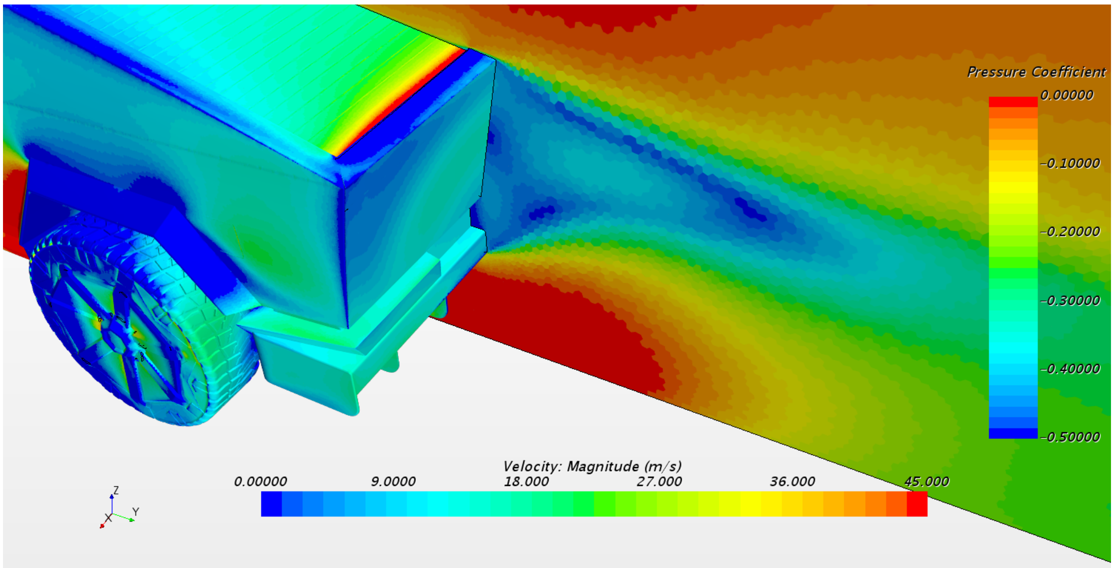

Figure 6.34: Vehicle rear part pressure coefficient and velocity magnitude scene with rear diffuser configuration.

By looking to above scenes we can recognize a remarkable effect of rear diffuser. If we start with velocity magnitude plane description located at the symmetry plane, we can see that low velocity region has reduced its effect at the centerline position of our vehicle mainly due to an accelerated flow caused by a diffuser and for some amount due to front air dam. Turning into the pressure coefficient description, we can see that low pressure area at the back region "pulling" our vehicle backward, has reduced its effect.

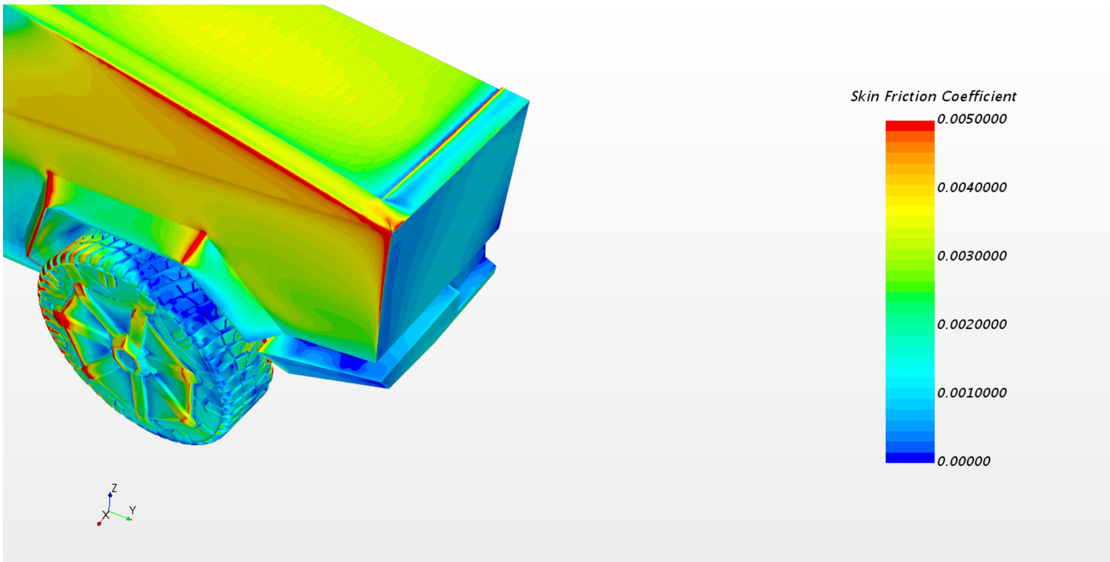

Figure 6.35: Vehicle rear part skin friction coefficient scene without rear diffuser configuration.

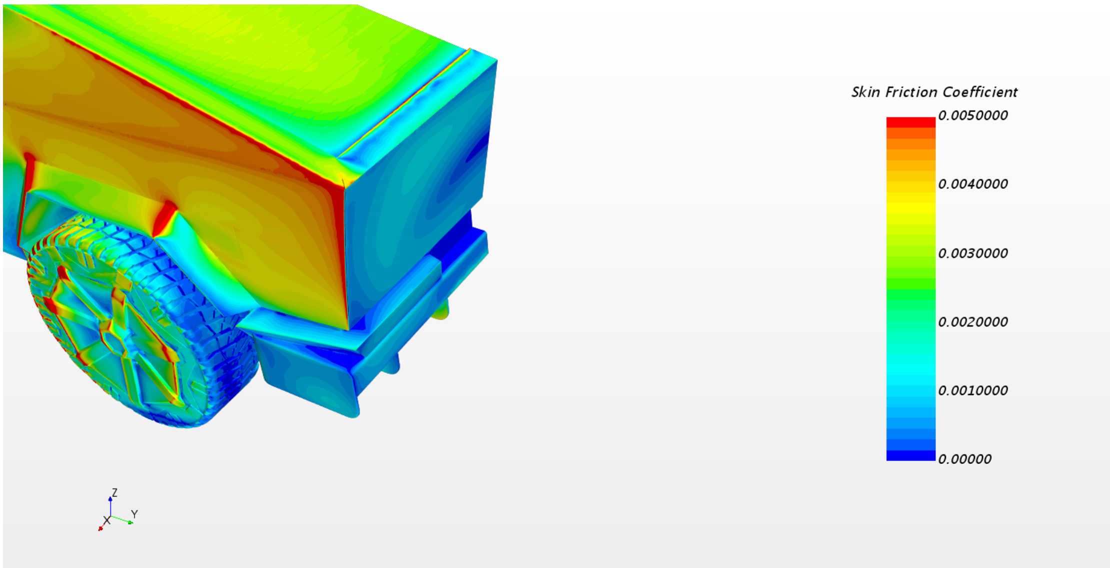

Figure 6.36: Vehicle rear part skin friction coefficient scene with rear diffuser configuration.

By looking at above scenes we can recognize the change in the skin friction coefficient distribution at the back of our vehicle mainly due to a rear diffuser installation. But due to sharp rear right-end, there is not a change in the position of a separation line.

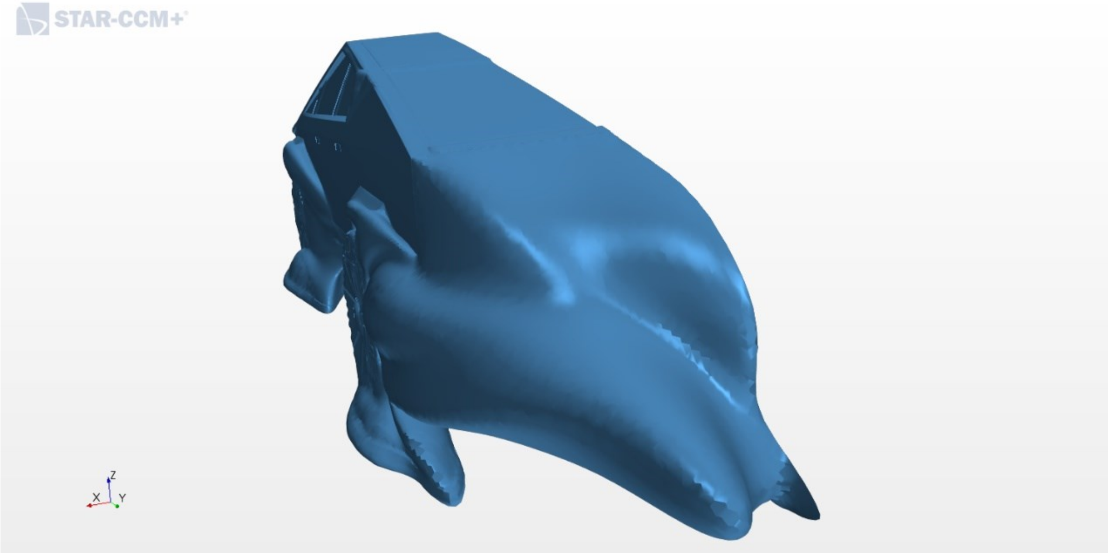

Figure 6.37: Vehicle rear part total pressure coefficient scene without rear diffuser configuration.

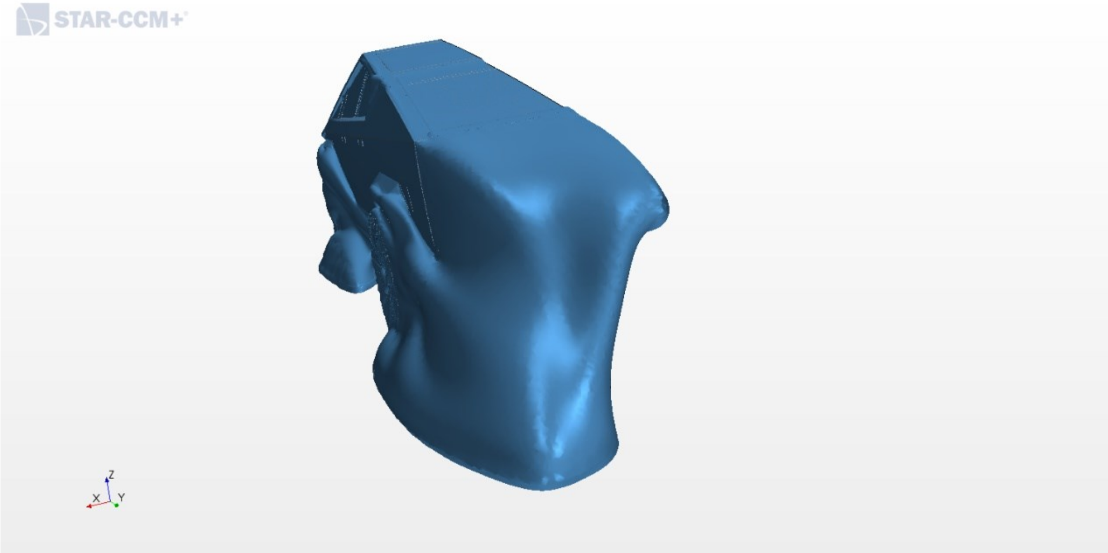

Figure 6.38: Vehicle rear part total pressure coefficient scene with rear diffuser configuration.

By investigating a total pressure coefficient scene, we can see a reduction in the length and also in the volume of a wake region at the back of a car. This improvement caused mainly due to a rear diffuser has a positive effect in the drag coefficient reduction.

Chapter 7

Conclusion

Our goal to analyze the outstanding maverick design of our vehicle of interest had achieved by prevailing very interesting results. Since we recognized the very good behavior of some regions, like the roof area with low air flow detachment despite its unusual design. Additionally, the sloped shape of a windscreen resulted in attached air flow on the surface, and the long trunk cover serves as pressure recovery for a Cybertruck.

In addition to this, an improvement of an aerodynamic performance of our vehicle by reducing drag and lift coefficient to promote effective usage of an energy is also achieved resulting in the decrease in drag coefficient for a value of **0.023** and in the decrease in lift coefficient for a value of **0.115.** This improvement in aerodynamic coefficients will obviously result in the higher range traveled by a vehicle on the single battery charge, also in the higher stability at highway speeds.

Bibliography

[1] "Legendary quotes from "Il Commendatore" Enzo Ferrari. p. 1," [Ferrari F1 Forums] 2023. http://www.thescuderia.net/forums/showthread.php/31826-Legendary-quotes-from-quot-Il-Commendatore-quot-Enzo-Ferrari.

[2] S. d'Ambrosio, "Engine-vehicle matching," *Combustion Engines and their Application to Vehicle Lecture notes,* p. 34, [Politecnico di Torino] 2019/2020.

[3] "2023 FORD F-150 LIGHTNING. p. 1," [Ford Motor Company] 2023. https://www.ford.com/trucks/f150/f150-lightning/?intcmp=f150brand-cta-reveal-f-150-lightning.

[4] "Cybertruck. p. 2," [Tesla] 2023. https://www.tesla.com/cybertruck.

[5] "What is Drag? p. 1," [Glenn Research Center. NASA] 2022. https://www1.grc.nasa.gov/beginners-guide-to-aeronautics/what-is-drag/#lift.

[6] "What is Lift? p. 1," [Glenn Research Center. NASA] 2022. https://www1.grc.nasa.gov/beginners-guide-to-aeronautics/what-is-lift/.

[7] "Aerodynamics of bluff bodies. p. 1," [Embry-Riddle Aeronautical University] 2023. https://eaglepubs.erau.edu/introductiontoaerospaceflightvehicles/chapter/bluff-body-flows/.

[8] "Drag of a Sphere. p. 1," [Glenn Research Center. NASA] 2022. https://www1.grc.nasa.gov/beginners-guide-to-aeronautics/drag-of-a-sphere/.

[9] "Equations of Compressible and Incompressible Flow in Fluid Dynamics. p. 1," [Cadence Design Systems, Inc.] 2023. https://resources.system-analysis.cadence.com/blog/msa2022-equations-of-compressible-and-incompressible-flow-in-fluid-dynamics.

[10] J. Anderson, Fundamentals of Aerodynamics. p. 129, 6th Ed., McGraw–Hill,, 2017.

[11] "Conservation of mass: Continuity equation. p. 1," [Embry-Riddle Aeronautical University] 2023. https://eaglepubs.erau.edu/introductiontoaerospaceflightvehicles/chapter/conservation-of-mass-continuity-equation/.

[12] "Conservation of momentum: Momentum equation. p. 1," [Embry-Riddle Aeronautical University] 2023. https://eaglepubs.erau.edu/introductiontoaerospaceflightvehicles/chapter/conservation-of-momentum-momentum-equation/.

[13] "Conservation of energy: Energy equation & Bernoulli's equation. p. 1," [Embry-Riddle Aeronautical University] 2023. https://eaglepubs.erau.edu/introductiontoaerospaceflightvehicles/chapter/conservation-of-energy-energy-equation-bernoullis-equation/.

[14] "How Does Aerodynamics Affect Fuel Economy? p. 1," [Haynes] 2023. https://haynes.com/en-us/tips-tutorials/aerodynamics-and-how-they-affect-fuel-economy.

[15] N. Amati, A. Tonoli, L. Castellazzi and S. Ruzimov, "Design of Electromechanical Height Adjustable Suspension. p. 2," *Journal of Automobile Engineering,* 2017.

[16] "The Effect of Aerodynamic Drag on Fuel Economy. p. 1," [Auto Research Center] 2023. http://www.arcindy.com/effect-of-aerodynamic-drag-on-fuel-economy.html#:~:text=Aerodynamic%20drag%20is%20proportional%20to,fuel%20used%20to%20overcome%20drag.

[17] "Aerodynamic drag. p. 1," 2023. https://physics.info/drag/.

[18] Laura Lorefice Maria, "Application. p. 3," *Aerodynamics Lecture Notes.,* [FCA] 2019/2020.

[19] S. Haggag and A. Mansouri, "Aerodynamic Forces Impact on Vehicle Braking Longitudinal Dynamics with a Sliding Mode Controller. p. 9," in *SAE Technical Paper*, 2016.

[20] "Bugatti Veyron Technology. p. 1," [BUGATTI AUTOMOBILES S.A.S.] 2023. https://www.bugatti.com/models/veyron-models/technology/.

[21] J. Keogh, T. Barber, S. Diasinos and G. Doig, "Techniques for Aerodynamic Analysis of Cornering Vehicles. p. 2," *SAE Technical Paper,* 2015.

[22] L. L. Maria, "Application p. 7," *Aerodynamics Lecture Notes,* [FCA] 2019/2020.

[23] B. George, Jairesh J. V., Chithraiselvan G. and Gokul Nath S., "Determination of Critical Downforce Coefficient of a Vehicle for Optimum Aerodynamic Performance," *International Research Journal of Engineering and Technology (IRJET),* pp. 323-325, 2018.

[24] A. Brandt, B. Jacobson and S. Sebben, "High speed driving stability of road vehicles under crosswinds: an aerodynamic and vehicle dynamic parametric sensitivity analysis. p. 2337,2339," 2021. https://www.researchgate.net/publication/352129364_High_speed_driving_stability_of_road_vehicles_under_crosswinds_an_aerodynamic_and_vehicle_dynamic_parametric_sensitivity_analysis.

[25] L. Cattafesta, C. J. Bahr and J. Mathew, "Fundamentals of Wind-Tunnel Design. p. 1," 2010. https://www.researchgate.net/publication/230271809_Fundamentals_of_Wind-Tunnel_Design.

[26] G. Le Good, C. Johnson, B. Clough and R. Lewis, "The Aesthetics of Low Drag Vehicles. p. 2641," 2016. https://www.researchgate.net/publication/301197328_The_aesthetics_of_Low_Drag_vehicles.

[27] A. Ferraris, A. G. Airale, D. Berti Polato, A. Messana, S. Xu, P. Massai and M. Carello, "City Car Drag Reduction by Means of Shape Optimization and Add-On Devices. p. 3," 2019. https://iris.polito.it/retrieve/handle/11583/2816932/353444/CITY%20CAR%20DRAG%20REDUCTION%20_IRIS.pdf.

[28] AMWEL Enterprises, "A Brief History of CFD. p. 1," 2008. http://www.amwel.com/history.html.

[29] Spatial Team, "13 Key Applications of CFD Simulation and Modeling. p. 1," 2019. https://blog.spatial.com/cfd-modeling-applications.

[30] Spatial Team, "3 Core Components of CFD Analysis. p. 1," 2020. https://blog.spatial.com/cfd-analysis.

[31] "Navier-Stokes Equations. p. 1," [Glenn Research Center. NASA] 2021. https://www.grc.nasa.gov/www/k-12/airplane/nseqs.html.

[32] "CFD Simulation - What Is Computational Fluid Dynamics? p. 1," [Aerotak ApS] 2020. https://www.aerotak.dk/en/cfd.

[33] Nicola, "Tesla Cybertruck. p. 1," 2020. https://grabcad.com/library/tesla-cybertruck-18.

[34] Giuseppe Scantamburlo, "Applications," *Aerodynamics Lecture Notes,* pp. 30,31,42, [FCA] 2019/2020.